The Mechanics of Fibrin Networks and Their Alterations by Platelets

The Mechanics of Fibrin Networks and their Alterations by Platelets

A dissertation presented

by

Louise Marie Jawerth

to

The Department of Physics

in partial fulfillment of the requirements
for the degree of
Doctor of Philosophy
in the subject of
Physics

Harvard University
Cambridge, Massachusetts

April 2013

Dissertation Advisor: David A. Weitz Louise Marie Jawerth

The Mechanics of Fibrin Networks and their Alterations by Platelets

Abstract

Fibrin is a biopolymer that assembles into a network during blood coagulation to become the structural scaffold of a blood clot. The precise mechanics of this network are crucial for a blood clot to properly stem the flow of blood at the site of vascular injury while still remaining pliable enough to avoid dislocation. A hallmark of fibrin's mechanical response is strain-stiffening: at small strains, its response is low and linear; while at high strains, its stiffness increases non-linearly with increasing strain. The physical origins of strain-stiffening have been studied for other biopolymer systems but have remained elusive for biopolymer networks composed of stiff filaments, such as fibrin. To understand the origins of this intriguing behavior, we directly observe and quantify the motion of all of the fibers in the fibrin networks as they undergo shear in 3D using confocal microscopy. We show that the strain-stiffening response of a clot is a result of the full network deformation rather than an intrinsic strain-stiffening response of the individual fibers. We observe a distinct transition from a linear, low-strain regime, where all fibers avoid any internal stretching, to a non-linear, high-strain regime, where an increasing number of fibers become stretched. This transition is characterized by a high degree of non-affine motion. Moreover, we are able to precisely calculate the non-linear stress-strain response of the network by using the strains on each fiber measured directly with confocal microscopy and by assuming the fibers behave like linearly elastic beams. This result confirms that it is the network deformation that causes the strain-stiffening behavior of fibrin clots.

These data are consistent with predictions for low-connectivity networks with soft, bending, or floppy modes. Moreover, we show that the addition of small contractile cells, platelets, increases the low-strain stiffness of the network while the high-strain stiffness is independent of the presence of the platelets; this is also consistent with expectations for small contractile elements in a network with low connectivity. Our results elucidate the origins of strain-stiffening in fibrin networks as well as the mechanism underlying platelet-induced clot stiffening.

Contents

List of Figures

Acknowledgments

One of the nice things about grad school is that the work that consumes most of your time is immensely fun: Namely, doing experiments and figuring things out. However, I did not do these things in a vacuum and the work would not have been so fun or successful without being surrounded by so many truly awesome people. I have been around as the bio-part of the Weitz lab has gone through many generations of people. Each time, the attitude has been fun, yet focused on figuring things out. These people include Tommy Angelini, Karen Kasza, Dave Vader, Cliff Brangwynne, Andy Utada, as well as current bio-types. Among these, David Vader's work on collagen and cells most closely paralleled my own and I particularly benefitted from this interaction. There have also been lots of visitors to the bio-group: in particular, Andrew Stein and Stefan Lindström have been great collaborators. I have also gotten help from many other people in the ginormous Weitz Lab. For most questions that I encountered, there was someone in the lab who could help. I have relied pretty heavily in this respect on the late-night, lab workers. In addition, the lab has had a constant stream of really cool people that are fun to have a beer with and discuss science or life. These people are too many too name and I will inevitable leave someone out.

Fred Mackintosh is a fantastic theorist that I have had the pleasure of working with for several years. Although we have often had disagreements about the physics in these systems, his critical analysis of my work has encouraged a level of rigor that I would not have achieved otherwise. In his lab, I have most closely worked with Chase Broedersz. Throughout my PhD studies, he was always a good person to discuss any crazy ideas with or bother with basic questions about biopolymer theory. I really value our many great discussions!

I would like to acknowledge my various family members. My father has, more than anyone, shaped who I am as a person and equipped me with the tools necessary to be a scientist. In addition, he has directly helped my graduate research by asking good questions, helping me solve problems and encouraging me to be fearless in pursuing the answer. I would also like to acknowledge Mona Rozovich, whose behind-the-scenes efforts may seem to go unrecognized, but they are not unrecognized and, without this effort, things would not be as great as they are. My awesome sister Niki understands me better than almost anyone, she is truly my buddy. Lastly, I would like to thank my mother for her support through the emotional roller coaster of grad school. She has always dedicated everything within her power to help me find a solution to whatever challenge currently lies ahead of me.

I acknowledge Stefan, my dad and Mona Rozovich for doing the work of carefully reading this thesis. I know this can be tedious (and probably boring), but I greatly appreciate their efforts!

I have left the most complicated person to acknowledge last: More than any other person, the person who has most directly impacted my work (and life) in grad school has been Stefan Münster. We have had a ridiculous amount of fun in lab, building stuff together, figuring things out and even writing our papers. Not only has this been fun, together we have gained energy from the other one and been able to push things further than either of us could have done alone. This attitude has also extended into our personal lives where we together explore many of the other awesome aspects of life.

Part I

Introduction

Chapter 1

Introduction to this thesis

The mechanical properties of fibrin networks are of clear importance: Fibrin is the structural protein that comprises the scaffold of blood clots, which stop bleeding at a site of vascular injury; however, blood clots are also implicated in the leading causes of deaths worldwide due to cardiovascular diseases, such as heart attack and stroke.

In the first two parts of my thesis, I present my work elucidating the complex mechanical properties of fibrin networks. Fibrin assembles into a fibrillar meshwork that is the major structural constituent of blood clots, and its mechanical properties are essential for its function in the body. Like many other biopolymer networks, fibrin networks exhibit the intriguing mechanical feature of strain-stiffening: As the network is sheared to small strains, its response is low and linear while at higher strains, its stiffness increases non-linearly with increasing strain. However, by contrast to the well understood intracellular biopolymers, fibrin networks are composed of stiff biopolymer fibers whose nonlinear mechanics are governed by different underlying

physical principles that have so far remained elusive (Weisel, 2008).

Here, I develop an experimental approach to directly observe the physical mechanisms underlying the feature of strain-stiffening (for the first time in any biopolymer network). I quantify the microscopic deformations of fibrin networks as they are being sheared using confocal microscopy and subsequent image processing. I discuss these experimental and analytical tools in the first part of my thesis on image processing and in the material and methods section. In the second part of my thesis, I use these tools to quantify the microscopic behavior of the networks: Specifically, I measure the non-affinity of the motion, the strain across the individual fibers, the role of fiber alignment, and then I estimate the shear stress one would expect if the fibers were to behave like linearly elastic beams. From these data, I develop a physical understanding that elucidates the origin of fibrin network mechanics.

In the third part of my thesis, I utilize this novel understanding of fibrin mechanics to investigate the mechanical alterations induced by platelets. Platelets are small cells that circulate in the blood stream. During blood coagulation, these cells adhere to and contract a fibrin network. It is known that they alter the mechanics of fibrin clots, and their mechanical role is thought to be essential for blood coagulation. However, the exact mechanism through which these alterations occur has remained elusive. Utilizing our knowledge of fibrin mechanics in the absence of platelets, we can now start to investigate and explain many aspects of this interesting problem.

Chapter 2

Fibrin

Fibrin is a biopolymer that polymerizes at the site of vascular injury in the body. It forms an interconnected network of fibers that serves as the major structural component of blood clots. The function of a blood clot is in part mechanical: It must stem the flow of blood to stop bleeding. For this reason, the structure and mechanics of fibrin clots have been studied extensively for decades by scientists and clinicians (Weisel, 2004). Abnormal mechanics or structure of fibrin networks have been correlated with disease states, and the mechanical perturbation of fibrin clots is of great interest to treating thrombus (Weisel, 2004). Moreover, the exact microscopic interactions between the monomers that comprise the fibrin fibers have also been extensively studied.

In this chapter, I review the history of fibrin, its structure, its basic mechanical properties, and the current models that describe its mechanics.

2.1 Formation and structure of fibrin

Fibrinogen, the pre-cursor to the fibrin monomer, circulates in the blood at a concentration around 2.5mg/ml in healthy individuals (Weisel, 2004). In the body, the enzyme thrombin is activated as part of the coagulation cascade. This enzyme, a serine protease, cleaves two fibrinopeptides from fibrinogen converting it from fibrinogen to fibrin monomer. When these two areas are cleaved, the fibrin monomers can associate with one another and start to polymerize. They initially form protofibrils that lengthen, associate to form the thick fibrin bundles, and branch to create the final network. During the polymerization process, thrombin also converts the transglutaminase, factor XIII (FXIII), to its active form, factor XIIIa. After the fibrin fibers have assembled, factor XIIIa catalyzes the formation of covalent bonds between fibrin monomers. In the lab, we mimic the process of blood coagulation by directly adding purified, activated human thrombin to a fibrinogen solution in the presence of FXIII (see the material and methods section for the exact protocol). The final fibrin structure exhibits a branched and interconnected structure of relatively straight polymer segments. Furthermore, by adding a small fraction of fluorescently labeled fibrinogen, we can visualize the final structure of the fibrin network in a confocal microscope (see fig. 2.1).

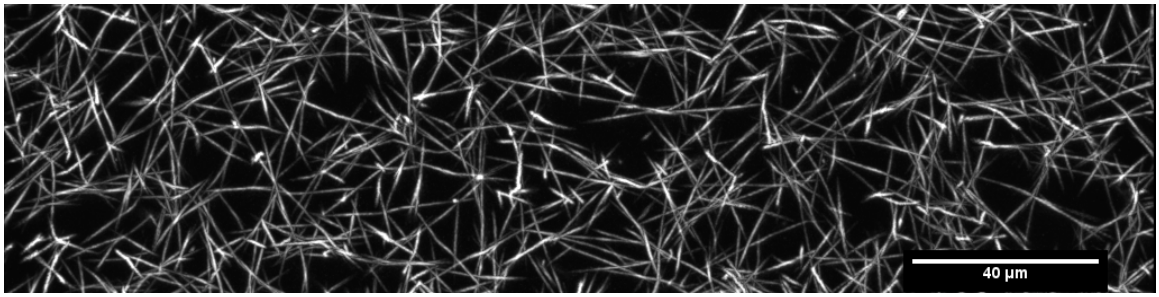

(a) 0.2 mg/ml sample

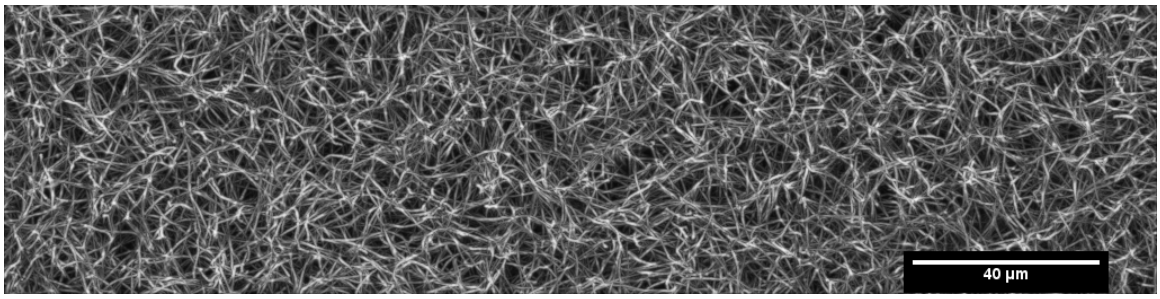

(b) 1.6 mg/ml sample

Figure 2.1: Maximum projections of networks at two different concentrations

2.2 Mechanical properties of fibrin gels

2.2.1 Basic mechanical properties of fibrin networks

To probe the mechanical properties of fibrin, we polymerize the network between two plates in a rheometer. We monitor the mechanical response of the network as it polymerizes by imposing a very small oscillatory strain and measuring the resultant stress. The amplitude and phase lag between the imposed strain and resultant stress can be used to find the storage modulus, G', as well as the loss modulus, G". The first value characterizes the elastic portion of the response while the second value characterizes the dissipative or loss portion of the response. Moreover, by examining the ratio between these two, we can establish whether the sample is highly elastic,

highly viscous, or a combination of both.

As the network polymerizes, we monitor both G' and G". At small times, G' and G" are both low and roughly equal. At around $5 - 10$ minutes, both values begin to increase with G' increasing more rapidly than G". At long times, these values level off to constant values. This indicates that the network polymerization is complete. The long term elastic modulus corresponds to the low strain linear modulus of the material, G_0. This represents the stiffness of the gel when it is sheared to small strains. In fibrin samples, once polymerization is complete, G' is much greater than G" indicating that the sample is very elastic. In highly elastic samples such as this one, the stress required to deform the network, σ, is directly proportional to the degree to which the network is deformed, γ.

$$\sigma = G_0\gamma \tag{2.1}$$

For many samples, this value is considered the stiffness of the network. In many previous studies of fibrin mechanics and most of the characterizations done by physicians, this is the primary value they measure. However, in the studies we present in this thesis, we are also concerned with the higher strain response of the network. To measure this, we impose a steadily increasing strain at fixed strain rate while measuring the resultant stress.[1] The network exhibits strain-stiffening: At low strains, the response is low and linear. As the strain on the network is increased, the sample shows an increased stress that increases with increasing strain. We call the transition

[1]Most materials show a dependence on the rate at which they are probed. Fibrin that has been crosslinked by FXIII (such the ones we study in this thesis) does not show a rate dependence.

point between these two regimes the characteristic strain, γ_c (see fig 2.2)[2]. The exact value of γ_c varies with fibrin concentration, with higher concentration networks showing an earlier γ_c.[3]

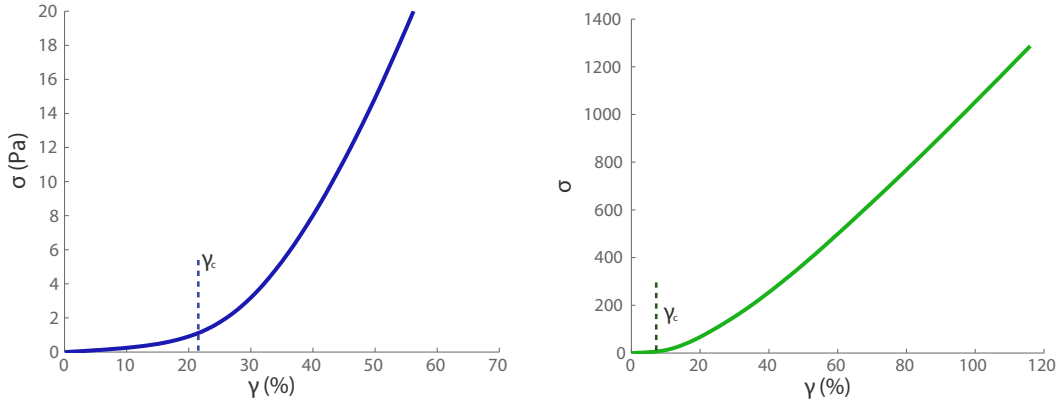

(a) 0.2 mg/ml sample

(b) 0.8 mg/ml sample

Figure 2.2: Stress-strain response of two fibrin networks at different concentrations

The slope of this curve at low strains corresponds to the low-strain stiffness, G_0 we measured during network polymerization. We can similarly determine the stiffness of the gel at all strains by measuring the differential modulus, $K'(\gamma)$. This is just the derivative of the stress-strain curve at all strain points, $K' = \frac{\delta\sigma}{\delta\gamma}$. We calculate this for the stress strain curve we obtained for fig. 2.2. At low stress, the sample shows a constant response corresponding to the initial linear modulus, G_0 of the sample (see fig. 2.3 regime 1). As the stress increases, the sample stiffens non-linearly until it reaches a plateau at very high stresses(see fig. 2.3 regime $2-3$). We denote this high

[2]There is no strict rule about how γ_c should be defined. To avoid difficulties with the exact definition of γ_c, in this thesis I try to compare any changes I measure to the entire trace of the stress-strain response of the network.

[3]See the materials and methods section to find the exact strains, strain rates and protocol used.

strain modulus with, K'_{high}. For higher concentration samples, there may be a final regime, at very high stress, where the network, again, shows a stiffening response (see fig. 2.3 regime 4). The differential stiffness K' is useful because it more clearly

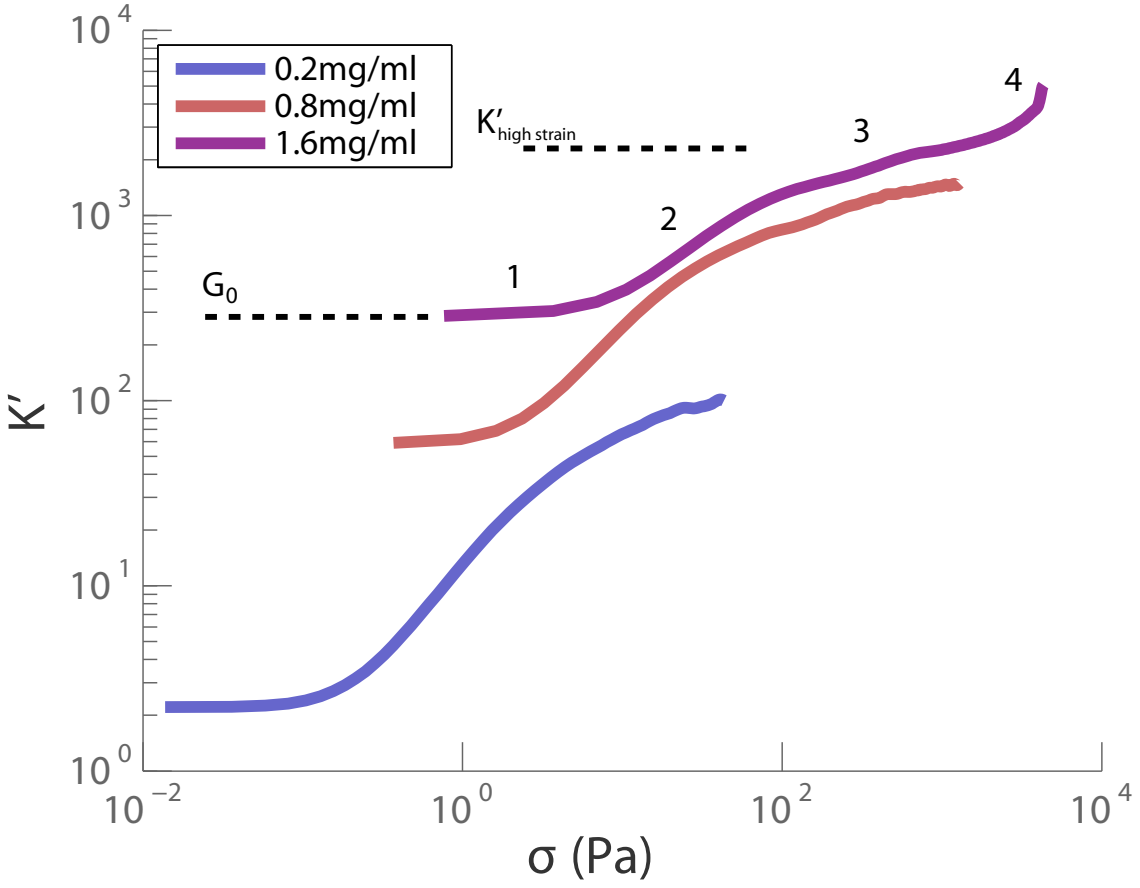

Figure 2.3: Differential modulus of three different concentrations of fibrin networks

highlights how the network response changes. For instance, from this measure, it becomes clear that the stress response of the network does not stay highly non-linear in strain but actually slows down and almost becomes linear again at high stress (resulting in the almost constant high strain modulus, K'_{high}).

2.3 Review of individual fiber mechanics

I address the mechanics of the individual fibers in chapter 10 and section 10.2. In short, studies have measured the force-extension curve of individual fibers to be linear up to strains beyond 1 with Young's moduli around $\sim 10MPa$ using atomic force microscopy. At strains beyond 1 the individual fibers exhibit strain-stiffening.

2.4 Current models of fibrin mechanics

I will review the most prominent models of fibrin mechanics that currently exist. Most of these models assume that an individual fiber or unit cell shows a strain-stiffening response, and the bulk mechanical response is a direct extension of this behavior.

Lastly, I describe a model which has been prominently applied to fibrin, but is not so much a model as work based on a simulation.

2.4.1 Strain-stiffening arises from an attenuation of thermal fluctuations

A prominent model in biopolymer rheology considers networks of semi-flexible fibers that undergo significant thermal flucuations (MacKintosh et al., 1995). When these fibers are stretched, this model predicts that their thermal fluctuations are attenuated, and the force required to stretch them increases. The network is modelled as deforming affinely so the bulk network properties become an extension of the individual fiber behavior and also exhibit a stiffness that increases with elongation. This

model was first applied to fibrin networks in 2005 by Storm *et* al. (Storm et al., 2005). More recently, this model was extended by Piechocka *et* al. to include the more complex structure of an individual fiber (Piechocka et al., 2010). In this study, the authors model individual fibrin fibers as loose bundles of thermally fluctuating protofibrils. Since the protofibrils are loosely coupled, the resulting fibrin fibers have a low persistence length and, therefore, exhibit significant thermal fluctuations. Like the original model, this model predicts that the fibers strain-stiffen owing to an attenuation of their thermal fluctuations as they are stretched. By assuming that the network deforms affinely, the authors of this study attribute the strain-stiffening of the bulk network to the strain-stiffening of the individual fibers (Piechocka et al., 2010).

2.4.2 Strain-stiffening arises from forced-unfolding and exposure of hydrophobic domains in the fibrin monomer

Brown *et* al. stretch a high-concentration fibrin network and measure its mechanical response. They discovered that as such a network is stretched, there is a large degree of associated water expulsion. Brown *et* al. proposed that as the individual fibrin fibers that comprise the network become aligned and stretched, their constituent monomers are forced to unfold and expose hydrophobic regions. These hydrophobic regions then associate leading to the large degree of water expulsion. They modeled the network-level mechanics as a direct extension of the mechanics of an individual unit cell. Their model attributes the mechanics of this unit cell and, thereby, the resulting bulk network to this process of forced unfolding of the

monomers and corresponding water expulsion (Brown et al., 2009).

2.4.3 High-strain network mechanics arise from the worm-like chain extension of the fibrin backbone

In this study, Hudson et al suspended small quasi-$2D$ fibrin networks with $\sim 10s$ of fibers over small transparent grooves on glass substrates. They pulled on one of the fibers to deform the entire network while simultaneously measuring the force using atomic force microscopy (AFM) and observing the deformation using microscopy. They were primarily concerned with the high-strain behavior of the network. They measured the strain in all of the fibers in the network. They found that to match the high strain behavior of the network, a worm-like chain model of an individual fiber, in which an individual fiber behaves non-linearly, was necessary (Hudson et al., 2010).

2.4.4 Strain-stiffening arises from a bending to stretching transition

In this study, Onck *et* al. simulated $2D$ networks of athermal fibers that are sheared. They found that at low strains, the network deforms using largely bending dominated modes while at high strains, there is stretching dominated behavior. This model predicts that the excess length in the fibers will set the exact point of strain-stiffening. Moreover, fiber alignment is considered very important to this transition (Onck et al., 2005; Kang et al., 2009). In an experimental study, the behavior of fibrin was compared to the behavior of the simulated network of Onck *et* al. They found that the degree of fiber alignment was not significant and did not correspond

to the expected stiffening of the gels (Kang et al., 2009). However, they were unable to either confirm or rule out many predictions made from these simulations.

Chapter 3

Platelets

Platelets are small, disc shaped anuclear cells that circulate in the blood stream (White, 2007). During the blood coagulation cascade, they become activated. When this occurs, they undergo a significant shape change and become spiky in appearance (White, 2007). Once activated, these cells will adhere to a fibrin network and contract the structure of the gel as well as nucleate more fiber growth at their surface (Hantgan et al., 1985). Although many of the biochemical interactions that dictate blood coagulation have been elucidated, in the body this is very complex, and many dynamic processes are occurring simultaneously: the fibrin network is polymerizing, platelets are becoming activated and contracting the fibrin gel, other proteins are starting to dissolve the fibrin structure, and the blood and blood vessel walls are undergoing continuous pulsatile deformations. Consequently, previous work to understand this dynamic process has investigated purified platelets, fibrin and other proteins and cells *in-vitro*. From these studies, it is known that platelets significantly alter the mechanics of fibrin gels (both in the presence and absence of other proteins or cells present in

a blood clot). These changes can lead to stiffness changes as great as ten-fold (Lam et al., 2010). By comparing the platelet contraction and stiffness change in diseased versus healthy patients, the mechanical alterations of a blood clot by platelets is thought to be one of the most crucial functions of platelets physiologically. However, the exact physical mechanism underlying these alterations has remained unknown. Elucidating such a mechanism will deepen our understanding of blood clot mechanics as well as impact our view of many cardiovascular diseases.

3.1 Basic mechanical properties of platelet and fibrin composite networks

When platelets are added to a fibrin network, they not only stiffen the network, they also cause a large degree of contraction (a process termed 'clot retraction'). There exists a large range of tests and tools that are used to characterize this process; these include machines that work analogously to traditional rheometers, tools that examine the size of clots over time and assays for the time it takes a wound to stop bleeding (Carr, 2003). These bulk approaches have measured clot retraction times, rates and forces (Lam et al., 2010; Carr, 2003; Schwarz Henriques et al., 2012).

In addition to bulk measurements, several recent studies have started to investigate the force an individual platelet can exert. These studies have reported forces that range from $\sim 1nN$ to 10s of nN using traction force microscopy, atomic force microscopy or the deflection of micropillars (Schwarz Henriques et al., 2012; Lam et al., 2010).

There have been a variety of models developed to explain platelet-induced retraction of fibrin clots over the past decades. These offer a variety of possible mechanisms through which platelets can stiffen fibrin gels, speculating that it may arise from their stiff pseudopodia (Cohen, 1979), a pulling out of slack in the individual fibers (Shah and Janmey, 1997) or as an effect of platelets on fiber polymerization (Chao et al., 1970). The more recent, prevailing view is that platelets reinforce fibrin structure and thus increase its structural integrity (Carr, 2003).[1] Very recently, another study has expanded on this idea (Lam et al., 2010). In this study, Lam *et* al. measured the modulus of individual platelets using AFM. They found that the modulus of these platelets is around around $10kPa$. This is substantially greater than the shear modulus of a fibrin network which shows stiffnesses between $1 - 100Pa$. The authors of this study hypothesized that the platelets act as stiff inclusions in the soft matrix of a fibrin gel thereby stiffening the composite gel (Lam et al., 2010).

[1] As far as I can tell, from both literature review and discussions with other people, this idea is based more on an intuitive understanding of platelet-induced alterations rather than a physical model. Most people intuit that if you stress or strain something it will become stiffer. This is actually not the case for linear materials. (Their stiffness will remain unchanged if pre-strained.)

Part II

Image Processing

Chapter 4

Tracking the structure of a fibrous network

Fibrin forms a branched and interconnected network of fibers (see fig. 4.1). To study the mechanics of these networks, we want to track and quantify the types of network deformations that occur as the network is sheared. We use a confocal microscope to image the full three-dimensional structure of the network at increasing strain points (see fig. 4.1). In this chapter, we describe how we identify the structure of the fibrin network and track its deformation as the network undergoes shear. We break up this problem into two parts. First, we find the skeleton or midline through all the fibers in the initial unsheared stack. This results in the X,Y,Z positions of all the fibers and their connectivity. Second, we note that the connectivity of the network is fixed (the fibers at a branch point do not de-associate and re-associate). So we just track how the initial fibrin structure deforms through the entire shear experiment (as opposed to re-identifying the structure in each shear step).

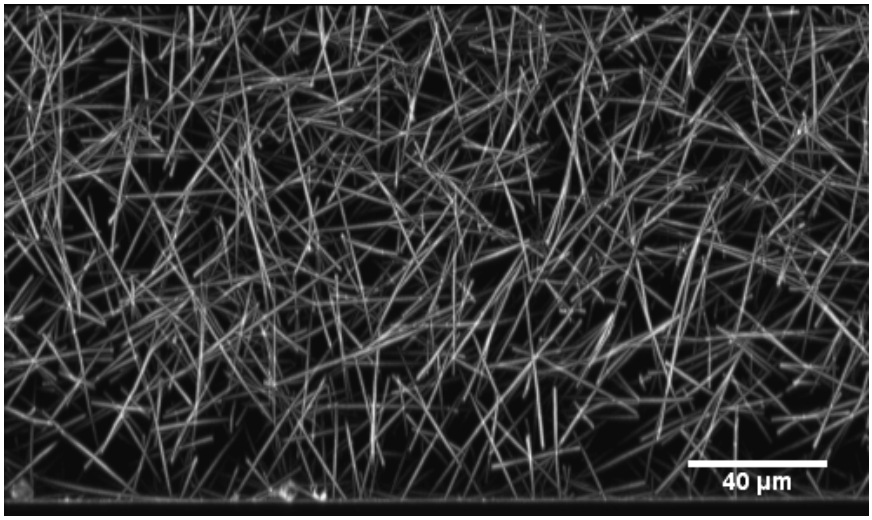

(a) unsheared

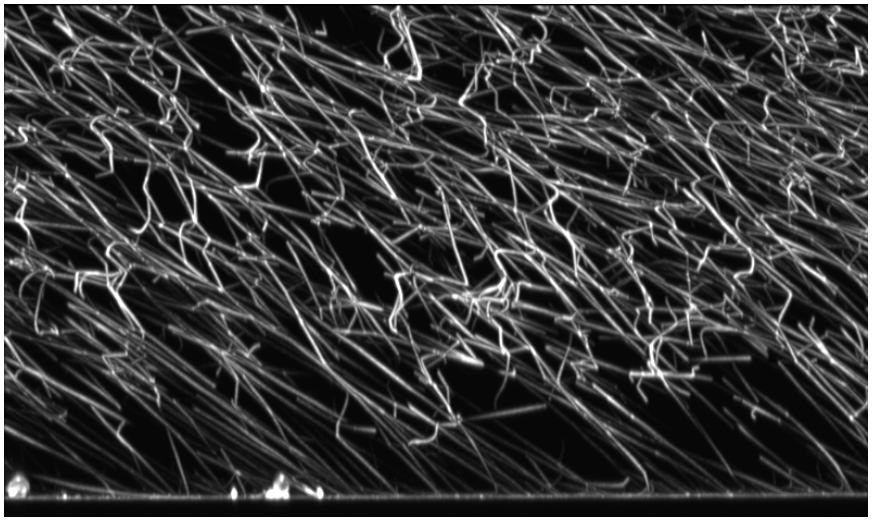

(b) sheared to high strain

Figure 4.1: A Y-Z projection of a typical fibrin network both sheared and unsheared.

4.1 Find 3D skeleton of the network structure

We would like to identify the positions of all the fibers in the network. In general, the fibers do not appear as one pixel thick structures; rather, they are structures with some degree of thickness. We therefore need a method that can, from this data, find

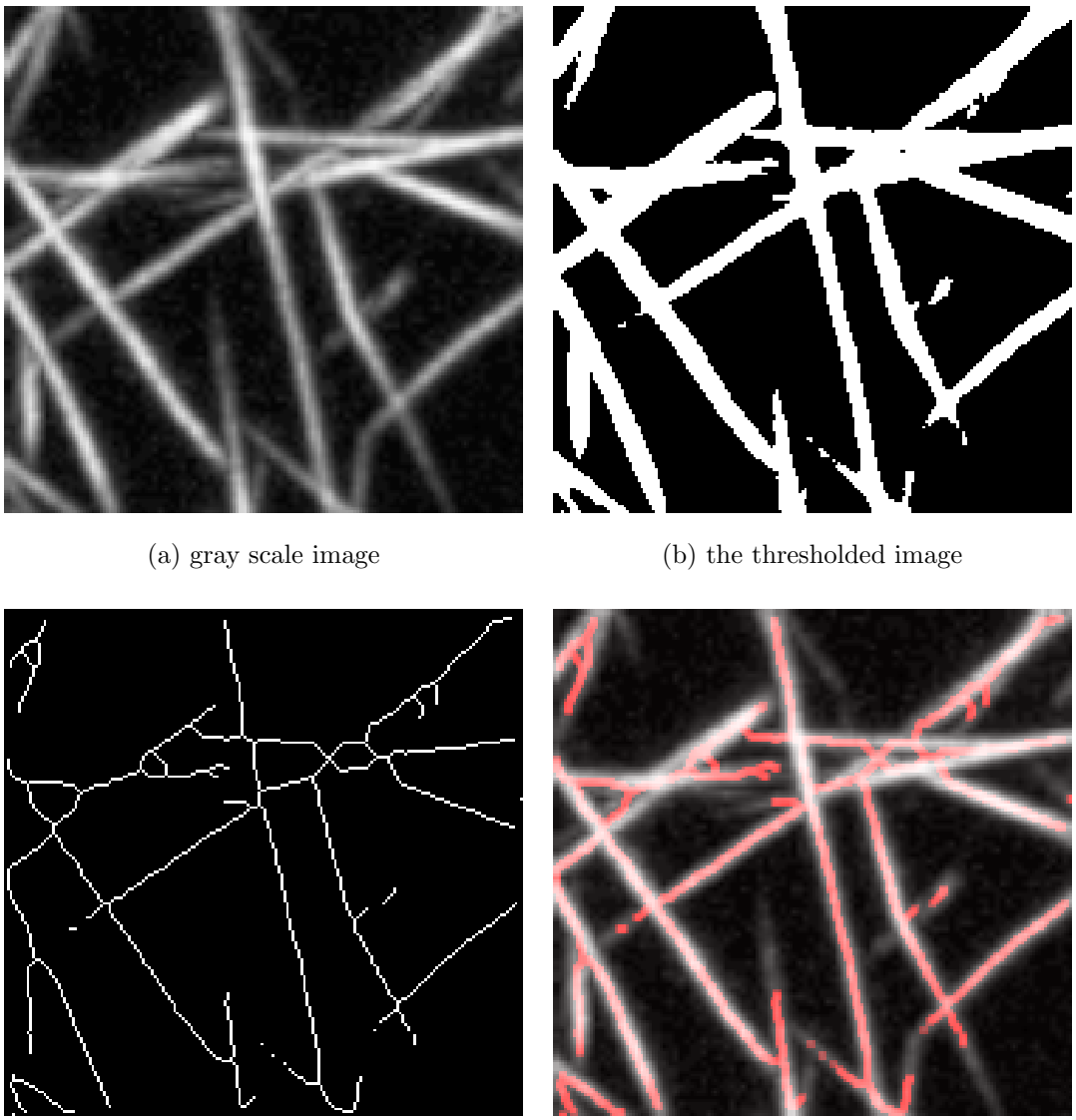

(a) gray scale image

(b) the thresholded image

(c) $2D$ skeleton

(d) skeleton overlaid on original image

Figure 4.2: The original $2D$ image is thresholded to create a binarized image. The skeleton represents the midline through the fibers in the image.

the ''midline'or 'skeleton'through the structure. This may seem like a trivial problem (and in 2D it is significantly easier), but it is actually rather tricky. The current method I use is a homotopic thinning method. I have also designed a homebuilt

method which can only be used for fibrous networks. This may be faster and more accurate; however, since the commercial solution is not prohibitively slow and has been de-bugged by professionals, I currently use that for the skeletonization of these networks.

The homotopic thinning algorithm starts with an image that has been thresholded so that the fibers have a value of 1 and the background has a value of 0 (see fig. 4.2 for a $2D$ illustration of this process and fig. 4.3 for a $3D$ illustration of this process). From this image, the midline of the fibers is found. For the homotopic thinning algorithm, the thresholded image is eroded from the border of the white region until just a one-pixel representation remains. During the erosion, the algorithm checks that the connectivity of the network has not been changed during each iteration of erosion. This is basically a brute-force method; however, with current computers and processers this can be run in a reasonable period of time.

The skeleton of the network is a representation of the X, Y, Z positions of the network structure. After the network structure has been found, branch points are defined as the intersections between three or more fibers. Furthermore, we define a fiber as the line segment connecting two branch points; therefore, we do not account for fibers that appear to persist through a branch point and treat such fibers as two fibers.

4.2 Track structure through several shearpoints

In this section, I outline how to track the structure of a deforming network. I assume that the basic structure and connectedness of the network from the initial

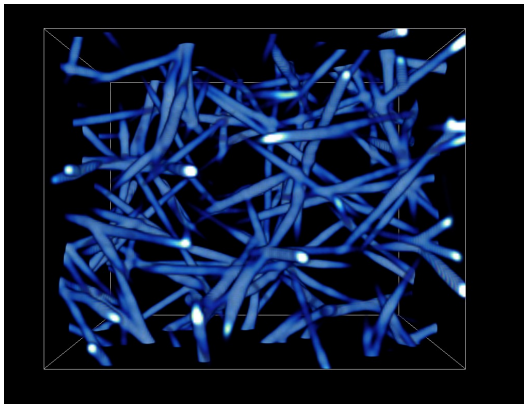

(a) rendered gray scale images

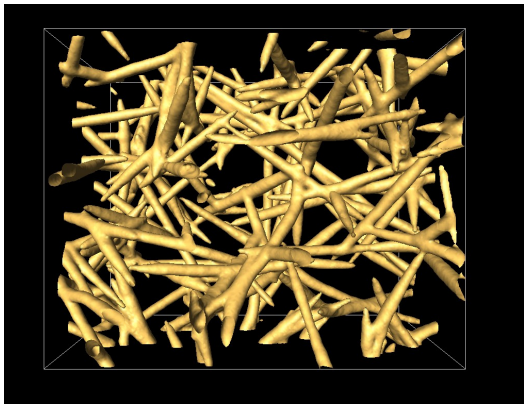

(b) a rendered version of the binarized image

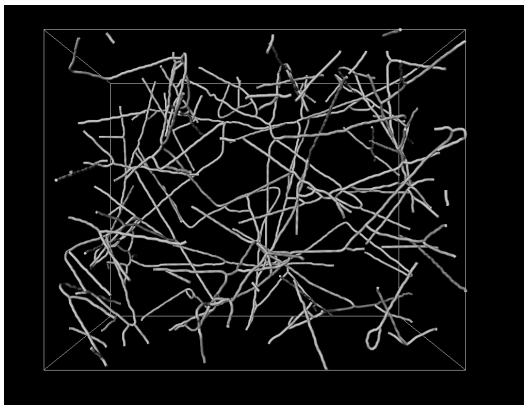

(c) skeleton of the resulting $3D$ structure

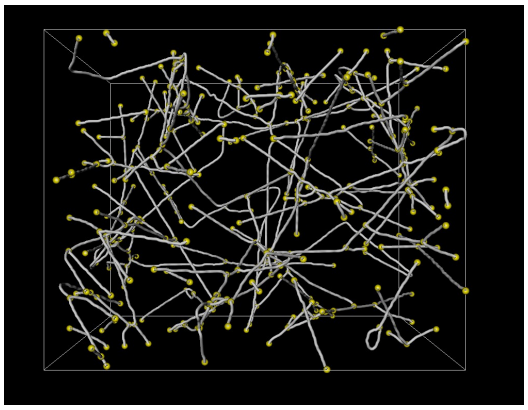

(d) skeleton with the branch points identified in yellow

Figure 4.3: Some rendered versions of the skeletonization process on a small stack in $3D$.

image stack are known. One method of tracking the structure would be to find the skeleton at every shear point and attempt to match the two structures before and after being deformed. However, we know the network does not rupture or associate as it is sheared. For that reason, the number of nodes and how they are connected should remain fixed; however, what *will* change is the exact positions of the fibers and the branchpoints. Consequently, we utilize this fact to track how the structure

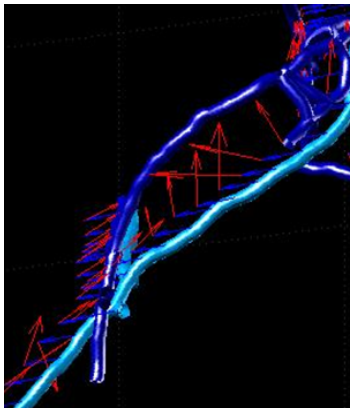

Figure 4.4: Since an individual fiber appears very uniform along its length, a cross-correlation algorithm easily mis-identifies the exact location of its small segments. In this image, the original network is shown in light blue and the sheared network is shown in dark blue. The tracked positions are shown at the of the red arrows. Some of the arrows point to the wrong spot along the length of the sheared fiber.

deforms without re-skeletonizing the network at every shear position. We use a cross-correlation method to take features in the initial stack and find the corresponding point in each subsequent, sheared image stack. Instead of tracking the fibers in the network, we track the individual branch points. Every fiber segment looks very similar to every other fiber segment. Therefore, tracking these segments easily leads to fiber segments being falsely identified (see fig. 4.4. By contrast, the branch points where many fibers join provide excellent features that are easy to follow. Therefore, we use a box centered at each branch point position in the original image stack of intensity values and cross-correlate it with its position in each subsequent stack to find the total motion of the branch point as the network is deformed. We repeat this method for all branch points and all shear positions in the network to track the deformation

of the entire structure.

4.2.1 Cross-correlation

Cross-correlation is a method to find the translational motion between a template box, T, and a target image box, I. The template box represents the feature that we are trying to track while the image box represents the region where we expect to find the feature. In our case, the template box, T, is a box centered at a branch point in the initial stack of intensity values while the target image box, I is the region in the sheared stack (see fig. 4.5)[1].

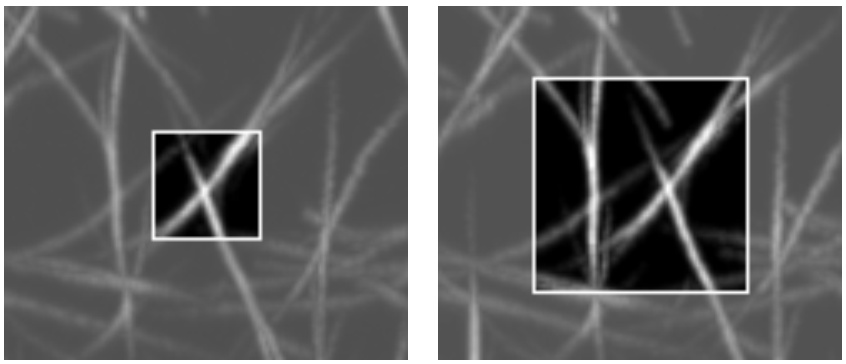

(a) template, T in original stack

(b) target region, I in sheared stack

Figure 4.5: The template image is a small image taken within a larger image in the initial stack. The target image is a larger box size in the subsequent sheared stack.

An image is basically an array of gray-scale values. Keeping this in mind, the basic concept behind a cross-correlation is simple. You translate the image, T, within

[1]Template matching using a cross-correlation is a pretty standard image processing technique. For a more complete review see (Gonzalez et al., 2004)

the larger image, I. For each shifted position, you multiply the value of each point in T with its underlying point in I. Then you sum up these products to find a total for that shifted position. If the original template T is very similar to an area in I, this product will be very high. The higher the value, the better the fit corresponding to the best match within the image. When the cross-correlation is normalized, a perfect fit will have the value of 1. By repeating this procedure for different shifted positions within the target image, the shifted position of the feature with the best match (highest value) can be identified. For each shift, the value of the cross-correlation can be stored in an array where the highest value corresponds to the shift with the best match (see fig. 4.6).

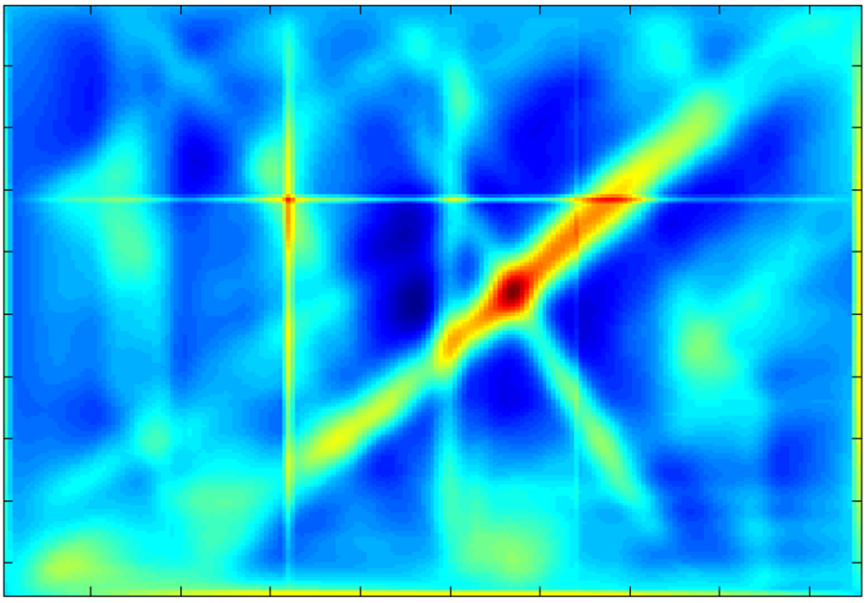

Figure 4.6: The array of cross-correlation values displayed as an image. High cross-correlation values are red and values that are low appear blue. Each point in the image corresponds to a specific shift in x and y between the images I and T.

If the cross-correlation is calculated in this way and normalized, it is described by the following equation for two two-dimensional images,

$$C(x,y) = \frac{\sum_{u,v}(I(u+x,v+y) - \overline{I}(x,y))(T(u,v) - \overline{T})}{\sqrt{\sum_{u,v}(I(u+x,v+y) - \overline{I}(x,y))^2}\sqrt{\sum_{u,v}(I(u+x,v+y) - \overline{I}(x,y))^2}} \quad (4.1)$$

where $\overline{T}$ is the mean of T and $\overline{I}$ is the average in a box the size of T centered at x and y. (The extension of this into the third dimension is straight forward. I have not written this out explicitly to keep eq. 4.1 readable.) The denominator corresponds to the auto-correlation of each function. It normalizes the function so that if the two functions correlate perfectly the result is 1 and -1 if they are perfectly anti-correlated.

Note, a standard deviation is defined as,

$$\sigma_I = \sqrt{\frac{1}{N-1}\sum_{u,v}(I(u,v) - \overline{I})^2} \quad (4.2)$$

where N is the total number of elements, so we can re-write equation 4.1 as,

$$C(x,y) = \frac{1}{N-1}\frac{\sum_{u,v}(I(u+x,v+y) - \overline{I}(x,y))(T(u,v) - \overline{T})}{\sigma_I \sigma_T} \quad (4.3)$$

Calculating this sum at every point in an image can be computationally expensive so, in practice, this is often done using Fourier transformations (Lewis, 1995). To explain how this works, let us consider just two 1-dimensional functions. The discrete (unnormalized) cross-correlation of these two functions is defined as,

$$f \star g[n] = \sum_m f^\star(m)(n+m) \quad (4.4)$$

while the discrete *convolution* between these two is given by,

$$f * g[n] = \sum_m f(m)g(n-m) \quad (4.5)$$

The cross-correlation and the convolution of these two functions is related by,

$$f \star g = f^*(-n) * g(n) \tag{4.6}$$

where * indicates the complex conjugate. Now, if we recall the convolution theorem,

$$\mathrm{F}\{f * g\} = \mathrm{F}\{f\} \cdot \mathrm{F}\{g\} \tag{4.7}$$

The un-normalized crosscorrelation is the numerator of eq. 4.1. We can solve for this by finding the inverse fourier transform. So the cross-correlation is given by

$$CC_{unnormalized} = \mathrm{F}^-1\{\mathrm{F}\{f * g\}\} = \mathrm{F}^-1\{\mathrm{F}\{f\} \cdot \mathrm{F}\{g\}\} \tag{4.8}$$

Using this to calculate the cross-correlation speeds up the calculation significantly.

4.3 Pseudo-code of actual procedure

4.3.1 Initial processing

- We smooth the image stacks with a Gaussian filter.
- To find the total drift that occurs during the experiment, we locate and track the bottom plate. We determine the total intensity of each plane in the image stack. The bottom plate is brighter than the rest of the sample from dye adhered to the surface; therefore, if we examine the total intensity of each plane, we find a peak in intensity centered at the bottom plane. To find the position of the bottom plate, we do not simply assume the plane with the highest intensity is the bottom plate; rather, we use the center of mass of the peak. (This is more robust than the position of the peak height.) After the bottom planes have been

found for all of the stacks, the motion between each plane and each subsequent plane can be found using a cross-correlation.

- If the top plate of the shear cell is within the imaging volume, its motion is determined in the same manner as the bottom plate's motion is determined. If the top plate of the shear cell is not in the imaging volume, an arbitrary slice through the network is assumed to be the 'top plane'. By cross correlating this slice with slices from subsequent stacks, the top plane can be identified and tracked.

- Lastly, using the motion of the bottom plate, we align the stacks so that the bottom appears stationary. (The motion of the top plate is used during the tracking of the network structure as described below.)

4.3.2 Find the $3D$ skeleton through the network

We find the skeleton of the network using the initial, unsheared image stack.

- We smooth images with a Gaussian filter if necessary.

- We determine a threshold intensity value and threshold the image. The threshold should be set to represent the network structure as closely as possible. If it is too low, distinct fibers will merge into one region; if it is set too high, fibers that are one may be broken up into two disjoint units.

- Use a commercially available software to identify the network skeleton (or use another approach).

4.3.3 Track the network structure

- To track the motion of one branch point, we obtain a box, T, of size $32x32x32$ pixels from the original image stack centered at the branch point position. We cross-correlate this box in a larger box, I, of size $64x64x64$ pixels in the target image stack to find the relative motion, u_{rel}, of the box, T, within box, I. Instead of extracting the box, I, centered at the original position, we center it an amount displaced by its expected motion, u_{exp}, between these two time points. In the case of a network that is being sheared purely in the y direction, this corresponds to the affine predicted motion.

$$\begin{aligned} u_{exp,x}(t_{i+1}) &= u_{exp,z}(t_i) \\ u_{exp,y}(t_{i+1}) &= u_{exp,z}(t_i) * \Delta\gamma \\ u_{exp,z}(t_{i+1}) &= u_{exp,z}(t_i) \end{aligned}$$

  where $\Delta\gamma$ is the shear strain between the first and subsequent positions. The corresponding absolute shift between the two boxes is then given as the sum of the relative shifted motion and the predicted motion.

$$u_{absolute} = u_{exp} + u_{rel} \tag{4.9}$$

- We repeat this procedure on every branch point to track their positions from the initial time point, t_0 to subsequent time point, t_1.

- To track the branch point positions in subsequent time point, t_2, we repeat the basic procedure. However, instead of using small boxes from the previous time point, t_1 we use the boxes from the initial time point, t_0. For each branch point,

we compare the initial image, T, with the target image, I, in each subsequent time point, t_2, t_3, t_4.... We repeat this until the branch point is considered 'lost'(defined below). When the branch point is lost, we replace the initial box with a new small box centered at the previous known, good position. If the branch point is still found to be 'lost'after this procedure, it is discarded from any further tracking.

  - A branch point is considered 'lost'if it has moved more than eight pixels from its expected location. (i.e., if $|u_{rel}| > 8$)

- Only branch points taken at least $10\mu m$ from the bottom of the plate are considered in this analysis. In addition, branch points within half a box of the image edge are also discarded.

- Lastly, we assume the mean of I does not change very much in a region the size of T. So we replace the mean of I, which should be calculated for just a region the size of T, with the mean for the entire region of I.

4.3.4 Post-processing

- We correct the structure of the network.

  - The skeletonization algorithm occasionally breaks up a single fiber into two fibers. We re-connect these fibers into one fiber.

  - We remove any fiber loops (a fiber whose end point and beginning point correspond to the same node).

- We fit a line through the X,Y, and Z branch point displacements with respect to their Z position. The slopes of each of these lines define the strain in the X, Y and Z directions.

Part III

Networks undergoing shear

Chapter 5

A quick introduction

In this part of the thesis, I outline quantitative measurements of the structure and motion of fibrin networks as they are sheared. Since all of these measurements are based on the same initial experiment, I will describe it briefly. We create a solution of fibrinogen with a small amount of fluorescent label and factor XIII. We polymerize part of this solution in the rheometer while polymerizing the rest between two glass plates on a confocal microscope. After polymerization is complete, we measure the mechanical response of the network by imposing a steadily increasing strain, γ, on the rheometer and measuring the resultant stress, σ. Simultaneously, to visualize how the network deforms during this experiment, we also shear the network on the confocal microscope by moving the upper glass plate in small strain steps. Between each movement of the glass plate, we obtain a stack of images representing a $3D$ volume in the network. By repeating this until high shear, we obtain a set of image stacks that represents the $3D$ structure of the network as it is strained. We use image-processing tools to extract the structure of the initial network. To track the basic deformation of

the network, we track the positions of all of the branch points in the network (these techniques are described in the section on image processing). This results in a list of node positions at every strain point and their connectivity. Using this, we can now quantify how the network deforms and compare this to the mechanical response we measure using rheometry. This is described in the next few chapters. Most of these quantities have never been measured before in a real system. Consequently, I try to carefully outline my thinking at each point and relate my measurements back to previous measurements, if they exist.

In many of the next chapters, I compare my measurements to those from a network that had deformed affinely. To predict the exact position of an affinely deformed network, I use the initial, unsheared network structure and predict the position of each node in the network using an affine transformation with the shear strain on the network. For example, if a node is initially at the position (x, y, z) and the network is sheared in the y direction an amount γ, the new node position would be $(x, y + \gamma z, z)$ (see the section on non-affine motion for a more detailed discussion of affine motion). Repeating this on all nodes at all strain positions results in a list of affinely deformed positions (and their connectivity remains the same as in the actually deformed case). To calculate a quantity that has deformed affinely, I use the exact same code on this set of data as I did to calculate the quantity on the data that represent the actual deformation.

Chapter 6

Static network properties

In this chapter, I examine the distribution of fiber lengths as well as the connectivity of individual nodes in the initial image stack before the network has been sheared.

6.1 Average fiber length

I define a fiber as the segment that connects two nodes in the network. I define the length of a fiber in two ways. The first uses the fiber arc length, l_{arc} (see fig. 6.1). This is the original length along the backbone of the fiber as we have identified from original image stacks using the skeletonization method (see the image- processing section of this thesis). The resolution of these paths is on a pixel level and may, therefore, not be the most accurate. [1] For the second definition of fiber length, I use the Euclidean distance between the two ends of a fiber, l.

[1]The size of an image voxel is $0.24\mu ms$; therefore, if we have a fiber that is $2\mu ms$ long the extra length due to the pixelated path may be significant.

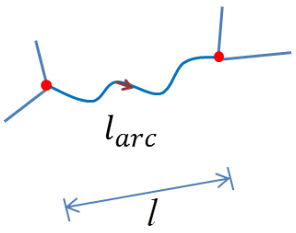

Figure 6.1: The definition of fiber length, l_{arc}, based on the arc length of the fiber and, l, based on the Euclidean distance between its end points.

To find the distribution of fiber lengths, l_{arc}, I determine the total fraction of fibers with a specific arc length, l_{arc}. I disregard all fiber lengths that are smaller than $1\mu m$. Each distribution is initially high at small fiber lengths and decays towards 0 at longer fiber lengths. For increased fibrin concentration, the distribution decays more rapidly (see fig. 6.2 a). I repeat this measurement using the end-to-end length, l, of the fibers. The decay towards 0 becomes slightly more rapid and pronounced for the higher concentration networks, but the basic trend is very similar (see fig. 6.2 b).

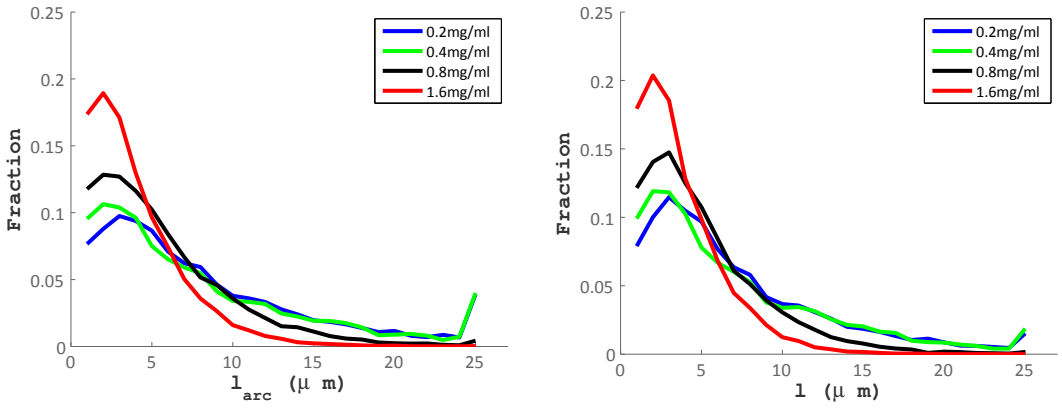

(a) l_{arc} (b) l

Figure 6.2: The fraction of fibers of length l and length l_arc.

A measure which is sometimes more relevant is the total fractional length a given

fiber length occupies. Essentially, it might not be relevant that 99% of the fibers are $1\mu m$ long if this only accounts for 1% of the total length in the network. I therefore examine the length weighted fractional distributions of both l and l_{arc}. (see fig. 6.3). In comparison to the un-weighted length distributions, these distributions look more peaked at slightly longer fiber lengths. The lower fibrin concentrations have a peak which occurs at longer fiber lengths as compared to the higher concentration networks. This is consistent with basic intuition which tells us that lower concentration networks should have longer fibers on average.

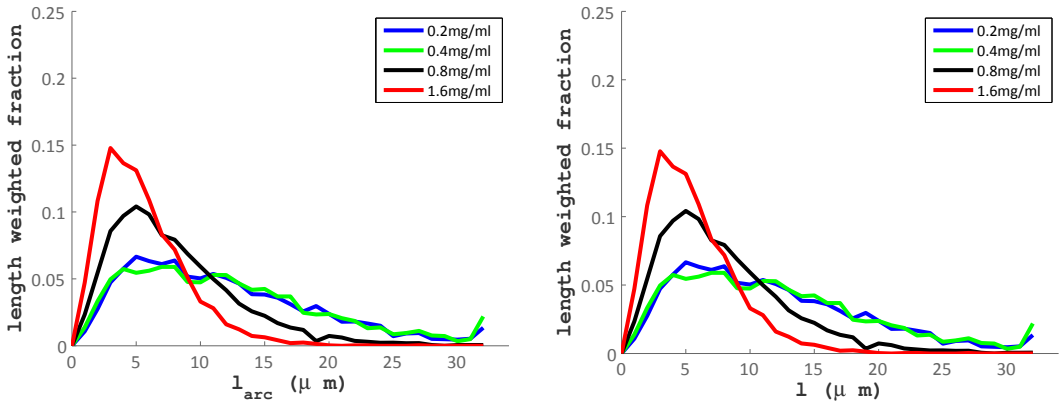

(a) l_{arc} (b) l

Figure 6.3: The fraction of the total length occupied by fibers measured using either their arc length, l_{arc}, or end-to-end length, l.

To determine how curved the fibers are, we compare the ratio of their arc length to their end-to-end length, l/l_{arc}. We find that the fibers are rather straight on average with ratios around 0.9 (see table 6.1).

Lastly, the line density, λ, is an important parameter in many models. This is

Table 6.1: Some characteristic values for the average fiber length and connectivity number. All average lengths are given in μms and the line density is given in $\frac{1}{\mu m^2}$

CONC.	$< z >$	$< l_{arc} >$	$< l >$	$< l/l_{arc} >$	$< \lambda >$
0.2mg/ml	3.07	8.4	7.3	0.91	0.008
0.4mg/ml	3.08	8.2	7.17	0.92	0.009
0.8mg/ml	3.1	5.7	5.15	0.93	0.012
1.6mg/ml	3.20	4.0	3.8	0.95	0.041

defined as the total amount of fiber length in a given volume,V,

$$\lambda = \frac{\sum l}{V}$$

where the sum is taken over all fiber lengths in the volume V. This value represents the total amount of fiber length in a given volume. If the radius of the fibers stays fixed for samples of different concentrations, we expect this value to scale linearly with the concentration. If it does not scale with concentration, it indicates that the radius of the network changes with concentration (see table 6.1).

6.2 Connectivity of the fibers

In this section, I examine the connectivity of the branch points in the network. A branch point is the junction of several fibers. The connectivity, z, of each branch point is defined as the number of fibers that associate at that branch point (see fig. 6.4)

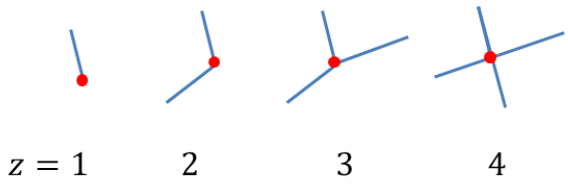

Figure 6.4: Definition of connectivity number of a node.

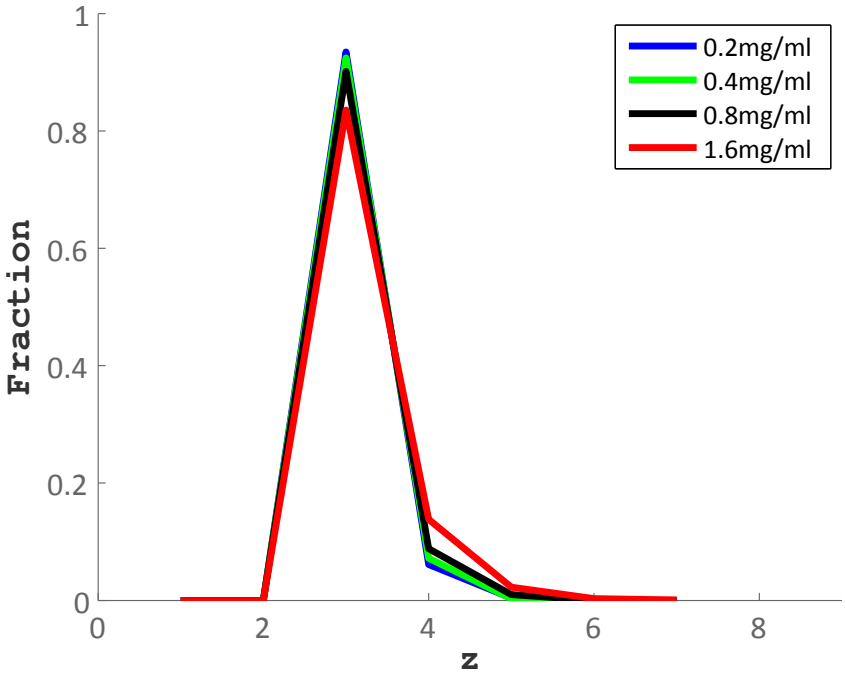

Figure 6.5: Distribution of connectivity numbers for four different concentration networks

We consider $z = 1$ a ''dangling end'and do not expect it to contribute to the mechanical properties of the network and disregard these. Moreover, we assume connectivities of $z = 2$ arise as an error in the skeletonization program which has erroneously divided a single fiber into two (see the image-processing section for more details on this algorithm). Consequently, we identify all branch points with $z = 2$ and join together the two fibers that meet at this point (and, therefore, nodes with $z = 2$ are also be effectively disregarded).

Table 6.2: Fraction of nodes with given z

CONC.	$z=3$	$z=4$	$z=5$	$z=6$	$z=7$
0.2mg/ml	0.9347	0.0611	0.0042	0	
0.4mg/ml	0.9247	0.0719	0.0029	0.0006	0
0.8mg/ml	0.9014	0.0882	0.0100	0.0003	0.0002
1.6mg/ml	0.8355	0.1380	0.0226	0.0032	0.0007

We examine the distribution of connectivity numbers for four different fibrin concentrations. Nodes with connectivity numbers around 3 are responsible for the largest fraction of connectivity numbers (see fig. 6.5). On average, the node connectivity is slightly above 3 (see table 6.1). There are, however, a small but finite fraction of nodes with higher connectivity numbers. These seem to follow a trend with higher concentration networks having a slightly increased fraction of high connectivity nodes (see table 6.2).

The low average connectivity number of these networks is an important clue to understanding the mechanism we think underlies the mechanical response of these networks (see chapter 11 for an explanation of the mechanism)

6.3 Relation to previous work

Similar network properties such as fiber length and branching connectivity have been characterized using scanning electron microscopy images on unsheared fibrin networks (see, for example, (Ryan et al., 1999)). Moreover, the relative size and

branching of fibrin networks taken from both diseased and healthy patients have been extensively characterized using SEM (see, for example, Weisel (2004)). Our results are all similar to those previously reported.

A recent paper has used a similar combination of image and image processing to measure static network characteristics directly from confocal image stacks as we have done here. Their results are also consistent with those we report here (Kim et al., 2011).

Chapter 7

Non-affinity of branch point motion

An important assumption in many current theories or models of biopolymer network mechanics is that the networks deform affinely. This is particularly important for previous work on the strain-stiffening response of fibrin networks (Piechocka et al., 2010; Brown et al., 2009; Hudson et al., 2010; Storm et al., 2005). The basic reason this is important is quite simple: If a network behaves affinely, the position and strain across all the fibers in the network (or an equivalent unit cell) is known, and the mechanical response of the bulk is a simple extension of the mechanical response of the individual fiber or unit cell. In this case, instead of modeling a complex network of interconnected fibers, one can assume the network response arises from an 'average'fiber response. This assumption has proven to be very powerful in understanding the mechanical response of semi-flexible fibers. However, it has not been shown to be the case in stiff-biopolymer networks such as those we are concerned with here.

Moreover, a significant degree of non-affine motion may indicate network motion that may impact the bulk mechanical response.

In this section, I introduce the concept of affinity and different measures of non-affinity that have been traditionally used. I apply these, and variations on these, to measure the non-affinity in fibrin networks as a function of shear.

7.1 Affine and non-affine motion

As a material is sheared, every point within that material moves. If all of the points move as they would in a continuum, they move affinely. For such motion, the top plate imposing the shear moves a fixed distance, d, and every point downwards moves an amount linearly proportional to this amount reaching 0 displacement at the bottom plate (see fig 7.1). The constant of proportionality is given by the shear strain on the system, $\gamma = d/h$, where h is the distance between the top and bottom plates (see fig. 7.1). If the shear is in the y direction, then the shear transformation matrix for this motion is given by,

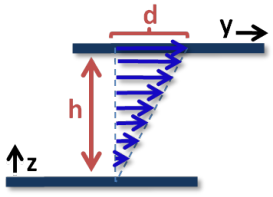

Figure 7.1: During affine shear, every point moves an amount linearly proportional to the motion of the top plate.

$$\Gamma = \begin{pmatrix} 1 & 0 & 0 \\ 0 & 1 & \gamma \\ 0 & 0 & 1 \end{pmatrix}$$

A point in the material at the position, (x, y, z) will then move to the point (x', y', z') given by,

$$\begin{pmatrix} x' \\ y' \\ z' \end{pmatrix} = \Gamma \begin{pmatrix} x \\ y \\ z \end{pmatrix},$$

Written out explicitly for a material being sheared in the y direction,

$$\begin{aligned} x' &= x \\ y' &= y + \gamma z \\ z' &= z \end{aligned}$$

For a network of connected fibers, if a network deforms affinely, each node and fiber in the network will follow this deformation profile as well (fig. 7.2).

Although, on average, the points in a material should behave affinely, every real system will have a degree of non-affine motion. Typically the 'average 'motion of the branch points at each z-height will be affine while the non-affine variation is the spread about this average (fig. 7.2, red line is affine prediction, blue dots indicate the spread from non-affine motion). A larger spread indicates a larger amount of non-affine motion. Different measures of non-affinity can be used to characterize the degree of this spread.

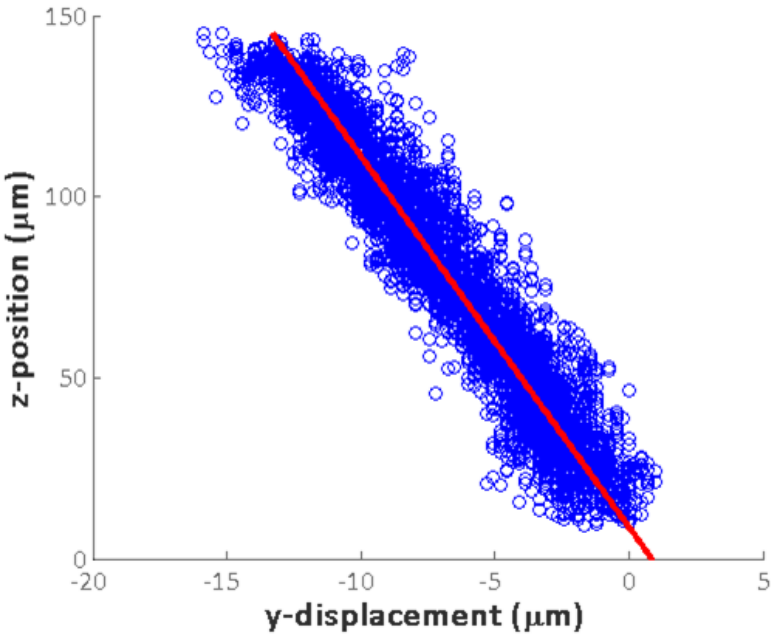

Figure 7.2: The displacement of branchpoints in the y direction at various z-positions (blue). The red line represents the affine motion.

7.2 Different measures of differential non-affinity

To understand the degree of non-affinity in a system, several non-affinity measures have been devised. I review a few of them below. The basic concept behind each of these is to characterize the spread in the non-affine motion. These all start by decomposing the motion, $\overline{u}_{tot}$, of a point in the sample into its affine, $\overline{u}_{aff}$, and non-affine, $\overline{u}_{NA}$, components(see figure 7.3). In this way,

$$\overline{u}_{tot} = \overline{u}_{aff} + \overline{u}_{NA} \tag{7.1}$$

The total motion is defined in one of two ways (with the affine and non-affine motions being defined similarly): either the motion represents the total motion that point has moved since the beginning of the experiment or it is the motion over a small range

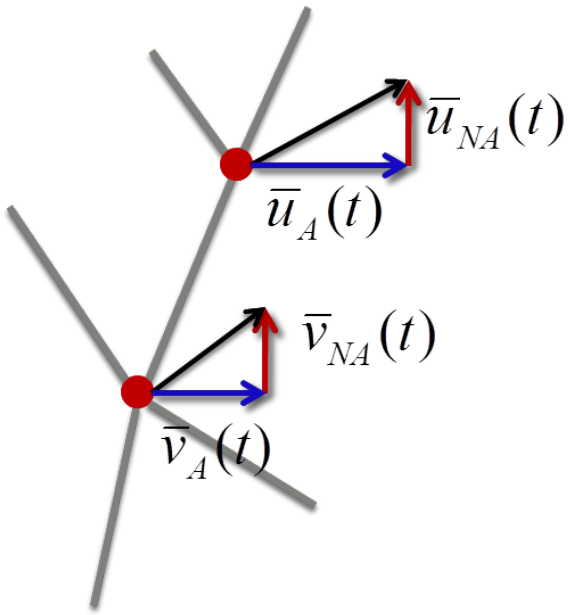

Figure 7.3: The total motion (black) of two branch points is divided up into its affine(blue) and non-affine (red) components.

in strain, $\Delta\gamma$. Measures of the latter type of non-affinity are referred to as measures of the *differential* non-affinity.

A few different common measures of differential non-affinity are outlined below. (To distinguish them, I have given each one a different name based on the original reference or some other feature.) Most of these measures can also be used in squared format to accentuate any peaks that occur (Fig. 7.5). The exact shape of the peak varies slightly, but all measures peak around the same strain (Fig. 7.4).

1. *Fred's*You scale the non-affine motion by the change in strain, $\delta\gamma$, over which you measure the motion of each branch point. This measure can have difficulties in experimental systems when the change in strain is very, very small.

$$\Gamma_{freds}(t) = \sqrt{\frac{1}{N}\sum_{i}\frac{|\ \overline{u}_{NA,i}\ |^2}{\Delta\gamma^2}} \tag{7.2}$$

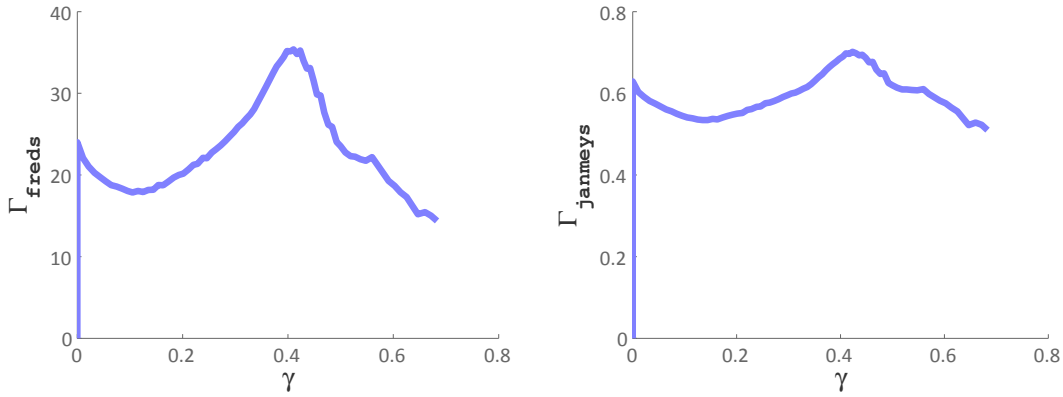

(a) Fred's measure

(b) Janmey's measure

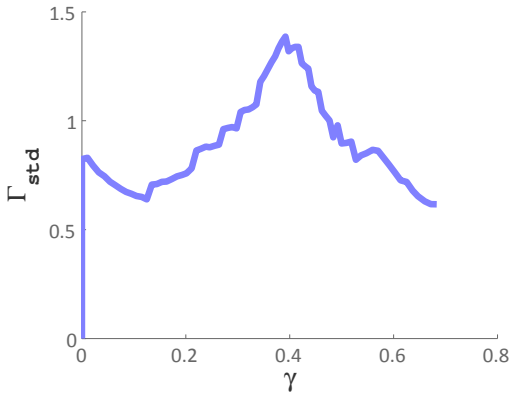

(c) standard deviation

Figure 7.4: Comparison of non-affinity measures.

where N is the number of points tracked.

2. *Standard Deviation* This measure is basically a standard deviation. The definition of standard deviation for a random sample is,

$$standarddeviation = \sqrt{\frac{1}{N}\sum_{i}(x_i - \overline{x})^2} \tag{7.3}$$

where x_i are the measured values and $\overline{x}$ is the mean. For the tracked displacements, the mean at each z height for all the displacements should be the affine

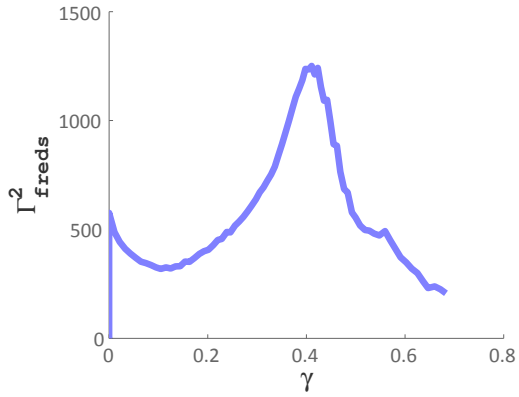

(a) Fred's measure squared

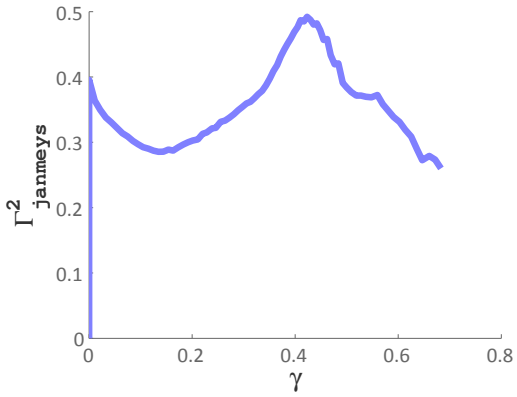

(b) Janmey's measure squared

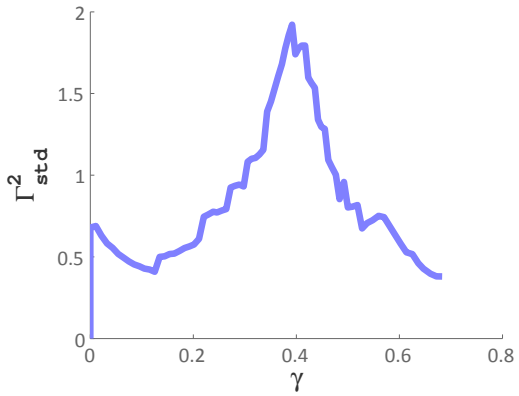

(c) standard deviation squared

Figure 7.5: Comparison of squared non-affinity measures.

predicted displacement (see fig. 7.2 red line). The non-affine component away from this line is the non-affine part of the motion; therefore, to characterize the spread of the non-affine part about this, we just take the non-affine part of the motion and assume the mean motion is 0. The non-affinity measure is then just defined as:

$$\Gamma_{std}(t) = \sqrt{\frac{1}{N}\sum_i \mid \overline{u}_{NA,i} \mid^2} \tag{7.4}$$

3. *Janmey's* Another definition is very similar to the measure based on standard

deviation except the non-affine motion is scaled by the expected affine motion. This definition becomes problematic when the expected motion is very small (for instance, close to the bottom plate where very little movement is expected). This definition has the benefit that it has values that start to make intuitive sense and give a sense of scale. If the non-affine motion is of the same magnitude as the affine motion on average, the value is 1. Modified from (Wen et al., 2007)

$$\Gamma_{janmeys}(t) = \sqrt{\frac{1}{N}\sum_{i}\frac{\mid \overline{u}_{NA,i} \mid^2}{\mid \overline{u}_{aff,i} \mid^2}} \tag{7.5}$$

Very little is understood about non-affine motion and its impact on network mechanics. Moreover, there is a dearth of 'models of non-affinity'. Therefore, it is even difficult to estimate whether the values of non-affinity we measure are significant or not.

7.3 Details of the actual procedure

To accurately calculate this value, I use a few tricks in the actual procedure I implement.

- The actual change in strain from one confocal stack to the next is very small (1%). The motion of each branch point, u_{t_i} is therefore also very small (see fig. 7.6 and 7.7). If you use the motion of all of the branchpoints over one shear step, this results in a very noisy result (fig. 7.8). If you examine the tracks of branchpoints, you notice that there is some variation along the branch point tracks, but the general motion is rather persistent. Consequently, to more accurately measure of the non-affinity of the branch points, it is better to use

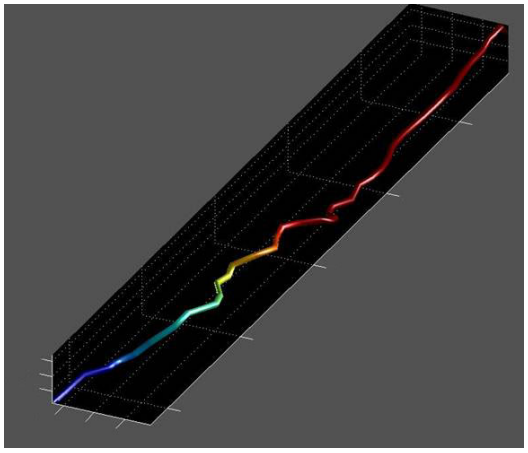

(a) A more affine branch point track

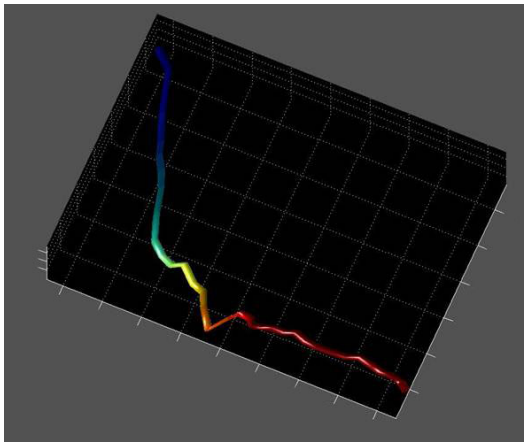

(b) A track which is initially non-affine but then becomes more affine.

Figure 7.6: The tracks of two branch points over several strain steps (blue is early strain and red is later strains.)

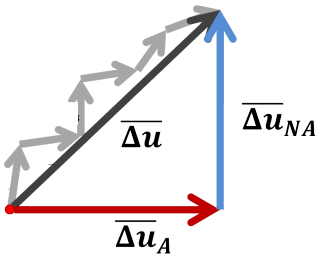

Figure 7.7: The representative motion of one node over several small shear steps.

the motion of each branch point over several shear steps $\overline{\Delta u} = \sum_i \overline{u}_i$ (see fig. 7.7). Moreover, to compare different experiments, where the change in strain between each confocal stack may vary, we find the total motion of each branch point over the number of shear steps, n_s that most closely corresponds to a fixed total change in system strain, $\delta\gamma$.

$$\delta\gamma(s) = \gamma_{s+n_s} - \gamma_s \tag{7.6}$$

Figure 7.8 shows that with increasing $\delta\gamma$ the data appear smoother.

- Moreover, to find the most accurate affine prediction, we use the total motion of each branch point over the small window, $\delta\gamma$, to determine the affine, predicted motion (see fig. 7.7). This will result in the most accurate affine prediction over the strain window, $\delta\gamma$.

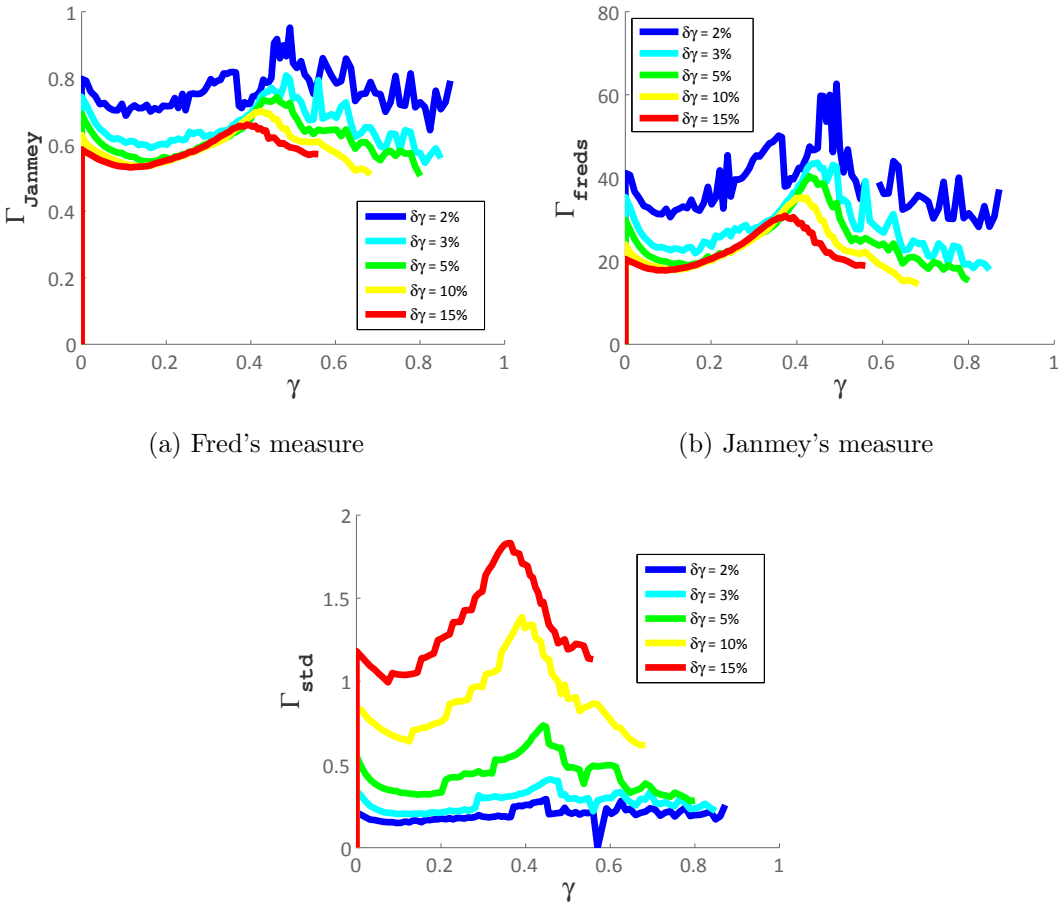

(a) Fred's measure

(b) Janmey's measure

(c) standard deviation

Figure 7.8: Non-affinity calculated for different strain windows

7.4 Results: non-affinity peaks at onset of strain-stiffening

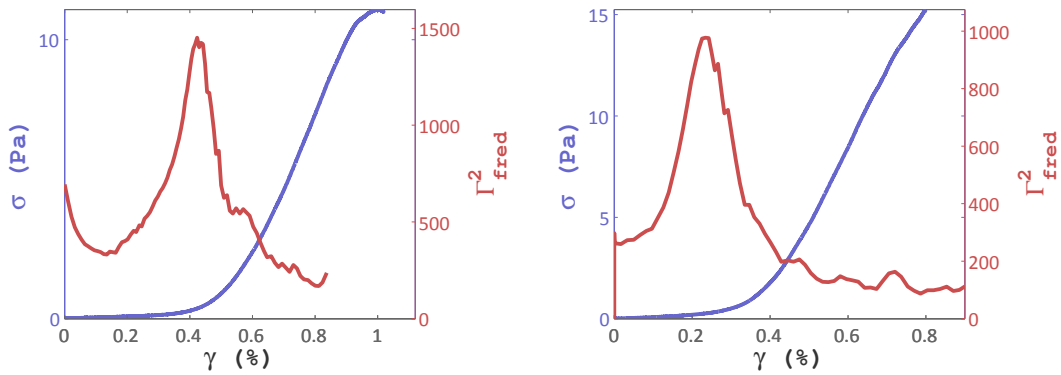

(a) 0.2 mg/ml

(b) 0.4 mg/ml

(c) 0.8 mg/ml

(d) 1.6 mg/ml

Figure 7.9: Fred's non-affinity squared compared to stress-strain response of four different concentration networks.

We sheared and tracked fibrin networks of four concentrations (0.2mg/ml, 0.4mg/ml, 0.8mg/ml and 1.6mg/ml). From the tracked data, we calculate the non-affinity of the branchpoint motion for each of these concentrations over a strain window of $\delta\gamma = 5\%$

(different values of this strain window do not significantly alter the results). We find that the non-affinity peaks around the critical strain, γ_c for each sample although the exact critical strain varies for each sample. In addition, the height of the peaks scale inversely with concentration (see fig. 7.9). [1]

7.5 Comparison to previous work

These results are consistent with a previous study that examined the non-affine motion of beads in a 2.5 mg/ml fibrin network. In this study, Wen *et al.* found a high non-affinity at very small strains that decreased towards 0 with increasing strain (Wen et al., 2007). Considering the trend in our data, we would expect that with increased fibrin concentration the non-affine peak would move to earlier strains consistent with the position of the peak measured in the study by Wen *et al.*

[1] It is often the case that low concentration fibrin networks are initially more non-affine then decrease before increasing again around the onset of strain-stiffening. Non-affine peaks occur in simulations of low-connectivity networks when they transition through different regimes (see the mechanism chapter for the physics underlying these behaviors). This non-affine peak may indicate a first regime where the network behaves differently. It probably occurs at strains that are too small to measure using microscopy but may indicate another interesting behavior. (Moreover, there is an additional stiffness regime that occasionally occurs in the differential modulus of these networks at very low strain. This may hint at the existence of such a regime.)

Chapter 8

Angular distribution

One factor that may be important to the mechanics of fibrin gels is the degree of fiber alignment that occurs during strain-stiffening. In fact, two studies have implicated a high degree of fiber alignment as a crucial cause of the strain-stiffening response of these networks (Brown et al., 2009; Kang et al., 2009).

In this chapter, we examine the orientations of all of the fibers as the network is sheared to different strain points. We find that the networks start out isotropic, and their orientations follow the expectation from an affinely deforming network fairly well.

We also examine the distributions of angles at branch points as the network is deformed. This again looks very much like an affine distribution; however, when we instead determine how these angles *change* as the network is sheared to increasing strains, we get a clear dip in all of the data sets around the onset of strain-stiffening for each network.

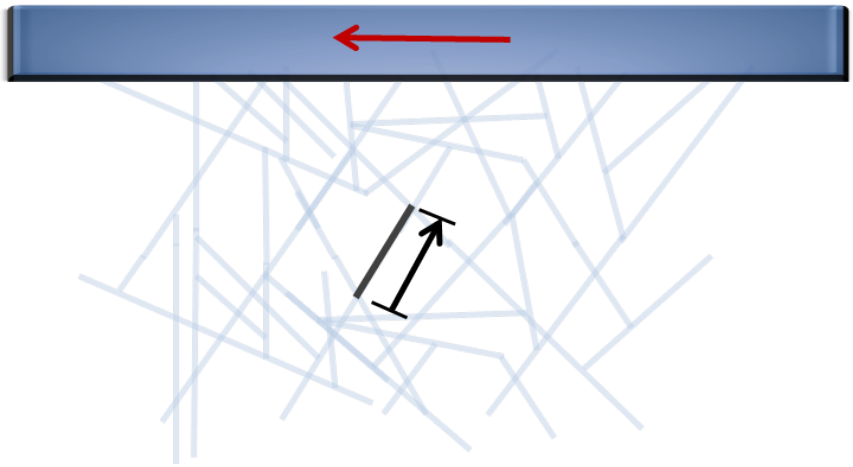

Figure 8.1: For each fiber in the network, we find the vector which connects its end points.

8.1 Orientation of fibers in the network

For every fiber in the network, we find the vector that connects its two end points (fig. 8.1). We find the angle of this vector away from the y-axis, θ, in the $y-z$ plane and its angle away from the x axis, ϕ (see fig. 8.2). This is different from the traditional way of defining these angles, but it is more relevant since we expect the alignment of fibers in the $y-z$ plane to most affect the mechanics of the network (as the primary direction of the imposed shear is in this plane). Although we take the end-to-end *vector* that connects the two fiber end points, a fiber does not have an inherent direction (these vectors simply denote the angle tangent to the fiber orientation). We therefore chose θ so that it ranges from $0 < \theta < \pi$. (Since there is no direction, a fiber that would have had $\pi < \theta < 2\pi$ can always be mapped on to the proper range by taking the equivalent vector with opposite sign.) To determine the fraction of fibers at a given orientation, we evenly segregate the fibers based on their orientation. For each angle, we count the total number of fibers at that angle and

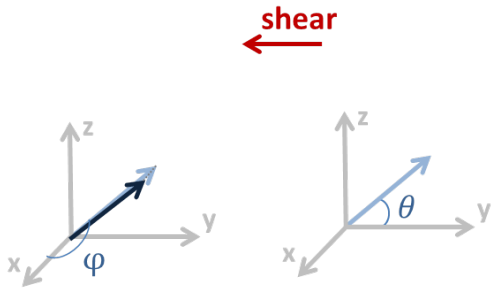

Figure 8.2: The definition of the fiber angles for a fiber. For each fiber in the network we find the vector which connects its end points.

divide by the total number of fibers in the sample. In this manner, we calculate the histogram of fiber distributions that we expect. By repeating this for several shear positions, we can examine how these distributions evolve as the network is sheared.

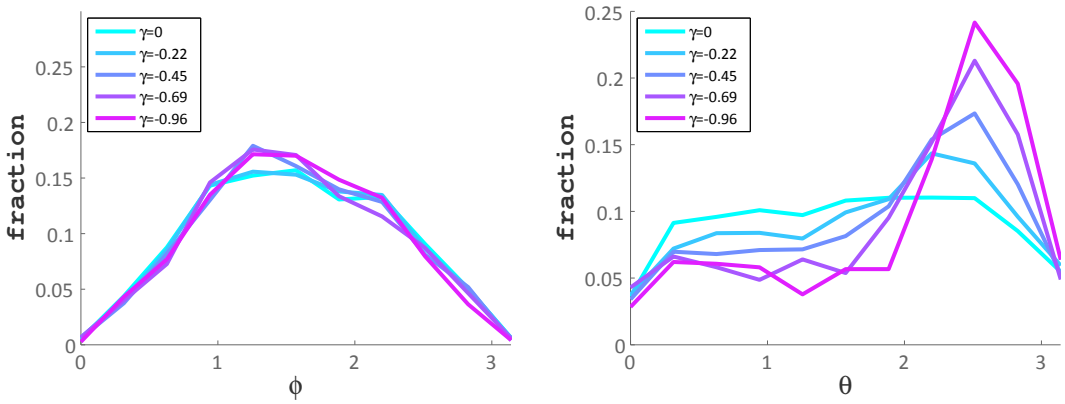

(a) 0.4mg/ml

(b) 0.4mg/ml

Figure 8.3: Orientation of fibers at several shear points for a 0.4mg/ml sample.

The networks exhibit an initially isotropic distribution of fibers which appears as an almost flat distribution of θ and a rounded distribution in ϕ (see fig. 8.3). As the strain on the network increases, a peak develops in θ corresponding to the direction

which undergoes the highest degree of strain (see fig. 8.3). The distribution of ϕ is relatively unchanged. We are interested in understanding whether this fiber alignment

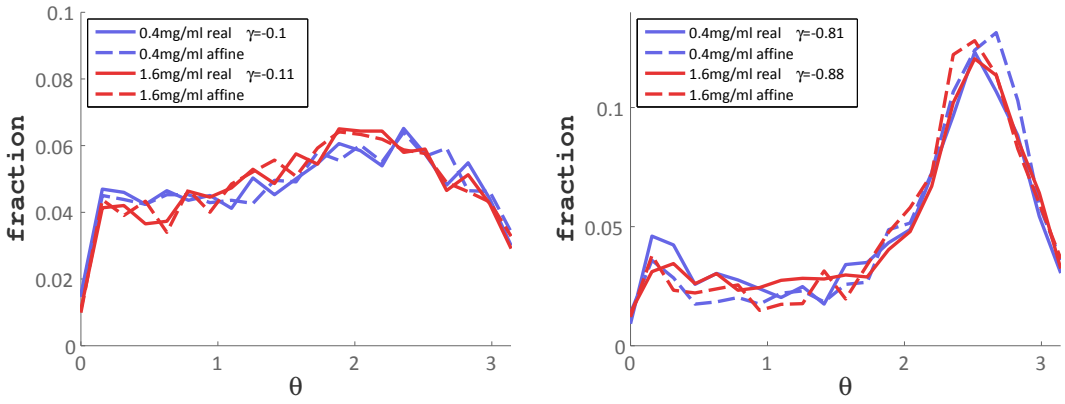

(a) small γ (b) large γ

Figure 8.4: Distribution of fiber orientation, θ, for different concentrations and affine distributions at low and high system strains.

affects the mechanics of the networks. We therefore compare ϕ and θ distributions for datasets that have very different onsets of strain-stiffening, in addition to the distribution we would expect from networks that had deformed affinely. When we compare the data from a low-concentration (0.4mg/ml) sample which has a very late onset of strain-stiffening ($\sim$ 30% strain) to a high-concentration sample (1.6mg/ml) sample which has a very early onset of strain-stiffening ($\sim$ 3% strain), we find that the distributions of θ are very similar for both concentrations as well as to the affine predicted distribution (see fig. 8.4). This the case at both low and high system strains. Moreover, the distribution of ϕ remains basically unchanged between samples, over strain, and in comparison to the affine prediction (see fig. 8.5).

Since datasets with very different mechanical characteristics exhibit orientational

distributions that are all very similar, most likely fiber alignment has little impact on the mechanics of the gels.

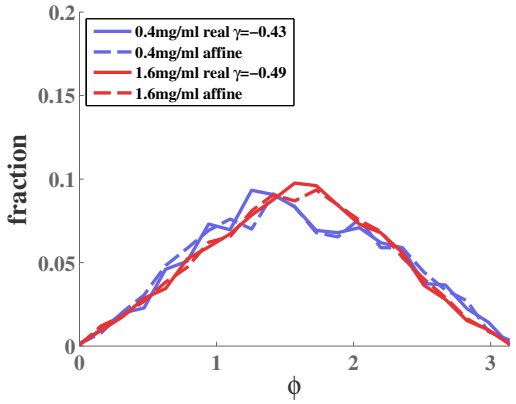

Figure 8.5: Distribution of fiber orientation, ϕ, for different concentrations and affine distributions.

8.1.1 Relation to previous work

The similarity between the angular distributions of the different networks and an affine network is consistent with previous work. An experimental study examined the degree of alignment in fibrin networks using birefringence (Kang et al., 2009). They determined that the degree of alignment did not directly correspond to the onset of strain-stiffening in different fibrin networks. In addition, a simulation of semi-flexible networks compared the angular distributions between networks that deformed affinely and those that were allowed to deform non-affinely. These authors found that networks that deformed non-affinely had a slightly higher degree of alignment in comparison to those that deformed affinely (Huisman et al., 2010). Within the resolution of our measurements, it is hard for us to discern such a slight change in

fiber alignment. Regardless, our study demonstrates that there is not a *large* degree of alignment due to non-affine fiber motion.

8.2 Distribution of branch point angles

We examine the distributions of angles between fibers at a branch point. For each branch point, we choose one fiber and find the smallest angle, β_i between that fiber and every other fiber at that branch point (fig. 8.6).

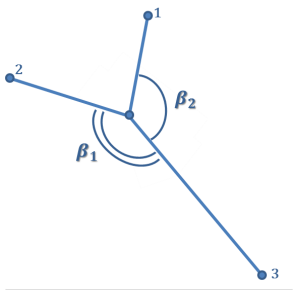

Figure 8.6: Definition of angle, β between fibers at a branch point

We find the distribution of branch point angles, β, at three shear points. We compare the distribution of β in two different concentrations of fibrin as well as their affine expected distributions. In the initial distribution, there is a slight peak in fibers with an angle near π (see fig. 8.7). This is consistent with previous studies that show fibrin fibers branch with a very acute angle (Weisel, 2004). As the network undergoes shear, this peak shifts to slightly smaller angles for all of the concentrations probed. These distributions are very similar to the expected change from an affinely deforming network (see fig. 8.7).

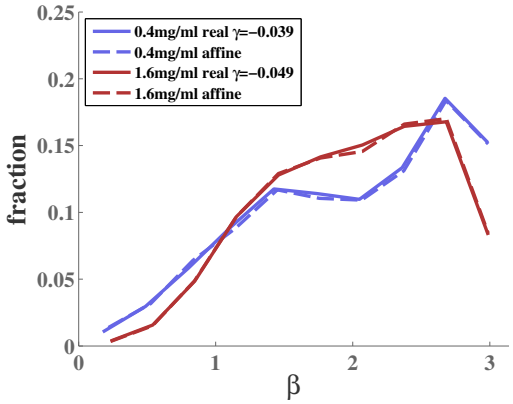

(a) $\gamma \approx 5\%$

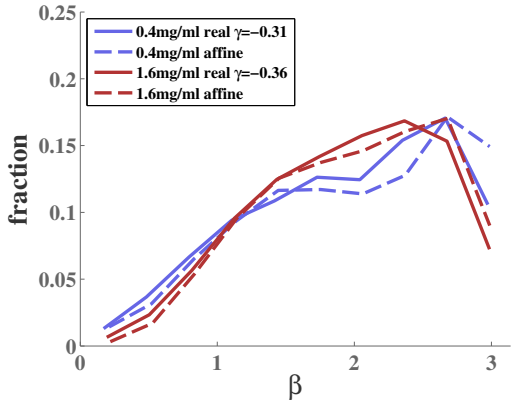

(b) $\gamma \approx 35\%$

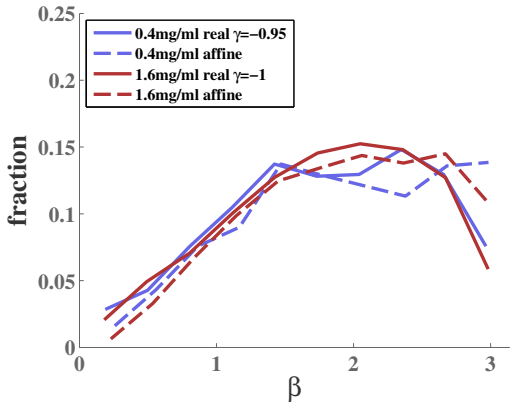

(c) $\gamma \approx 100\%$

Figure 8.7: Distribution of branching angle, β for 2 concentrations and affine distributions.

Instead of examining the distribution of branching angles, we instead focus on the mean change, $< \Delta\beta >$, of this angle at all strain points, γ. We determine this value for four different fibrin concentrations and compare it to the affine expectation. In all but the highest concentration case, there is a distinct dip that coincides well with the onset of strain-stiffening for that sample (fig. 8.8). This suggests that there are a significant number of fibers whose angles change as the network transitions from linear to non-linear network behavior (see chapter 11 to understand how this fits in

with the onset of strain-stiffening in these networks).

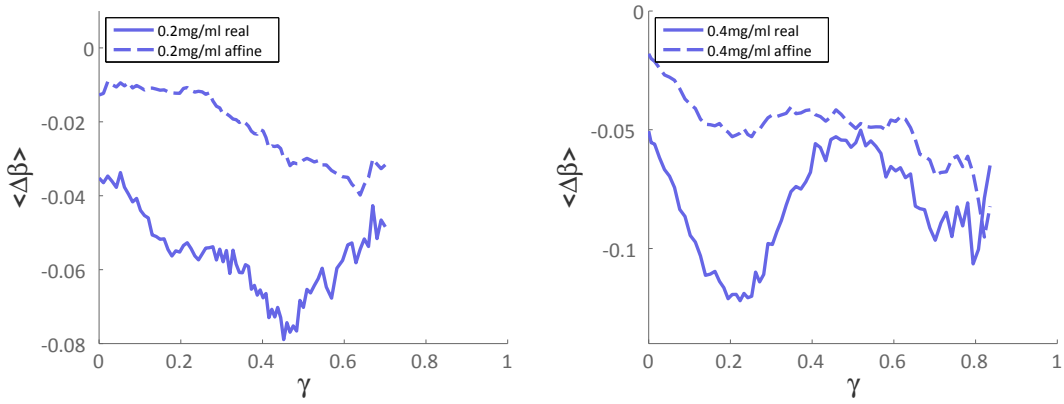

(a) 0.2 mg/ml

(b) 0.4 mg/ml

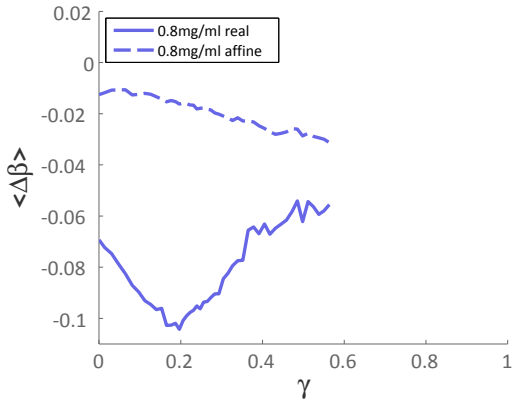

(c) 0.8 mg/ml

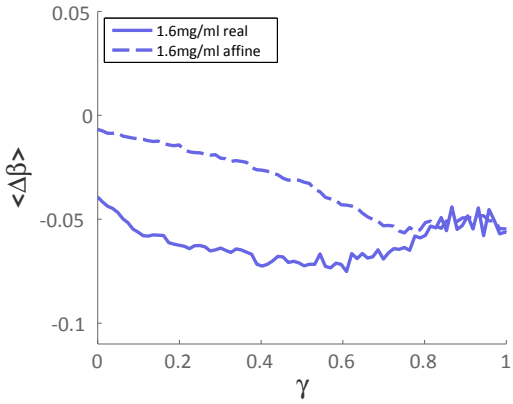

(d) 1.6 mg/ml

Figure 8.8: Mean change in branching angle for four concentrations in comparison to mean change expected for an affine distribution.

8.3 Relation to previous work

As far as I know, there is no previous work that has characterized the angles between fibers at branch points as a (real or simulated) biopolymer network is sheared.

Chapter 9

Strain distribution

As a network is deformed, the individual fibers that comprise the network must deform in concert to bear the load. The stress required to deform the network arises from the force required to strain the individual components. In this chapter, I investigate how strain is distributed in the network. Since the fibers are long and slender, I examine the elongational strain on the fibers. This ignores strains from other contributions such as twisting or bending.

The most insightful piece of data from this chapter is how the average individual fiber strain changes as the network is sheared. By focusing on this relatively simple measure, we find that fibers are on average compressed in the linear regime. By examining the average strain as a function of orientation, we find that fibers that are expected (from an affine prediction) to compress, compress; however, the fibers that are expected to become stretched are actually not stretched until the network enters the non-linear regime. This is important for the mechanism that we think underlies the strain-stiffening response in these networks.

9.1 Individual fiber strain

We assume a fiber is the segment between two branch points (ie we do not account for a fiber that persists through a branch point and treat such a fiber as two fibers). We define the individual strain on a fiber in two ways. In the first method, we use the original arclength of the fiber, l_{arc}, as its rest length (ie. we assume that when the fiber has this length, there is no strain on the fiber (see fig. 9.1)). In the second method, we use the Euclidean distance between the fiber end points (a.k.a. the end-to-end length) of the fiber as the rest length. This overestimates the actual elongational strain (the first method). However, to avoid errors that arise from the measurement of the arc length from the original images, we use the second definition almost entirely throughout this thesis.[1]

In the first case, we define the strain on an individual fiber as,

$$\epsilon_{arc} = \frac{\delta l_{arc}}{l_{arc}} \tag{9.1}$$

where $\delta l_{arc} = l_{e2e} - l_{arc}$ is the change in the current Euclidean distance (or end-to-end distance) between the nodes, l_{e2e} and the original length, l_{arc}. With this definition, all of the fibers must have either a negative or, in the event they are perfectly straight, a 0 strain initially (when the system strain, $\gamma = 0$).

In the second definition, we use the initial Euclidean distance between the two fiber end points, l, as the rest length of the fiber (fig. 9.2). In this case, we define the

[1]This is still very useful although it may seem inaccurate. For instance, we find that the mean strain of the individual fibers is negative at small strains using the second definition. Since this definition *overestimates* the strain, we know the actual strain must be even less.

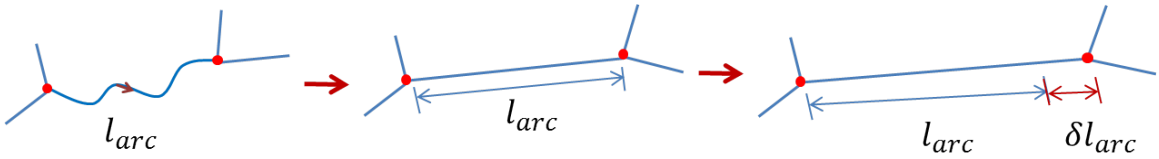

Figure 9.1: When a fiber is first pulled, it must first be pulled taut (so that the end-to-end distance is equal to its original arc length) before there is any actual strain on the fiber.

individual fiber strain as,

$$\epsilon = \frac{\delta l}{l} \tag{9.2}$$

where l is the original fiber length and $\delta l = l_{e2e} - l$ is the change in current end-to-end length and the original length.

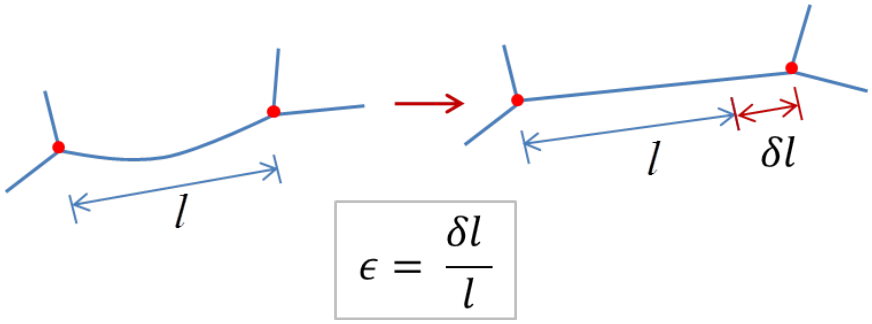

Figure 9.2: The strain is defined as the change in end-to-end length of the fiber scaled by its original fiber length.

9.2 Distributions of individual fiber strains

We examine the distribution of individual fiber strains as the overall network is sheared to different values, γ. We measure the strains for all of the tracked fibers using both measures. To find the distribution of fiber strains, we divide up the number of strains into intervals from $-0.5 < \epsilon < 0.5$ in steps of 0.05 and find the fraction of fibers at each binned strain. We repeat this calculation for every value of system strain, γ. For ϵ_{arc}, we find that the distribution is not centered about 0 initially (as we expect since the initial strain must be non-negative) and spreads out as the overall network is sheared (see fig. 9.3). By contrast, ϵ starts with a peak around 0 and shows a more symmetric broadening as the system strain is increased (see fig. 9.3).

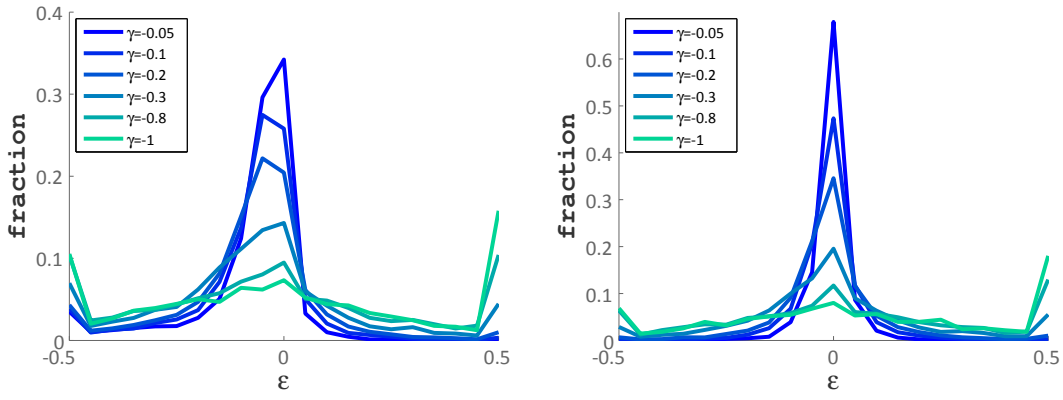

(a) ϵ_{arc} (b) ϵ

Figure 9.3: The distribution of individual fiber strains, ϵ_{arc} and ϵ at different system strains.

This may not be the most informative way to start examining how strains are distributed in the network. We can also look at the fraction of fibers that are compressed or stretched as a function of system strain. We use a small threshold strain of $\epsilon_{thresh} = 0.01$ and treat a fiber with strain greater than this as 'stretched', a fiber

which has less than $-\epsilon_{thresh}$ as 'compressed', and one which is within this threshold strain as having 'no strain'. There is a large number of compressed fibers initially for

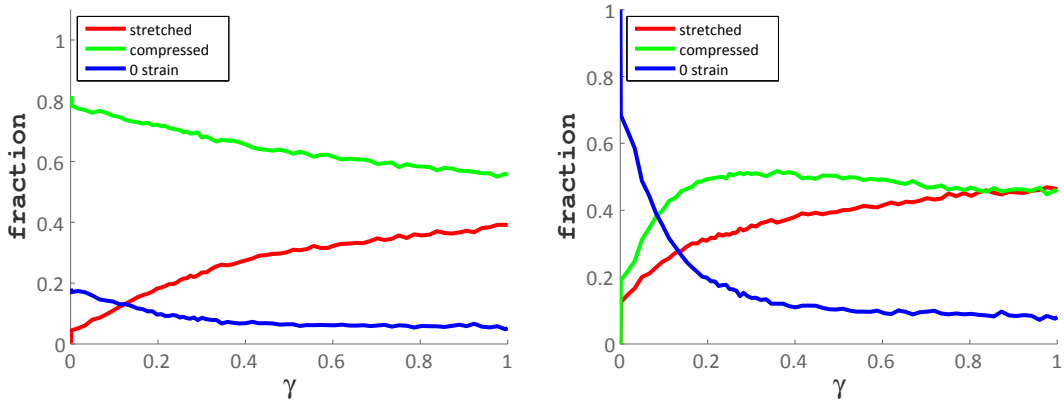

(a) ϵ_{arc} (b) ϵ

Figure 9.4: The fraction of fibers that are stretched or compressed as a function of system strain, γ.

ϵ_{arc} (again, as it must from its definition (see fig. 9.4). That fraction decreases while the fraction of stretched fibers increases, and the fraction of fibers with no strain decreases as well. Similarly, the fraction of fibers for the ϵ definition has a similar trend with all of the fibers starting with 0 strain (again, as it must by its definition (see fig. 9.4)).

If we compare many different samples, we see that with increasing concentration, the number of stretched fibers increases more quickly with increased system strain (see fig. 9.5). This is consistent with their earlier onset of strain-stiffening in the context of the underlying mechanism of strain-stiffening (see chapter 11).

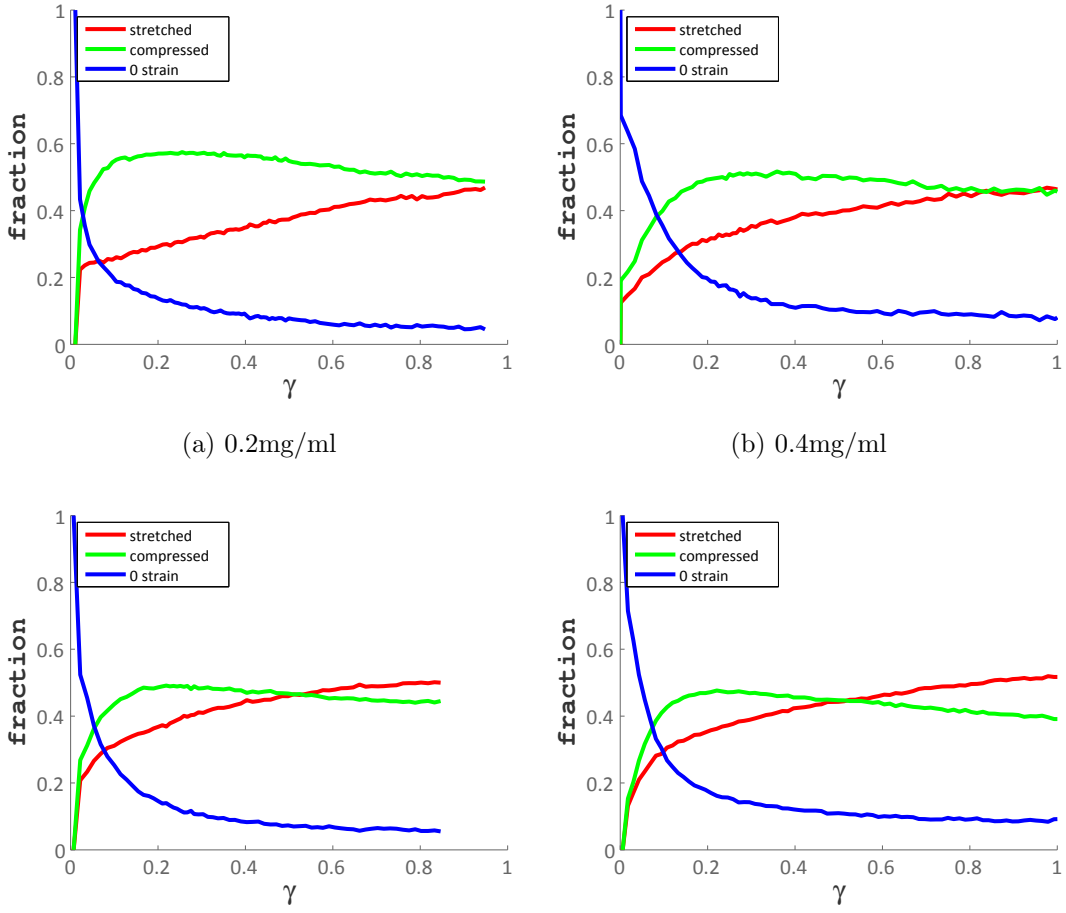

(a) 0.2mg/ml

(b) 0.4mg/ml

(c) 0.8mg/ml

(d) 1.6mg/ml

Figure 9.5: The fraction of fibers that are stretched or compressed using ϵ as the definition for many different concentrations.

9.2.1 A note on the role of noise in the strain measurements

The accuracy of the strain measurement depends on the accuracy of the location and tracking of the two end points of a fiber. This has some degree of noise associated with it. When we measure the distance between two end points, we measure that actual distance plus a small noise term, δ_{noise}. We assume this noise is random and

therefore Gaussian. However, because of this noise, the distributions of strains we show here represent the actual distribution of strains convolved with the distribution from the noise in the measurement.

$$\epsilon_{noisy} = \frac{\delta l + \delta_{noise}}{l} = \epsilon + \frac{\delta_{noise}}{l}.$$

In general, this is why it is more accurate to use average information such as the mean fiber strain (below).

9.3 Mean individual fiber strain

We determine the mean strain of the stretched fibers, the compressed fibers, and the entire population of fibers. We find that the mean positive strain becomes larger and the mean compressed strain becomes more negative with increasing system strain (see fig. 9.6). The mean positive strain grows faster than the mean negative strain decreases.

This measurement may still have problems associated with the noise (as outlined above). These problems can be avoided if we examine the total mean fiber strain, $< \epsilon >$, as a function of system strain, γ. This turns out to be a very interesting measure that is helpful in understanding how strain is being propagated into the network.

We determine the mean individual fiber strain for four different network concentrations as a function of system strain, γ (see fig. 9.7). For each of these datasets, the mean strain is negative at low strains but will eventually become positive at higher strains. This distribution is in stark contrast to what we would expect for an affinely

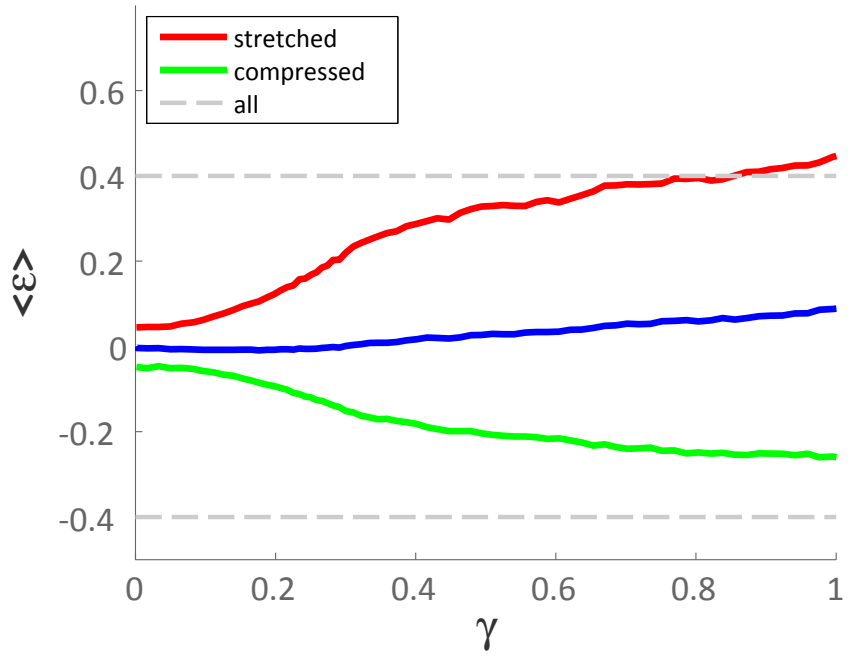

Figure 9.6: The mean individual fiber strain $< \epsilon >$ for just the stretched, compressed and total mean strain.

deforming network. In that case, we find a steadily increasing $< \epsilon >$ that is never below 0 (see fig. 9.8). The point at which the actual mean strain crosses 0 is correlated to the onset of strain-stiffening in these networks as we describe in section 9.3.2 of this chapter.

9.3.1 Some notes on the actual calculation of the mean strain

Since the motion of the end points still has a small amount of associated noise, we can look at the mean strain that a fiber undergoes in a small window of system strain that corresponds to several smaller strain steps. This is useful for cleaning up measurement noise. This has the drawback that with an increased strain window,

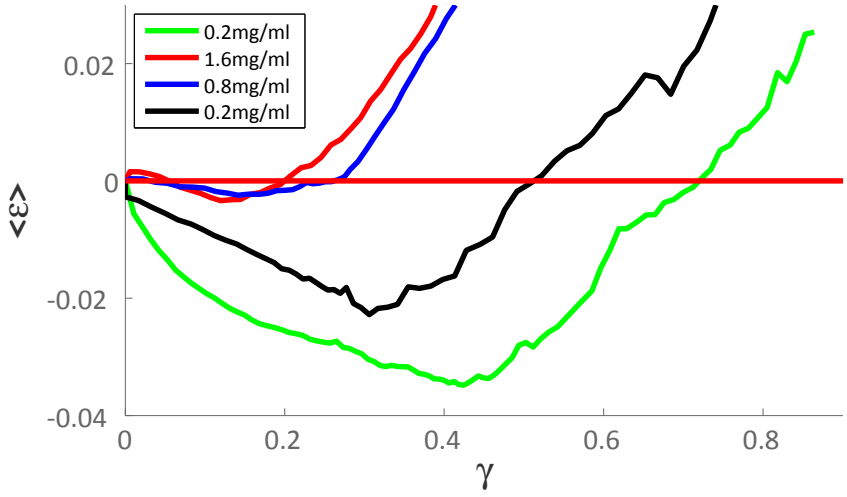

Figure 9.7: The mean individual fiber strain for 4 concentrations. The trend in the crossing through 0 corresponds well with the trend in the onset of strain-stiffening for the different samples.

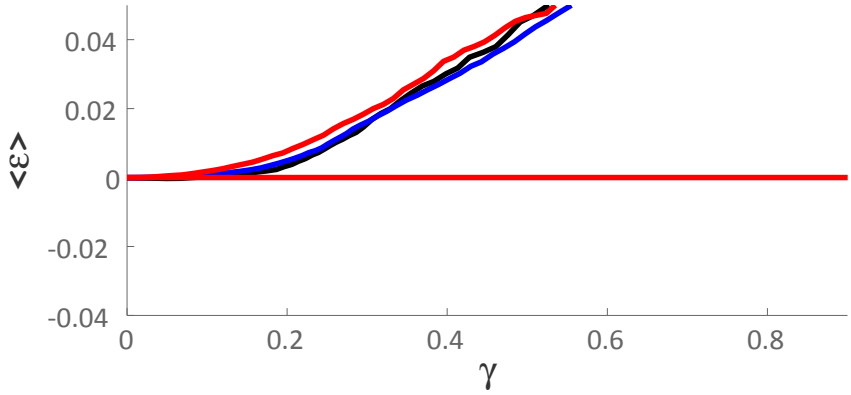

Figure 9.8: The mean individual fiber strain for several datasets assuming the networks had deformed affinely.

the mean strain crosses 0 at earlier strains. This makes sense if we assume that the fibers are actually compressed at small strains but become stretched at higher strains (see fig. 9.9).

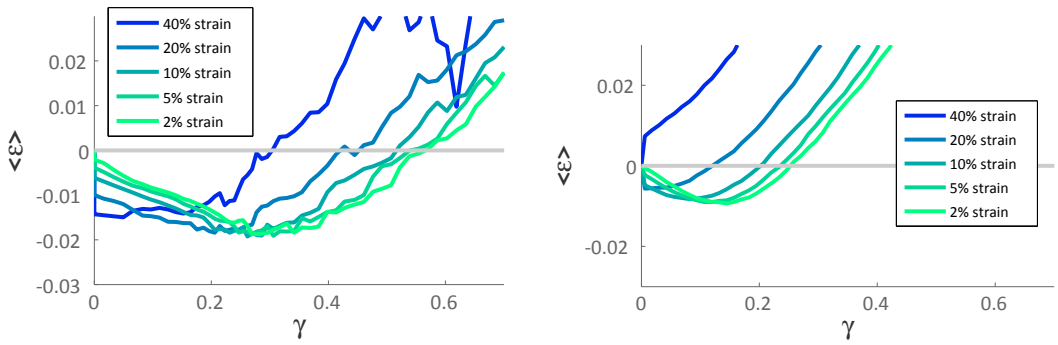

(a) 0.4mg/ml

(b) 1.6mg/ml

Figure 9.9: Mean strain averaged over different strain windows.

9.3.2 Relation of mean individual fiber strain to network mechanics

If we compare the mean strain, $< \epsilon >$, to the mechanical responses of these networks, we can identify some interesting trends. We find that the crossing of $< \epsilon >$ through 0 follows a similar trend as the onset of strain-stiffening for the four different concentrations: The higher concentration samples strain stiffen at smaller strains as well as have a $< \epsilon >$ that crosses 0 at smaller strains (fig. 9.7). Moreover, if we look in detail at what this involves, we find that the initial compressive strain in the network corresponds to the linear regime in these networks (see fig. 9.10).

9.4 Strain distribution at a given fiber orientation

We can start to understand why the fibers are compressed in the linear regime by examining the average amount individual fibers are stretched at various orientations in the network. We use the same definition of θ from chapter 8. (Basically, if we

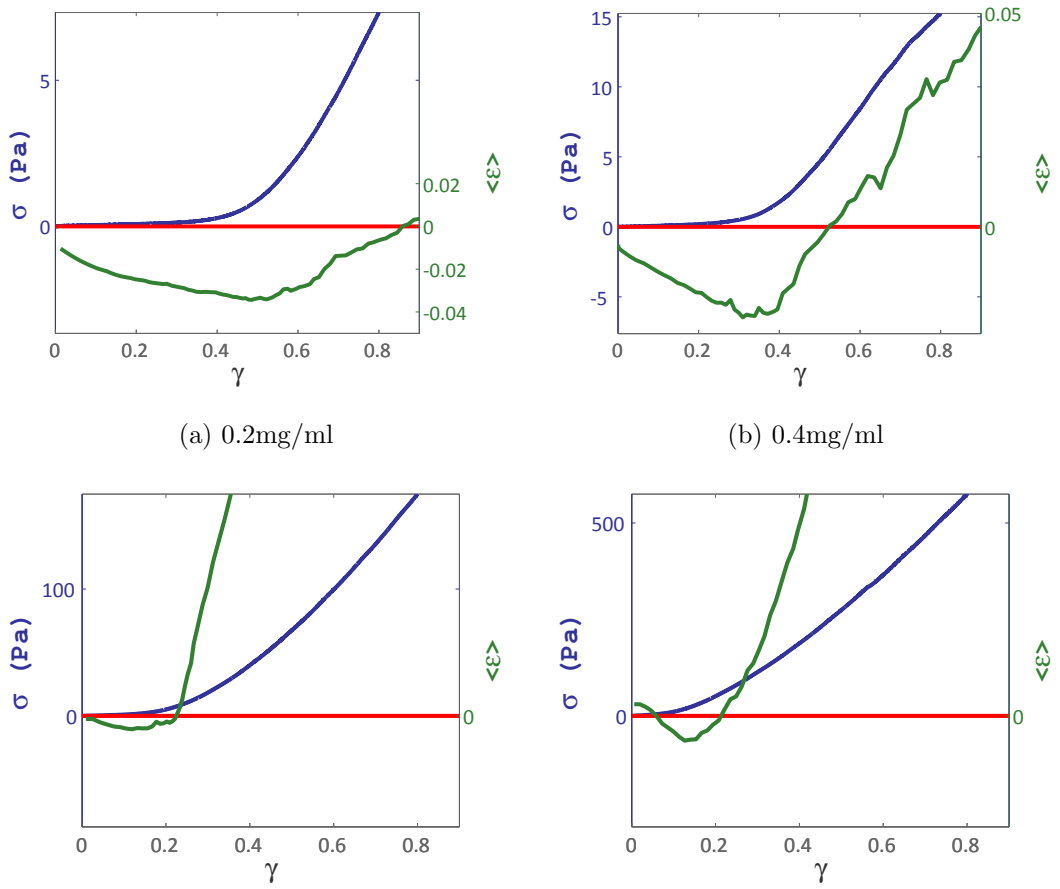

(a) 0.2mg/ml

(b) 0.4mg/ml

(c) 0.8mg/ml

(d) 1.6mg/ml

Figure 9.10: The fraction of fibers that are stretched or compressed using ϵ as the definition for many different concentrations.

shear in the $(-)y$ direction, θ is the angle away from the y axis.) We segregate fibers by their angle in the $y-z$ plane. We calculate the average mean strain for all fibers in a small range of θ, repeating this for every θ.

We compare the mean strain we measure to the expectation from a network that deformed affinely. We find that at small strains, the measured mean strain is around 0 for fibers that are expected to become stretched (approximately $\pi/2 < \theta < \pi$).

This is significantly less than the affine expected mean strain. By contrast, the mean strain of fibers perpendicular to this direction, exhibit negative strain values similar to that of the affine expectation (see fig. 9.11). As the overall network is deformed further, the mean strain becomes more pronounced at values of θ, where the fibers are expected to become stretched but remains near or below the affine expected value, while the fibers expected to become compressed continue to more closely follow the affine expectation (fig. 9.12).

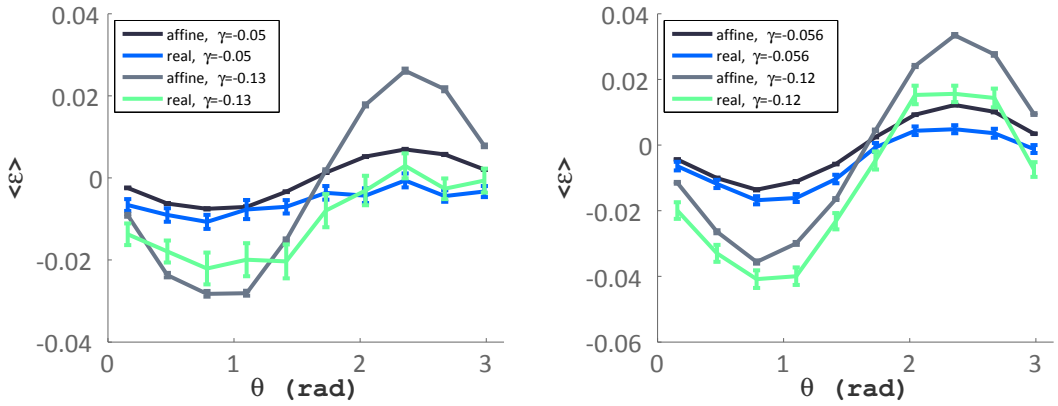

(a) 0.4mg/ml

(b) 1.6mg/ml

Figure 9.11: The mean individual fiber strain for fibers at different values of θ in the network with small network strain

9.5 Conclusion

As a fibrin network is sheared, we find that, on average, the mean fiber strain is compressive at small deformations (low system strains), while at large deformations (high system strains) fibers, on average, begin to become stretched. This is in contrast

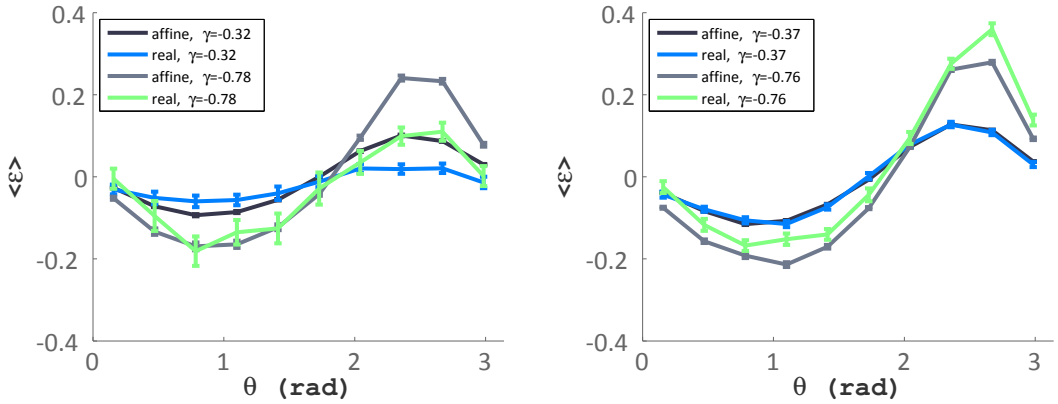

(a) 0.4mg/ml (b) 1.6mg/ml

Figure 9.12: The mean individual fiber strain for fibers at different values of θ in the network with large network strain

to the affine expected strain which should steadily increase from 0. To understand why the average fiber strain is initially compressive, we segregate the fibers by their orientation in the network and calculate the mean strain for each angle. We find that the mean strain of compressed fibers corresponds well to the affine expectation; however, the mean strain of fibers that are expected to be stretched show a mean strain around 0. This indicates that the fibers in the direction of strain are not stretched explaining the mean strain which is initially compressive. To understand these data in the context of other data in this thesis the chapter 11 on the mechanism.

Note: these mean strain calculations were done using the definition of strain that assumes the initial end-to-end distance between a fiber's branch points represents its initial length, ϵ. This is always an overestimation of the strain which accounts for the initial arc length of the fiber, ϵ_{arc}. Since most of our conclusions rely on fibers being initially compressed, the general arguments should still hold (since the strain defined

in this manner should be even more compressive).

Chapter 10

Stress estimation

The stress required to deform a network arises from the stress required to strain all of the individual fibers and the branch points that comprise the network. Since we have measured the strains of all of the fibers in the network, it may, therefore, be possible to estimate the total shear stress required to deform the network.

When we move the top plate during a shear experiment, the network below exerts a total force, $\overline{F}$, on the top plate. We can break this force up into two components: the component parallel to the motion of the top plate and a component perpendicular. These correspond to the shear force, $\overline{F_s}$, and normal force, $\overline{F_N}$, respectively (see fig. 10.1). The stress, σ, is the force, F, scaled by the plate area, A. The shear stress, σ_s, and normal stress, σ_N, are the shear and normal forces scaled by area, respectively.

In the first part of this chapter, we are concerned with estimating the shear stress. We will subsequently use a similar methodology to estimate the normal force. Since this has previously never been directly measured, I will also go through a detailed explanation of different approaches and, in particular, how many of these fail owing

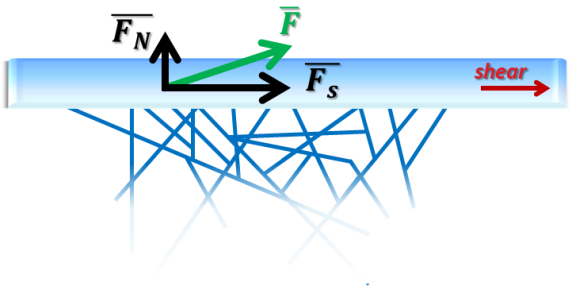

Figure 10.1: An illustration of the force from a network being sheared. The total force can be divided into the shear force that lies parallel to the top plate while the normal force lies perpendicular to it.

to noise in the branch point tracking.

10.1 Set-up of shear stress estimation

The total force felt on the top plate is just the force from the fibers directly connected to the top plate.

$$\overline{F} = \sum_i \overline{f_i}$$

where $\overline{f_i}$ is the force from one fiber and the sum is over all of the fibers connected to the top plate. The shear stress, σ_s, is the magnitude of the force in the direction of shear scaled by the plate area. We can replace the sum over the force from all fibers with the sum over just the shear component of all individual forces.

$$\sigma_s = [\frac{1}{A}\sum_i \overline{f_i}] \cdot \hat{s} = \frac{1}{A}\sum_i \overline{f_i} \cdot \hat{s} = \frac{1}{A}\sum_i f_{i_s} \tag{10.1}$$

where $\hat{s}$ is the direction of shear, the sum is again over the fibers connected to the top plate and f_{i_s} is the magnitude of the force for the fiber, i, in the direction of shear. Moreover, we can find the shear stress in terms of the density of fibers on

the top plate, α, and the average force from the fibers connected to the top plate, $< f_s >_{topplate}$,

$$\sigma_s = \frac{1}{A}\sum_i f_{i_s} = \frac{N_{topplate}}{A} < f_s >_{topplate} = \alpha < f_s >_{topplate} \tag{10.2}$$

using,

$$< f_s >_{topplate} = \frac{1}{N_{topplate}}\sum_i f_{i_s} \tag{10.3}$$

and

$$\alpha = \frac{N_{topplate}}{A} \tag{10.4}$$

where all sums are over the fibers connected to the top plate and $N_{topplate}$ is the total number of fibers connected to the top plate. The formulation in equation 10.2 turns out to be more useful when we extend the sum from only the fibers connected to the top plate to all of the fibers in the system as described in the next section.

10.1.1 Extending the sum over fibers connected to the top plate to all fibers

The imaging volume is very small in comparison to the total sample volume. The plate area in the field of view is, at most, $250\mu m^2$ compared to the actual plate area of $\sim 1cm^2$. This does not particularly matter for our shear stress calculation, because we can always use the total force from the fibers in our field of view that are connected to the top plate and scale by the area of the plate we image; however, this *does* have the limitation that we only have the few fibers connected to the top plate to calculate the total shear stress. This can lead to noisy results. However, we can achieve better statistics by noting the following. If we take an arbitrary plane through the network

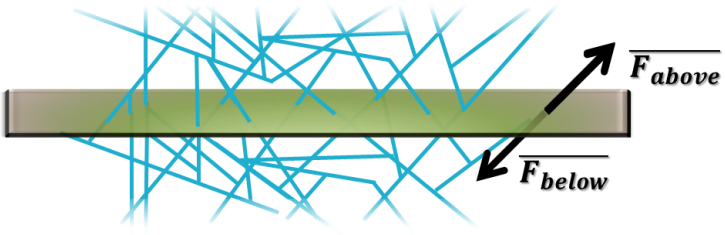

Figure 10.2: Force balance on an arbitrary plane through the network

parallel to the top and bottom plates, the force on this plane from the fibers above and below must balance (fig. 10.2) Since they balance, the force from either the top or bottom of the plane must be equal to the force on the top and bottom plates (the magnitudes are equal - so the force vector will have a sign difference depending on whether it is the force from below or from above). A different way of thinking of this is that each 'sub-volume'enclosed by a plane above and below it acts like a spring; from the top plate to the bottom plate, there are basically many springs in series. Consequently, the force on the bottom is equal to the force on the top, and the same holds for every plane in-between. For a more formal treatment, you can see (Doi and Edwards, 1988) pg. 70.

Assuming the density of fibers is approximately constant throughout the network, the average force for each arbitrary plane through the network must also be the same. We therefore extend the sum over just the fibers on the top plate to all of the fibers in the system. We therefore can rewrite equation 10.2 as:

$$\sigma_s = \alpha < f_s > \tag{10.5}$$

where $< f_s >$ is the average over *all* the fibers in the system.

10.1.2 Approximating the density of fibers on the top plate

We want to find the density, α, of fibers on the top plate. The density of fibers on the top plate should be proportional to the characteristic mesh size of the network, ξ:

$$\alpha = \frac{1}{\xi^2}$$

We want to find the α value in terms of the node density, n. This is the total number of nodes in the system, N_{nodes}, scaled by the volume, V,

$$n = N_{nodes}/V$$

This is an easy quantity for us to measure directly from our images (Alternatively,

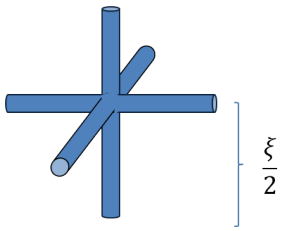

Figure 10.3: A typical node in a typical unit cell.

we could have used the line density, another quantity that is easy to measure). We can relate these two quantities by considering a typical unit cell. There is one node in a typical unit cell and the volume of the unit cell is proportional to ξ^3 (fig. 10.3). The node density for a typical unit cell will then be,

$$n = \frac{1}{\xi^3}$$

Therefore, we can rewrite α in terms of the node density:

$$\alpha = n^{2/3} \tag{10.6}$$

10.2 Force extension relation of an individual fiber

In our confocal experiment, we measure the displacements of the branch points and, from these, the strain on the individual fibers (see chapter 9). However, we need to know the force that these fibers exert to calculate the total shear stress on the top plate from equation 10.5[1].

Recent studies have measured the force-extension curve of individual fibrin fibers using atomic force microscopy (Hudson et al., 2010; Liu et al., 2010). These studies have found that the individual fibers are linear up to strains of 1 with a Young's modulus of $10MPa$. The low-strain Young's modulus was also measured using optical tweezers and found to be about $14MPa$(Collet et al., 2005).

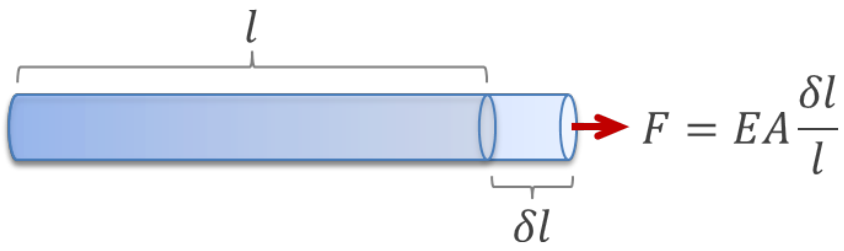

Figure 10.4: The force from a linearly elastic beam in extension

From these measurements, we assume the fibers are linear in extension. We also assume the fibers behave like linearly elastic beams. This is most likely an over-simplification, but it is a good first approximation. In this case, the force, F, required to stretch a fiber is (see also figure 10.4),

[1]Many of the equations in this section can be found in a standard text on mechanics. See, for example, (Timoshenko and Gere, 2009) for more information

$$F_s = EA\frac{\delta l}{l} \tag{10.7}$$

where,

δl the total amount the fiber is stretched

l the length of the fiber

A the cross-section area of the fiber

E Young's modulus of the fiber.

To understand the role of fiber bending and buckling, we compare the force required to stretch the fiber a small amount, δl, to the force required to bend a fiber the same amount. For this calculation, I will assume the fiber behaves like an Euler-Bernoulli beam.

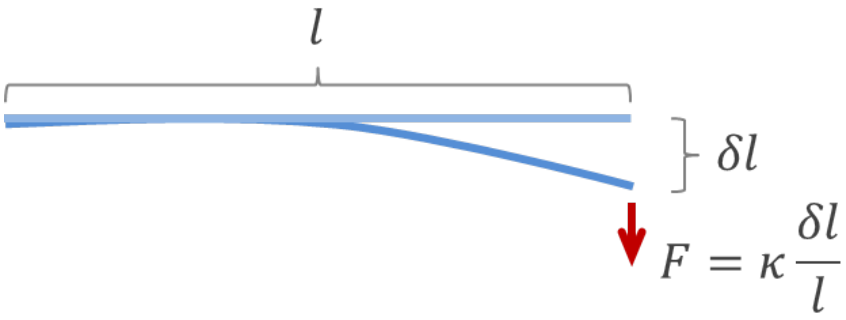

Figure 10.5: The force from an Euler beam of length l being bent a deflection of δl

The force required to bend a beam clamped at one end is given by (fig. 10.5) :

$$F_B = \kappa\frac{\delta l}{l^3} = EI\frac{\delta l}{l^3} \tag{10.8}$$

where,

κ the bending stiffness

δl the amount the fiber is deflected

l length of the fiber

E Young's modulus of the fiber

I area moment of inertia the fiber

For a uniform beam of circular cross-section, the area moment of inertia is $I = \frac{\pi}{4}r^4$. We can compare the force required to stretch the fiber versus the force required to bend the fiber,

$$\frac{F_B}{F_s} = (\frac{r}{l})^2 \tag{10.9}$$

Typical values of the length and radius of the fibers is $5\mu m$ and $0.1\mu m$, respectively. In this case, the force for bending would be $4 \cdot 10^{-4}$ that of stretching a fiber an equivalent amount. For instance, the actual force for deflecting a fiber $0.5\mu m$ that is $5\mu m$ long with a Young's modulus of $14MPa$ and a radius of $100nm$ is $0.004nN$ compared to $44nN$ for stretching the fiber an equivalent amount. We therefore consider any transverse bending negligible for the estimation of the total shear stress on the network.

To understand how these fibers behave in compression, we recall that the fibers are long and slender. We therefore expect them to buckle. To determine the force required to buckle the fiber, we calculate the critical force, F_c, required to buckle the fiber using Euler buckling.

$$F_c = \frac{\pi^2 EI}{l^2} \tag{10.10}$$

For a fiber with the typical dimensions we used for the bending and stretching forces above, we find that the force required to buckle the fiber is $0.1nN$. (Note: the fibers are rarely perfectly straight and usually have a small but gentle bend. This bend will also lower the force required to compress the fiber.) We therefore consider the amount of force required to buckle the fiber to be small and set all compressive forces on the fiber to zero in our estimation of the shear stress (below).

Finally, the force extension curve that we use for estimations of the shear stress assumes the fiber is linear in extension with a Young's Modulus of $14MPa$, 0 in compression and all transverse motions are also negligible (see fig. 10.6 for a representative force extension curve).

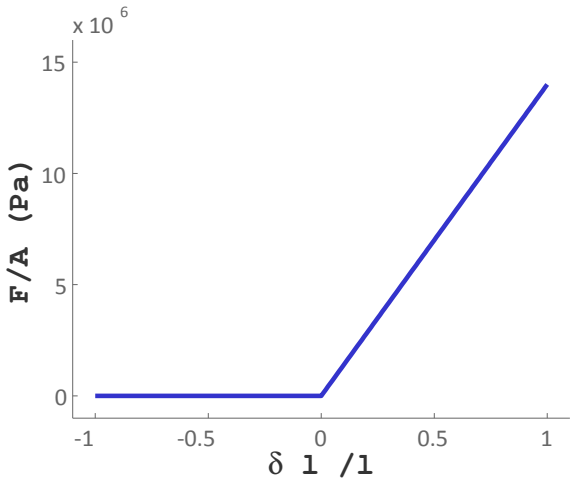

Figure 10.6: The force extension curve we assume for an individual fiber.

$$F_{ind} = \begin{cases} EA\epsilon & \text{if } \epsilon > 0 \\ 0 & \text{if } \epsilon <= 0 \end{cases} \tag{10.11}$$

where I have used $\epsilon = \frac{\delta l}{l}$ for the individual fiber strain.[2]

[2]When we try to calculate this quantity using real data-sets, this definition of the force

10.3 Shear stress estimation: the most straightforward approach

For each fiber, we calculate the total force that the fiber exerts on the top plate and, subsequently, we average all of the components of all of the forces in the direction of the shear strain. Basically, we directly calculate what we would expect given our distribution of fiber strains, using the equation for the total shear stress, eq. 10.5, and the force extension curve given in eq. 10.11. Explicitly the equation becomes,

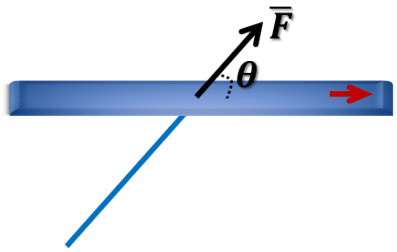

Figure 10.7: The angle θ from a fiber is defined as the angle between the force from the fiber and the primary direction of shear

$$\sigma_{std} = \alpha < f_s >= \alpha < EA\epsilon_i cos\theta_i >_+, \tag{10.12}$$

where θ_i is the angle of each fiber, i, away from the primary shear direction (fig. 10.7)[3] ($-y$ for most of the experiments). Here, we have introduced the new notation,

from an individual fiber tends to create problems. The reason for this is that positive noise in the measurement does not cancel the negative noise for fiber strains around 0. This is discussed in detail in section 10.3.1. In many cases in the rest of the chapter, to investigate how compressed elements can or cannot cancel the stretched elements, we recalculate quantities pretending, for the sake of that calculation, that the individual fiber force in compression is equal and opposite to the force from stretching.

[3]The definition of θ is the same as the one we used in our discussion of fiber orientations in chapter 8

$< .. >_+$, to indicate an average over all fiber strains, except that fiber strains that are negative contribute to the average with 0 strain. We assume the Young's modulus and areas are constants and pull them out of the sum:

$$\sigma_{std} = \alpha EA < \epsilon cos\theta >_+, \tag{10.13}$$

where,

$$< \epsilon cos\theta >_+ = \sum \epsilon_i cos\theta_i \quad \text{with } \epsilon < 0 \text{ contributing 0 to the product} \tag{10.14}$$

For the final calculation of this quantity, we assume that $E = 14MPa$ (taken from literature (Collet et al., 2005)). We use the fiber cross-sectional area, A, as a fit parameter. This value scales the resultant stress curve by a constant. For convenience, in most of this chapter, we set this value so that the maximum stress reached for our estimate matches the stress we actually measure in the rheometer. At the end of the chapter, when I have presented the final procedure that we use to estimate the shear stress, I compare the radii we use for the fiber area to reported literature values.

Moreover, we compare these results to the shear stress expected for a network that had deformed affinely. We use the initial positions of the fibers in the unsheared network stack to calculate their positions at each shear point in our experiment. We repeat our shear stress calculation on the affinely deformed network keeping all the parameters except the fiber area A constant. We leave A as a fit parameter as described above.

We estimate the shear stress using the real fiber positions for four different concentration samples as well as the affinely deformed positions (figure 10.8 and 10.9 light blue curves and red curves, respectively). For all of the samples, the affine predictions (red curves), exhibit a linearly increasing stress response that overestimates

the actual shear stress response (dark blue curve)(see fig. 10.8 and 10.9). For the high concentration, 1.6mg/ml sample, the shear stress estimation using the real deformation is similar to the actual shear stress response (fig. 10.9 b) . However, the shear stress estimation for the lower concentration, 0.4mg/ml sample, overestimates the actual shear stress (fig. 10.8 b). We can understand this overestimation of the

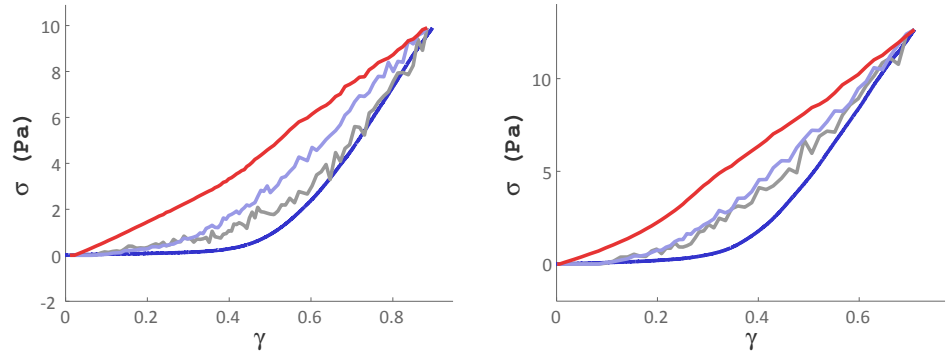

(a) 0.2 mg/ml sample

(b) 0.4 mg/ml sample

Figure 10.8: Comparison of the actual shear stress (dark blue line) to the most straightforward estimation of the shear stress (light blue line) for 0.2 mg/ml and 0.4 mg/ml samples. The same calculation is repeated on a network that had deformed affinely (red line). The calculation is repeated again using the actual network deformation but modifying the force extension relation of an individual fiber so that the fiber does not buckle, but rather, compresses (light gray line).

force required to deform the network by considering the noise in our measurements.

10.3.1 The effect of noise in our measurements

When we deform a fibrin network, a portion of the fibers is compressed, a portion is stretched, and the remaining portion is neither stretched nor compressed. For our

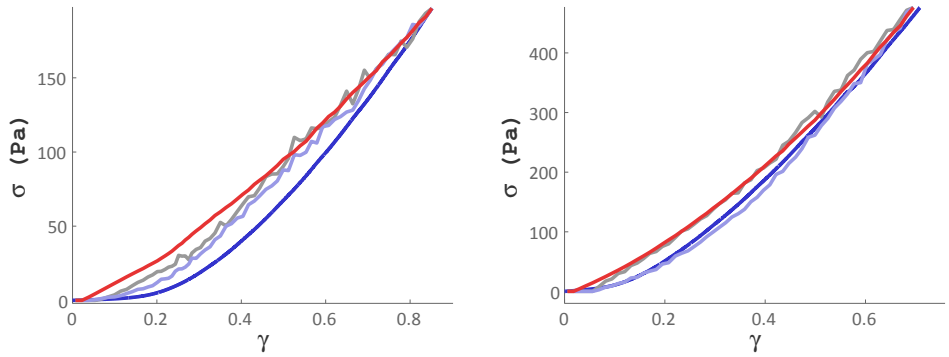

(a) 0.8 mg/ml sample

(b) 1.6 mg/ml sample

Figure 10.9: Comparison of the actual shear stress (dark blue line) to the most straightforward estimation of the shear stress (light blue line) for 0.8 mg/ml and 1.6 mg/ml samples. The same calculation is repeated on a network that had deformed affinely (red line). The calculation is repeated again using the actual network deformation but modifying the force extension relation of an individual fiber so that the fiber does not buckle, but rather, compresses (light gray line).

calculation of the shear stress, we assume that all compressed fibers exert 0 force. This is a good approximation for the fibers that are actually compressed. However, we run into a problem with the fibers that have a strain close to 0. When we measure the strain of an individual fiber we do not actually measure the strain; rather, we measure this quantity plus a small degree of (presumably random) noise. In general, when we take the average force a fiber exerts, $< f >$, the positive and negative noise contributions should cancel, and we should get something close to the actual average force. The problem is, we set all negative contributions to the force to 0. Therefore, for fibers that have strains close to 0, the positive and negative noise contributions do not cancel, leading to the overestimation of the force that we find in figures 10.8

and 10.9.

Note: When we consider the mechanism that we think underlies the strain-stiffening response in these networks, we expect a significant portion of the fibers can *avoid* being stretched when the network is deformed. Assuming this is indeed the case, the number of fibers that have strains at or near 0 is very large! (See the discussion of the underlying mechanism in chapter 11 and the direct measurement of fiber strains in chapter 9.)

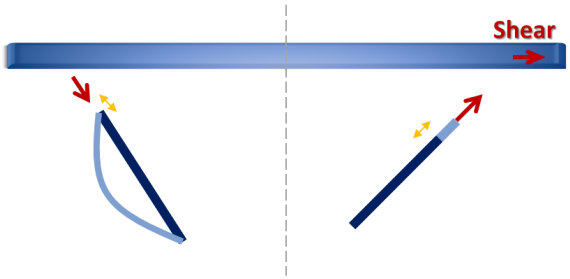

Figure 10.10: On average, the population of fibers that are compressed have an orientation that is perpendicular to the principal axis of strain, while the fibers that become stretched lie along the principle axis of strain. Moreover, it may be the case that in our experiments there is a delay before fibers in the stretched direction actually become stretched. They therefore have 0 strain initially.

Moreover, we may (incorrectly) think that errors in our measurement might still cancel: since the fibers are distributed isotropically, there will be as many fibers pointing in one direction with an erroneous positive shear strain contributing an erroneous positive force to the shear stress, as there are fibers in the other direction contributing an erroneous negative force to the shear stress. This is not the case because, on average, the amount a fiber is stretched depends on its orientation in the network. Fibers perpendicular to the primary direction of strain (roughly fibers with

$\frac{\pi}{2} < \theta < \pi$) will be compressed while fibers along it (roughly fibers with $0 < \theta < \frac{\pi}{2}$) will have very little or no strain (see fig. 10.10, see also the distribution of strains as a function of angle fig. 9.11 and the discussion of the underlying mechanism in chapter 11). Consequently, the fibers with strains around 0, where noise problems arise, tend to be oriented primarily in the direction of stress and, therefore, contribute positively to the shear stress (fig. 10.8 and fig. 10.9).

Consistent with this, if we assume for a moment that compressive elements do not buckle and instead compress, we would have gotten an even smaller shear stress approximation (fig. 10.8 and 10.9 gray line). (Some of the compressed elements would cancel the positive elements. However, this approximation still overestimates the actual shear stress because the compressed fibers, on average, add to the total shear stress when, in reality, the force required to buckle them should, in fact, be negligible.)

10.4 Shear stress estimation: average first and then sum (a seemingly correct but not correct way to average)

One enticing (yet wrong) way to avoid this problem is by replacing the average of the two products with the product of the averages in eq. 10.13 : $< \epsilon cos\theta >_{+} = < \epsilon >< cos\theta >$ where $< \epsilon >$ is the average of ϵ (including compressive elements). In that way, positive and negative noise contributions should cancel, and the resulting average strain, $< \epsilon >$, should represent the average of the real strain without noise.

After calculating this average, if the resulting average strain is 0, we assume that most of the fibers are compressed and set the resulting shear stress to 0. The equation for the shear stress would then become:

$$\sigma_{wrng} = \begin{cases} EA\alpha < \epsilon >< cos\theta > & \text{if } < \epsilon >> 0 \\ 0 & \text{if } < \epsilon >\leq 0 \end{cases} \tag{10.15}$$

This way of averaging (had it been correct) assumes that the average strain, $< \epsilon >$, must be roughly equivalent to the average strain of just the positive elements $< \epsilon >_+$.

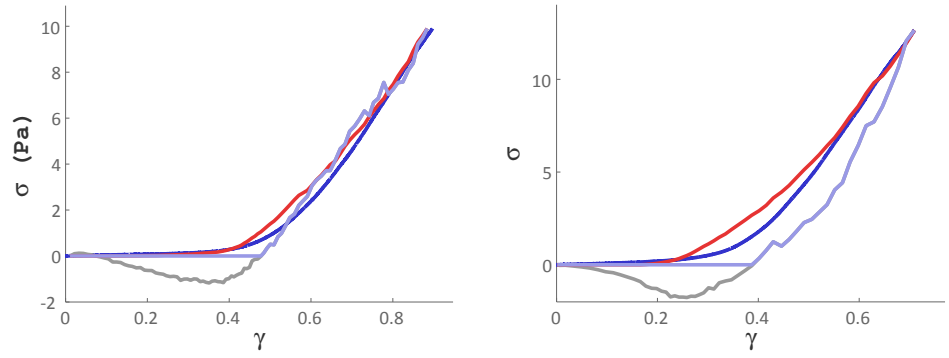

(a) 0.2 mg/ml sample

(b) 0.4 mg/ml sample

Figure 10.11: Comparison of the actual shear stress (dark blue line) to an estimation of the shear stress for 0.2 mg/ml and 0.4 mg/ml samples (light blue line) averaged using equation 10.15. For comparison, had we assumed the force to compress a fiber was equal and opposite to the force required to stretch a fiber, we would get the estimation in gray.

When we repeat this on the four data-sets that we evaluated before, we find that the estimated shear stress (fig. 10.11 and 10.12 light blue curve) is 0 initially and always underestimates the actual shear stress (fig. 10.11 and 10.12 dark blue curve).

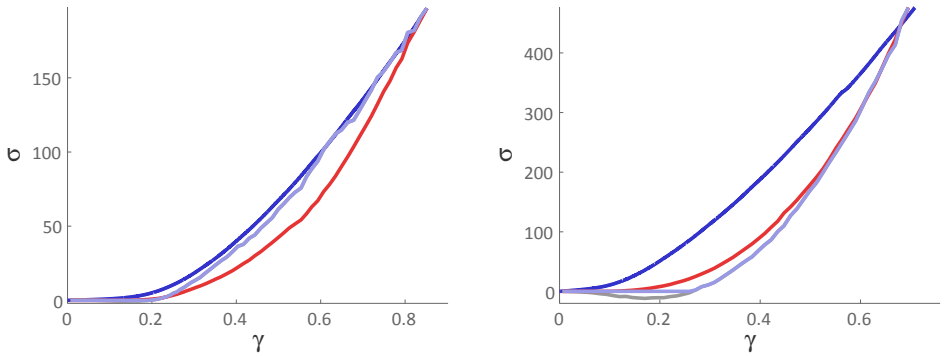

(a) 0.8 mg/ml sample

(b) 1.6 mg/ml sample

Figure 10.12: Comparison of the actual shear stress (dark blue line) to an estimation of the shear stress for 0.8 mg/ml and 1.6 mg/ml samples (light blue line) averaged using equation 10.15. For comparison, had we assumed the force to compress a fiber was equal and opposite to the force required to stretch a fiber, we would get the estimation in gray.

We can begin to see the problem with this method if we allow the fibers to bear compressive load and estimate the shear stress with:

$$\sigma_{wrngComp} = \quad EA\alpha < \epsilon >< cos\theta > \quad \text{for all cases}$$

including contributions from compressed elements. The approximated shear stress measured like this is strongly negative at low strains (fig. 10.11 and 10.12 gray curve). We know, on average, most of the fibers are compressed at these strains. In addition, those fibers are oriented roughly perpendicular to the principal direction of strain (roughly speaking, these fibers will have $\frac{\pi}{2} < \theta < \pi$). These fibers should contribute *positively* to the total shear stress (basically, they would push back against the plate that is being sheared), yet, here they appear to be contributing negatively. The reason for this is that although $< \epsilon >$ is negative, the average orientation of

the fibers is between 0 and $\frac{\pi}{2}$. This leads to $< cos\theta >$ being positive. The product, $< \epsilon >< cos\theta >$, is therefore negative (contrary to what it should be).

10.4.1 Individual fiber strain and orientation are correlated

The reason the shear stress estimation in eq. 10.15 does not hold stems from the fact that the strain a fiber is exposed to is correlated with its direction in the network. We saw this was the case in chapter 9. Generally speaking, the average of a product, $< AB >$, is only equal to the product of its averages, $< A >< B >$, when these are not correlated. This can easily be seen by using the definition of an average,

$$< AB >= \frac{1}{N}\sum_{i=1}^{N} A_i B_i$$

Now, we can always re-write A_i in terms of its deviation from the average, $A_i =< A > +\delta A_i$ where δA_i is the deviation. Doing a similar treatment of B_i, we can expand the product in the sum:

$$\begin{aligned} < AB > &= \frac{1}{N}\sum_{i=1}^{N}(< A > +\delta A_i)(< B > +\delta B_i) \\ &= \frac{1}{N}[(N < A >< B > +\sum_{i=1}^{N}(< A > \delta B_i + < B > \delta A_i + \delta A_i \delta B_i) \\ &= < A >< B > +\sum_{i=1}^{N}\delta A_i \delta B_i \end{aligned}$$

When the variations in A and B are uncorrelated, the product of $\delta A_i \delta B_i$ will go to zero, on average, when we sum over all contributions (for a large number of elements). However, in the event they are correlated, this may not be the case (If δA_i is more likely to be positive (or negative for that matter) when δB_i is positive, then the sum of the product will be non-zero.)

For the shear stress approximation we can not, therefore, replace the product $< \epsilon cos\theta >$ with $< \epsilon >< cos\theta >$.

10.5 Shear stress estimation: Bin fibers by orientation, average and find shear stress

We would like to have a method to calculate the shear stress that will overcome the overestimation that occurs from noise. We can not average over all of the strains first, as discussed above, to find the average force. However, we can, instead, utilize the fact that strain and fiber orientation are correlated. Our original equation for the shear stress is:

$$\sigma = \alpha < f_s >_+ = \alpha EA < \epsilon_i cos\theta_i >_+$$

Instead of averaging over all of the fibers to find the average fiber force, we divide all possible orientation of fiber angles, θ, into n_{bin} bins, $\theta_{1,2,3...n_{bin}}$ (see fig. 10.13). We segregate all of the fibers based on their orientation and respective binned angle. Then we can re-write the equation for the shear stress, equivalently, as:

$$\sigma_{ang} = \alpha EA < \epsilon_i cos\theta_i >_+ = \alpha EA \sum_{s=1}^{n_{bin}} \phi_{\theta_s} < \epsilon cos\theta_s >_{+,\theta_s}$$

where the sum ranges over the all of the binned angles and ϕ_{θ_s}, is the fraction of fibers at each binned angle. Here, we have introduced the notation, $< .. >_{+,\theta_s}$, to denote the average over just the fibers that have the binned angle, θ_s, and all negative strains contribute to the average with 0 strain. If we note that for each s, θ_s is constant, this

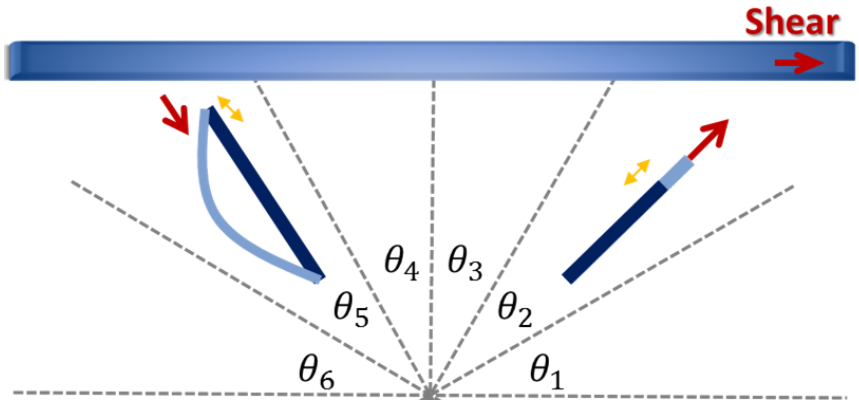

Figure 10.13: Graphic illustrating the segregation of fiber angles with respect to the top plate.

equation becomes:

$$\sigma_{ang} = \alpha EA \sum_{s=1}^{n_{bin}} \phi_{\theta_s} < \epsilon >_{+,\theta_s} cos\theta_s$$

To this point, writing the shear stress in this manner is completely equivalent to the most standard average, eq. 10.13. However, here we make an assumption. If this assumption is correct, then the following remains equivalent to eq. 10.13, yet we can overcome our noise limitation; if the assumption is wrong, then the following is not a correct expression. The assumption we make is that for each fixed angle, that instead of averaging over just positive ϵ at this fixed angle, we can first average over ϵ for all of the fibers at this fixed angle, including negative contributions and then, set the average to 0 if the result is negative. Basically, what this assumes is that for a given angle, all of the fibers with that angle have an approximately uniform strain. So, the final equation for the shear stress approximated in this manner becomes:

$$\sigma_{ang} = \alpha EA \sum_{s=1}^{n_{bin}} \phi_{\theta_s} < \epsilon >_{\theta_s} cos\theta_s, \tag{10.16}$$

with $< \epsilon >< 0$ contributing 0 to the product in the sum.

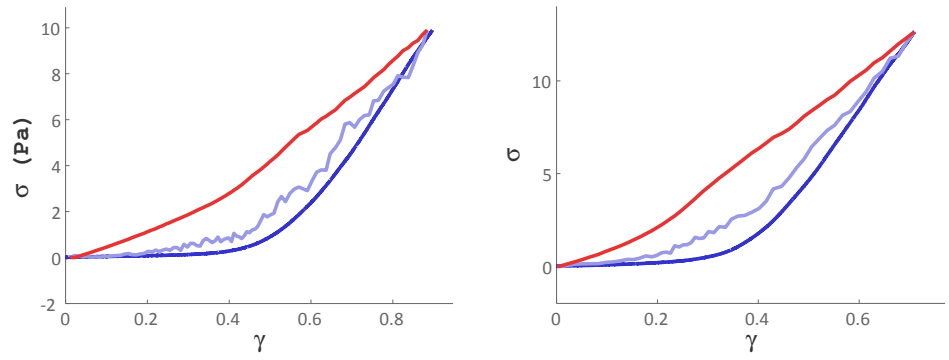

(a) 0.2 mg/ml sample

(b) 0.4 mg/ml sample

Figure 10.14: Comparison of the actual shear stress measured in a rheometer (dark blue line) to an estimation of the shear stress (light blue line) utilizing the orientation of fibers to calculate their average strain for 0.2mg/ml and 0.4mg/ml samples. This calculation is repeated for an affinely deformed network (red line).

We calculate σ_{ang} for the four different data-sets. These show the best correspondence to the actual shear stress (see fig. 10.14 and 10.15). We use an average fiber radius to fit the shear stress approximation for each data-set. The radii we find are in good correspondence with what is reported in the literature: Fibrin polymerized in buffer with 20mM $CaCl_2$ and 0.1 U/ml thrombin (as we have here), should have radii around $75 + / - 30$ (for a 3 mg/ml sample measured using SEM) (Ryan et al., 1999). The radii we find have a good correspondence with this expectation (see table 10.1).

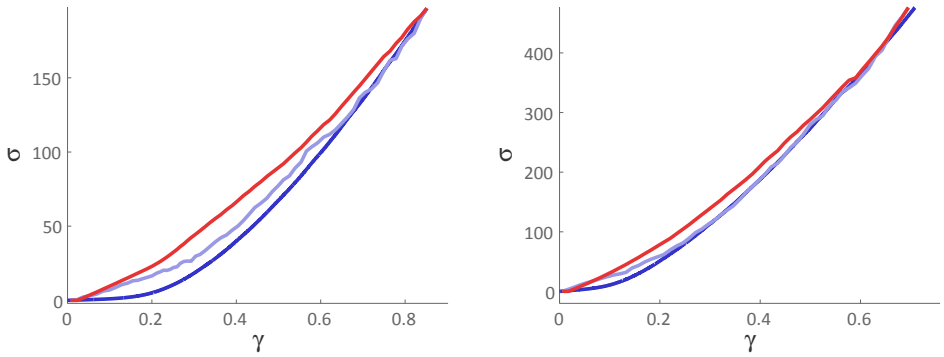

(a) 0.8 mg/ml sample

(b) 1.6 mg/ml sample

Figure 10.15: Comparison of the actual shear stress measured in a rheometer (dark blue line) to an estimation of the shear stress (light blue line) utilizing the orientation of fibers to calculate their average strain for 0.8mg/ml and 1.6mg/ml samples. This calculation is repeated for an affinely deformed network (red line).

10.6 Normal stress estimation

To estimate the normal stress exerted by the network on the top plate, we will repeat the basic approach we used to estimate the shear stress. Analogous to the shear stress, we can write the normal stress in terms of the average force from all of the individual fibers in the normal direction (z-direction in our experiment). We use coordinates so that a negative normal force corresponds to the network pulling the plates towards each other while a positive normal force corresponds to the network pushing the plates apart.

$$\sigma_n = \alpha < f_n >_+$$

Table 10.1: Expected average radii from shear stress estimation

CONCENTRATION	RADII(NM)
0.2mg/ml	29
0.4mg/ml	45
0.8mg/ml	105
1.6mg/ml	144

Again, by using the force extension curve from an individual fiber (eq. 10.11), we can re-write this equation in terms of the average strain on the top plate:

$$\sigma_n = -\alpha E A < \epsilon sin\theta >_+$$

where, again, E is the Young's Modulus (for all calculations we take this from literature to be roughly 14MPa) and A is the average area of an individual fiber (which we leave as a fit parameter). Again, the notation, $< .. >_+$, indicates an average over all strains where negative strains contribute 0 in the calculation of the average (since we have ignored the contribution from buckled fibers).

We calculate this result for three different datasets[4] and choose A so that the minimum normal stress corresponds to the normal stress we measure in the rheometer at the same strain. We find that this estimation (fig. 10.16 light blue curve) is very far from the actual normal stress.

[4]For most of the calculations in this chapter we use four data sets. However, the normal force from the lowest concentration sample is too low to measure in the rheometer

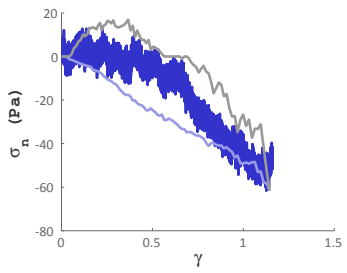

(a) 0.4 mg/ml sample

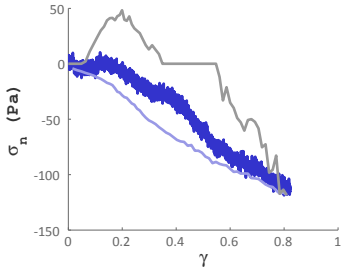

(b) 0.8 mg/ml sample

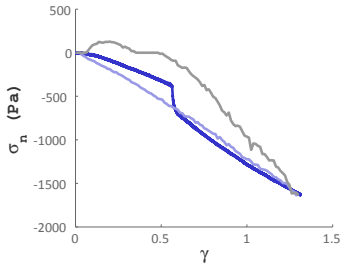

(c) 1.6 mg/ml sample

Figure 10.16: Comparison of the actual normal stress measured in a rheometer (dark blue line) to an estimation of the shear stress (light blue line) calculated in the most straight forward manner. This calculation is repeated for an affinely deformed network (red line). We also repeat this calculation assuming the fibers do not buckle but rather, compress (light gray line)

As in the shear stress measurement, we can guess that this overestimation stems largely from the noise in the measurement (see section 10.3.1 for a full discussion). To address this, we can try an approach similar to what we tried for the shear stress estimation and replace the average of the product with the product of the averages. For the shear stress measurement, this was not acceptable because the individual fiber strain, ϵ and the orientation of a fiber, θ are correlated. This is also the case with the normal stress. However, although $cos\theta$ and ϵ are correlated, I do not expect

Table 10.2: Expected average radii from normal stress estimation.

CONCENTRATION	RADII(NM)
0.4mg/ml	31
0.8mg/ml	28
1.6mg/ml	93

$sin\theta$ and ϵ to be correlated (for every $sin\theta$ you can find fibers that have a variety of strains).

$$\sigma_{avg} = \begin{cases} EA\alpha < \epsilon >< sin\theta > & \text{if } < \epsilon >> 0 \\ 0 & \text{if } < \epsilon >\leq 0 \end{cases} \tag{10.17}$$

We perform this calculation for the three data sets (fig. 10.17 light blue line) and find a much better match to the actual shear stress data (fig. 10.17 dark blue line). To find the corresponding radii for these fits, see table 10.2.[5]

[5]The normal force measured in the rheometer from the $1.6mg/ml$ sample appears a little strange compared to the other data-sets that have a curve that varies more smoothly. I have, in general, run this measurement on a large number of samples (with this and other concentrations) and think this particular sample looks a little strange. However, I have added this here for completeness, since this sample is used throughout this thesis.

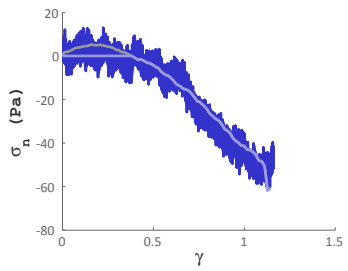

(a) 0.4 mg/ml sample

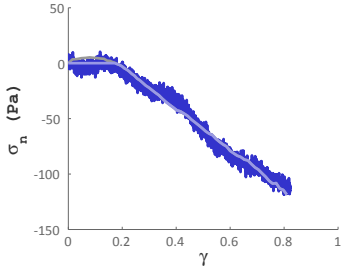

(b) 0.8 mg/ml sample

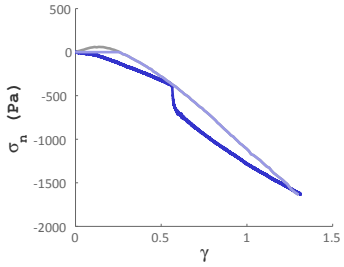

(c) 1.6 mg/ml sample

Figure 10.17: Comparison of the actual normal stress measured in a rheometer (dark blue line) to an estimation of the shear stress (light blue line) calculated using equation 10.17. This calculation is repeated for an affinely deformed network (red line). We also repeat this calculation assuming the fibers do not buckle but rather, compress (light gray line).

Chapter 11

The mechanism underlying strain-stiffening in fibrin networks

In this chapter, I include some observations from microscopy, review measurements from previous chapters and use these to motivate the underlying origin of the mechanical response of strain-stiffening in fibrin networks. I then elaborate on the implications of this mechanism and how it fits into the context of our current understanding of network mechanics. Lastly, I speculate on certain interesting limits and try to give some intuition about some of the behaviors we observe.

Briefly, what I find is that the strain-stiffening response arises when the network transitions from a linear regime, where fibers can avoid being stretched, to a nonlinear regime in which individual fibers must become stretched.

11.1 Observations from microscopy

We have a few pieces of data that can be used to understand the general behavior of the network as it is sheared and, from this hypothesize the general mechanism that underlies the strain-stiffening. However, it might be easiest to first show the most compelling piece of data (the microscopy images), explain what I think is going on and, then, explain the quantitative evidence we have to back up this picture.

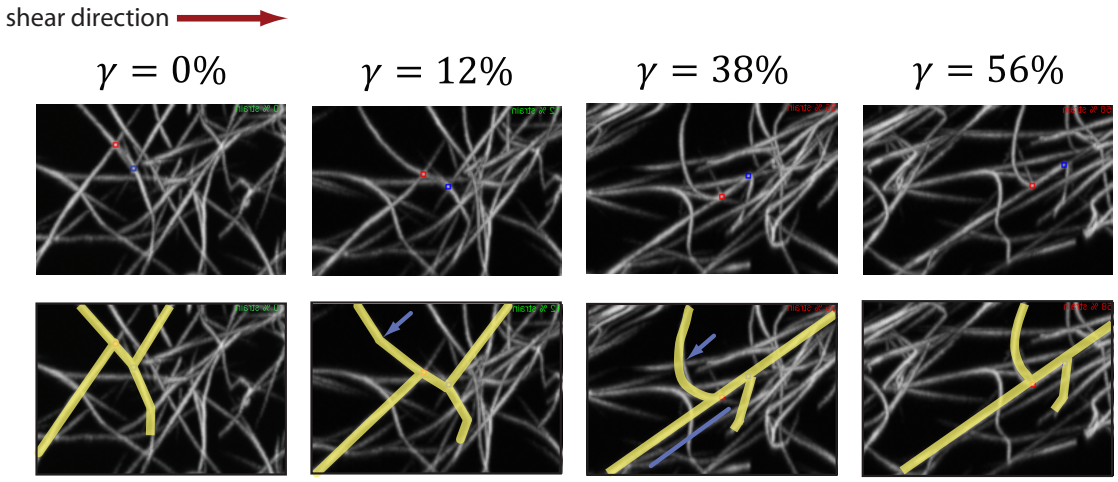

Figure 11.1: Several maximum projections taken in the Y-Z plane as the network is sheared to four strain points. Two typical node motions are illustrated. The upper set has the two nodes marked in blue and red, while the lower set has the fibers outlined in yellow. Blue arrows indicate bent and buckled areas, while the straight yellow line illustrates the straightness of the fiber through both nodes.

We take a maximum projection of several $Y - Z$ slices taken from each image stack as the strain on the network is increased (see fig. 11.1 the direction of strain, $-y$, is shown going towards the right-hand side of the page). By examining these projections, we can see a distinct behavior of two branch points that represents a

behavior that is often seen as the network is strained. These two nodes are connected via fibers which form a sort of zig-zag shape through them (see fig. 11.1). As the network is strained to small strains, the upper node starts to move downwards in the z direction. This is a highly non-affine motion (had the motion been affine, we would have seen the nodes simply translate over in the $-y$ direction). As the node moves downwards in z, the fibers perpendicular to this motion (and somewhat out of the XY plane), begin to bend and buckle. As the strain on the network is increased further, the fibers move more non-affinely until the fibers that connect the nodes form a straight line (see fig. 11.1). Once this line has formed, these nodes move relatively affinely, and the individual fibers start to become stretched. The point where the fibers form a straight line coincides well with the onset of strain-stiffening in the network.

If we examine this motion more closely and compare it to the affine expected motion, we can intuitively understand why the network undergoes this type of motion (see fig. 11.2). Basically, the nodes in the network move analogously to strings connected via nodes that exert little resistance to bending. If we tug on the ends of these strings (see fig. 11.2 black arrows), the fibers will move to avoid being stretched, and they do not begin to become stretched until a straight line is formed. If we compare this to the affine predicted case, we do not see this motion, and the angle of the fibers stays basically fixed (see fig. 11.2 red prediction).

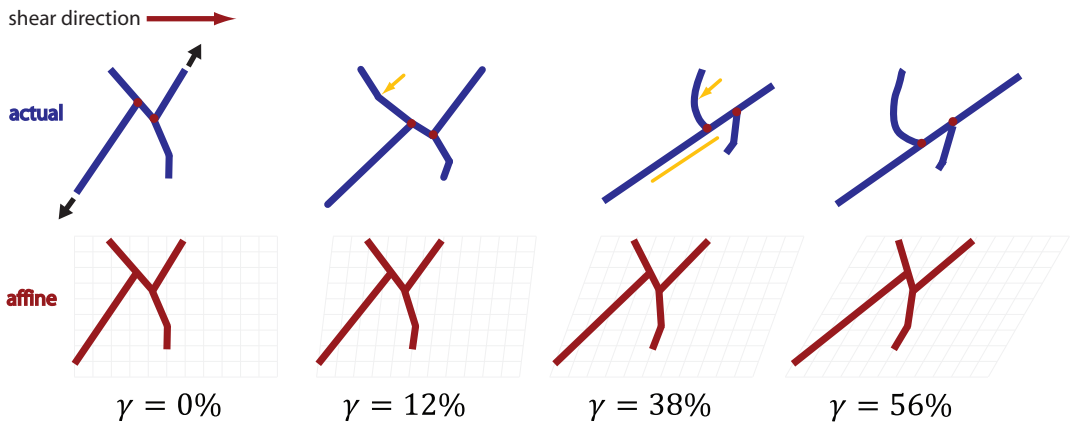

Figure 11.2: The outlined portion of the fibers taken from figure 11.1. The upper panels are the actual motion while the lower panels are the motion we would expect had the network moved affinely.

11.2 The mechanism

If we assume the network as a whole undergoes a similar type of behavior, we can build a basic understanding of the mechanism that underlies the strain-stiffening response of the network: As the network is sheared to low strains, the fibers utilize bending, rotation at branchpoints, and buckling to deform without stretching. Since the force to bend or buckle a fiber is low, the network is deformed with a small amount of force, and the stiffness is low. As the strain on the network is increased, some of the individual fibers must begin to become stretched. This requires more force, and the stiffness of the network increases. As the strain is increased even further, an increasing number of fibers starts to become stretched, and the stiffness increases non-linearly with increasing strain. This behavior is qualitatively similar to the strain-stiffening

response we measure.

This is already a fine hypothesis to explain strain-stiffening in these networks. However, we can also predict what we expect will happen at even higher strains based on this simple explanation (if the network does not break). As the strain on the network is increased sufficiently past the point where the network mechanics show non-linear stiffening, all of the fibers that will become stretched are stretched, and no additional fibers contribute to the stiffness of the network; at this point, the stiffness of the network should again become constant (the network is essentially behaving like springs in parallel). Up to this point, the hypothesis we have built depends on fibers that are behaving linearly and, indeed, the individual fibers have been measured to be linear to high stress/strain (Hudson et al., 2010). However, the fibers will exhibit a non-linear stiffening response once they are stretched to very high stress or strain (beyond strains of 1). Consequently, we conjecture that if the strain on the network can be increased far enough without the sample breaking, the individual fibers will stiffen and we will in fact, get a second non-linear stiffening response.

For the first part of this mechanism, I have many quantitative pieces of evidence that support this hypothesis (see the section below). For the second part of this mechanism, we can compare to the rheological response we measure at high stress/strain (see the section on the differential stiffness below).

This behavior of the network most likely indicates that the network has soft bending modes. We review what this means and what is already known about these kinds of systems in section 11.5.

11.3 Comparison to data from this thesis

I will review different pieces of data I have found that support my hypothesis for the mechanism that underlies the strain-stiffening response in fibrin networks:

- *The non-affinity peaks at the onset of strain-stiffening.* For every sample tested, the differential non-affinity peaked at the onset of strain-stiffening. This indicates some sort of motion on a network level. We think the individual fibers transition using a very distinct type of motion from primarily bending or rotating at branch points to becoming stretched. The peak in non-affinity may be a signature of this motion (see the chapter 7 on non-affinity). Furthermore, simulations of analogous (low-connectivity) networks also show a peak in non-affinity when the networks transition from bending or rotating to stretching (see comparison to other work below 11.5).

- *The angles between fibers change significantly at the onset of strain-stiffening.* When we examined how the angles between fibers change (the branch point angles) as the network strain-stiffened, we saw the largest change at the onset of strain-stiffening. Since we think that fibers rotate significantly about the individual branch points, this change is consistent with the underlying mechanism.

- *The fibers are not stretched in the direction of strain.* When we examined the mean individual fiber strain $< \epsilon >$, for all of the fibers in the network in chapter 9, we found that the network exhibits, on average, a negative $< \epsilon >$ at low system strains γ, before crossing 0. Moreover, we found that the earlier the γ_c was for a sample, the earlier the mean strain became positive for the

network. When we examined the distribution of mean fiber strain at different fiber orientations in the network, we found that the fibers that are expected to become stretched are actually not stretched until the network entered the non-linear regime, while the fibers that are expected to become compressed, compress (chapter 9). This corresponds well to our mechanism and indicates that fibers are, indeed, not stretched until the non-linear regime. Moreover, this explains the mean compressive strain being initially negative: since a portion of the fibers are buckled or bent (leading to an apparent negative strain[1]) and the rest of the fibers are unstretched, the average between these must be negative.

- *The shear stress of the network is well-approximated assuming the fibers behave as linearly elastic elements that require no force to bend.* The fact that we can approximate the shear stress well using an only a linear fiber response not only qualitatively supports our hypothesis, but also *quantitatively* supports our hypothesis that linear fibers can lead to a non-linear network response owing to the architecture of the network.

- *Average connectivity number near 3* The average connectivity number of each node is quite low (around 3). In the absence of bending or branch point stiffness, a network needs a connectivity number of at least 6 to form a network that will begin to stretch immediately. When a network has a lower average connectivity

[1]To understand why buckling or bending gives a 'negative'individual fiber strain, recall our definition of $\epsilon = \delta l./l$. This was defined for the end-to-end distance between branch points. When fibers bend or buckle, the fiber end points get closer together or stay roughly the same distance apart. Therefore, ϵ, measured as it is defined, will be 0 or negative. (Also, recall that fibers are long and slender. Therefore, they will not bear compressive load and will, instead, buckle)

number, the network can undergo other types of motions (such as the ones we observe) and the network mechanics may be non-linear (Wyart et al., 2008). I explain this in more detail in the section 11.5.

- *The mechanical response of platelets in the presence of fibrin.* We don't discuss the mechanical response of platelets on the fibrin mechanics in this part of the thesis. However, when we add platelets, which act as small contractile elements, their effect on the mechanics of fibrin is exactly as expected from our interpretation of the mechanical response (see the part of this thesis on platelets).

11.4 The mechanical regimes of fibrin

In this section, we will investigate how the network behaves throughout a range of stresses and strains. In particular, we will investigate how the network behaves at very high stress and strain. It is difficult to examine a stress-strain response on a linear plot and see exactly how the stress changes with respect to strain. In particular, it is difficult to see if the change is linear or non-linear; therefore, we instead examine the differential modulus, K', of the network on a logarithmic plot (K' is just the derivative of stress with respect to strain. For more details see section 2.2.1)

The network response shows four regimes[2]: I have numbered these regimes from low to high stress (see fig 11.3).

[2]At very, very small stress or strain, you sometimes see another regime; however, tou cannot see this in the figure shown. I do not know why this sometimes occurs (it is at very, very small strains (less than 1% usually) so it might have to do with the rheometer. Although, maybe it is interesting!)

1. At the lowest stresses, the network has a constant stiffness (corresponding to the linear modulus of the sample).

2. The response of the network is non-linear.

3. The network becomes less non-linear and almost shows a constant stiffness.

4. At very, very high stress the network will show a final non-linear regime.

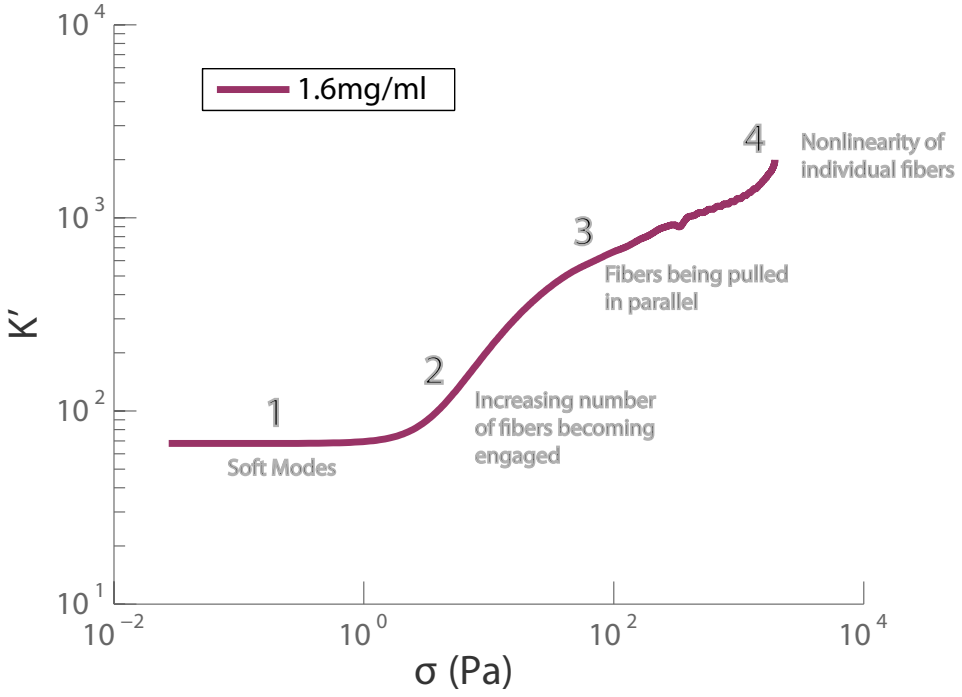

Figure 11.3: The differential modulus of fibrin. The response shows four different regimes.

The mechanical response of fibrin is consistent with our understanding of its microscopic behavior:

1. The low strain, linear regime, corresponds to the soft bending modes being 'pulled out'as the strain on the network is increased.

2. The second regime corresponds to an increasing number of fibers becoming stretched and contributing to the stiffness of the network.

3. The third regime corresponds to the point where no more fibers contribute to the bulk strain, and the fibers that are being stretched remain stretched, leading to another almost constant stiffness regime. In this regime, the fibers are just being pulled in parallel with a slight change in angle from the geometry of the shear deformation (leading to the non-constant shear modulus).

4. The final regime occurs when the individual fibers do eventually become non-linear (in many samples, the network does not reach this point before breaking).

As further evidence, we compare the K' response of several different concentrations. The low strain modulus in regime 1 shows a roughly c^2 scaling. This is consistent with a linear regime in which the response is bending dominated (Piechocka et al., 2010). Moreover, in regime 3, the fibers are behaving like springs in parallel and the high strain modulus scales with the number of fibers being pulled. Therefore, we expect it to collapse with concentration. These scalings are consistent with scalings found in previous rheological studies on fibrin networks (Piechocka et al., 2010).

These mechanical regimes of fibrin have been reported before (Piechocka et al., 2010). However, their underlying origins were attributed to the thermal motion and resulting non-linear response of individual fibers.

11.5 Discussion and relation to other studies

There are three predominant models to explain the strain-stiffening response of fibrin networks. These all assume a non-linear mechanical response of the individual fibers arising from backbone stretching (Hudson et al., 2010), an attenuation of thermal fluctuations (Piechocka et al., 2010), or water expulsion (Brown et al., 2009) when the bulk network is strained. Our results, however, suggest that a non-linear fiber response is not necessary to explain the non-linear response of the bulk network. This is consistent with atomic force microscopy measurements of the stress-strain response of individual fibrin fibers that show the fibers have a linear response to strains of 1 or higher (Hudson et al., 2010; Liu et al., 2010). The average individual fiber strains we measure are significantly below 1 at the onset of strain-stiffening.

In addition, to the three prominent models that rely on a non-linear response of individual fibers, another important idea is based on a simulation which shows that stiff biopolymer networks can transition from a bending-dominated to stretching-dominated regime (Onck et al., 2005; Kang et al., 2009). This is more consistent with our findings. This study was based on a simulation without an analytic model. Below, I will discuss more analytic approaches to understanding these types of networks. Then, I will reconcile our results to previous simulations of network behavior.

Since a linear fiber model is sufficient to explain the non-linearity of the network, the non-linearity we find must be a result of the network geometry or how the fibers are connected. Although never directly applied to fibrin, some recent general theoretical developments have shown that such a response is possible. These ideas hinge on very old ideas originally posited by Maxwell. He found that for a structure composed of

freely hinged springs to be rigid (*i.e.* exhibit a finite shear modulus), each degree of freedom for a node must be, on average, constrained by its neighbors. This is satisfied in large systems when the average node connectivity of a network, z, exceeds the critical value, z_c, of 6 in three dimensions (Wyart et al., 2008; Tang and Thorpe, 1988). When this condition is not satisfied and $z < z_c$, the network will be 'floppy'and have a 0 shear modulus at low strains. A significant amount of work has been done to gain an understanding of how networks transition from having no shear modulus to having a finite shear modulus in the 0-strain limit. These studies usually fall under the heading of 'rigidity percolation'(Tang and Thorpe, 1988). More recently, Wyart *et al.* built on this work and investigated the mechanical response of low-connectivity networks when the strain on the network is increased to finite strains. This study demonstrated that when a floppy network is strained, it will eventually yield a nonzero stress response that increases non-linearly with increasing strain. This is reminiscent of the strain-stiffening response we see in stiff biopolymer networks, such as fibrin. In their model, they predict that the characteristic strain in these networks should scale linearly with $\delta z = z_c - z$ (the higher the average connectivity number of the network, the earlier the stiffening response should occur) (Wyart et al., 2008). Fibrin networks have a z slightly larger than 3 (see chapter 6). This is much less than the critical connectivity of 6 in three dimensions. This would suggest that our networks are, in fact, floppy and the possible origin of our strain-stiffening is from its low connectivity number. However, although we find a large spread in the onset of strain-stiffening for the four different concentrations we probe, we do not measure a corresponding change in the average node connectivity.

A recent theoretical study, however, has shown that incorporating fiber bending stiffness to a system with $z < z_c$ adds constraints to the system and effectively lowers the critical constraint number (Broedersz et al., 2011). This may explain the discrepancy between our results and the predictions of Wyart, *et al.*: if the difference in γ_c between the different data-sets is not due to a change in the average connectivity number, it may instead arise from a difference in the bending stiffness of their constituent fibers. To explore this possibility, we consider the bending stiffness, κ, of individual fibers in different concentration networks. In the simplest case, the bending stiffness of a fiber with circular cross-section is given by $\kappa = E\frac{\pi}{4r^4}$ where E is the Young's modulus and r is the radius of the fiber. If the radius of our fibers remains approximately fixed for the different network concentrations, the bending stiffness should also remains fixed. However, the bending stiffness may *effectively* change as the fibrin concentration is increased. The reason this may be the case is that with increasing fiber concentration, the average fiber length shortens, making it effectively more difficult to bend each fiber. (You can also imagine scaling everything in the network by a characteristic length (such as the mean fiber length). In this case, the radius would also become effectively larger as the characteristic length became smaller with higher fibrin concentration). Consequently, the higher concentration samples may, indeed, be more constrained, leading to their strain-stiffening response occurring at lower γ. Unfortunately, the study by Broedersz *et al.* did not extend their study to finite strains. Therefore, there is no quantitative prediction exactly how γ_c should change with κ, and a direct comparison to my measurements is not possible.

The type of behavior we find in fibrin is also reminiscent of simulations of some biopolymer networks. The simulation that is the most prominent, at least in the more general area of biopolymer mechanics, is the one performed by Onck *et al.* In this simulation, they observe a low strain response that is bending-dominated and a high strain response in which individual fibers must begin to become stretched. Moreover, they see a peak in non-affinity at low strains consistent with our measurements. They attribute the change in onset of strain-stiffening to the degree of 'curviness'of the individual fibers. Basically, as individual fibers become more curved, they have a built-in 'slack length'that delays the onset of strain-stiffening (Onck et al., 2005).

Another interesting simulation investigated low connectivity networks with varied bending stiffnesses (Broedersz and MacKintosh, 2011). Qualitatively, the simulated mechanical responses are *very* similar to mechanical responses we measure. Specifically, the simulated networks exhibit three stiffness regimes similar to the first three stiffness regimes of fibrin (recall, we think the fourth regime is from the non-linearity of the fibers). In addition, with increased bending stiffness, the low-stress, linear modulus increases in the simulated networks, but the higher stress response remains unchanged. This is consistent with the behavior of the differential stiffness of fibrin when scaled by fibrin concentration.

11.6 String theory

In this section, I comment on the interesting limit where fiber compression requires no force and re-emphasize the role of geometry in understanding the strain-stiffening response of these networks.

In many of the theoretical models of networks with a low-connectivity number, they posit that the network will deform via bending if this is energetically favorable in comparison to stretching. However, even in the total absence of bending stiffness, the network *must* begin to stretch eventually. This is clear from the work of Wyart *et al.* which simulated networks of springs with no bending stiffness or branch point rigidity and found a non-linear network response (Wyart et al., 2008).

In fact, a clever way of examining this limit is geometrical. As a warning - I never figured out a way to solve this problem except in a brute-force manner, and you would not expect this simple explanation to hold for large systems. However, it is an interesting approach to the question so I will examine it here. Basically, this represents the point at which the network must begin to stretch even in the absence of bending stiffness. We treat the fibers basically as extensible strings. Therefore, they can buckle and bend with essentially no force. If we examine an area in the network, we have nodes on the top and bottom plates, nodes in the middle of the network, and connections between the nodes. As the top plate of the network is sheared, all of the nodes on the top plate move with the motion of the plate, and the bottom nodes remain fixed. This deformation will require no force as long as none of the fibers within the network are stretched. This can be accomplished by placing all of the nodes so that none of the distances between two nodes is greater than the length of the fiber that connects them (note, in this case, it can be closer than the length and still cost no energy). Once there are no arrangements left that can satisfy this condition, the network must begin to stretch the individual fibers and show a stiffer mechanical response. This is a purely geometrical way of examining the problem.

11.6.1 Strings are an interesting limit

The limit we just used, where fiber bending, buckling, and rotation cost no energy, is an interesting one.[3] It is distinct even from networks simulated by Wyart *et al.* (In this study, they used networks of springs, so compression of the elements requires the same amount of force as extension of the elements). There have been no theoretical studies on low-connectivity networks that incorporate fiber buckling (as far as I know), but it is likely to be an interesting limit. It might seem that this should just reduce the effective connectivity number by two, but I think it will be a bit more complicated than this. A quick argument why:

Consider an individual node in a random network connected to two other nodes. Let us start by examining the symmetric force case where the amount of force required to strain the fiber is the same as the force required to compress a fiber. In this case, the central node will have the lowest energy state if it neither stretches nor compresses its connecting fibers. This will constrain it to sit on a circle (or sphere in 3-space) with a radius of the length of the fiber. If a node is connected to two fibers, each fiber defines a circle, and the node will sit on the intersection points of these circles (see fig. 11.4). If, instead, we consider the asymmetric force case where the force required to compress a fiber is effectively 0, then the node can occupy any area (or volume in $3D$) with low energy as long as it is *within* the length of each fiber that connects the node

[3] In fact, in its simplest form, the fibers behave almost like the opposite of solutions of hard spheres. In these systems, it is impossible to push two spheres closer together than the sum of their two radii while you can pull them as far apart as you want with little or no energy cost. In the case of a network of strings, it is more costly to pull two nodes further away from each than the length of the fiber that connects them, but it requires no energy to push them together. A big difference between the two systems is that, in the case of connected strings, the connectivity of the network cannot change.

to its neighbors. The node is therefore significantly less constrained in comparison to the symmetric force case. Now, if the two neighboring nodes start to move away from the central node, as would happen in a shear experiment, it is clear that the overlap area will start to shrink. At high enough strain, it will vanish completely, and the fibers will have to become stretched; therefore, although the neighboring nodes may not seem to matter at low strain, these constraints will 're-appear'at higher strains.[4]

11.7 Why does the network move non-affinely?

There is currently no 'theory of non-affine motion'and understanding under-constrained networks at finite strains is still being actively investigated. Of course, the reason a network behaves non-affinely is because this represents a lower energy state. This is a somewhat vague notion; however, we develop a bit of intuition about the exact network behavior by considering what happens to a few representative fibers as a small network is sheared.

We create an over-simplified network composed of a few fibers (see figs. 11.5 and 11.6). When the network is deformed affinely, the nodes and fiber positions are all determined by the affine transformation (they simply translate over the amount prescribed by the transformation). We move the nodes and fibers in fig. 11.5 to mimic this type of motion. With an affine type of deformation, some of the fibers have become longer/stretched, and some of them have become shorter/compressed.

[4]You can almost think of the overlap volume that we have just defined as some sort of free volume or an area the node can explore with little energetic cost

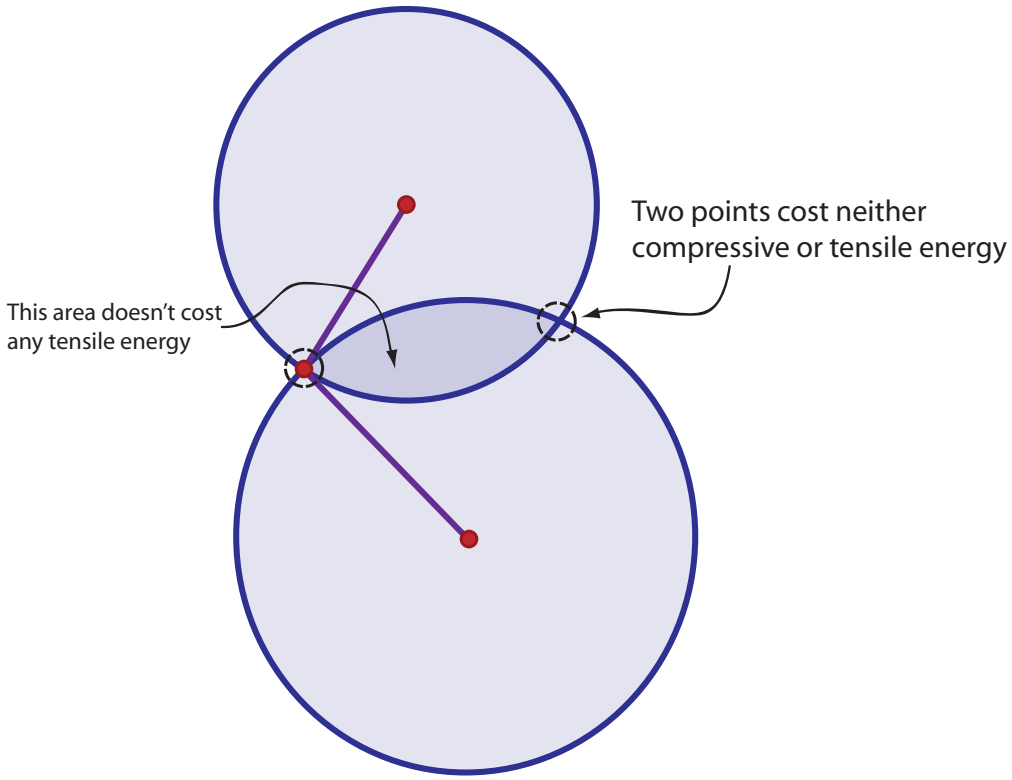

Figure 11.4: Graphic of all of the positions a node connected to two other nodes can occupy in $2D$ when compressing a fiber requires the same force as stretching a fiber or, alternatively, requires no force at all.

This costs a lot of strain energy. Moreover, we examine some of the central nodes and note that force balance clearly does not hold at these points (unless we added some torque from the branch point stiffness or something similar to compensate) (see fig 11.5).

Now, we repeat the deformation but let the nodes move non-affinely. Again, the upper plate moves, and the nodes connected to the upper plate move with it. However,

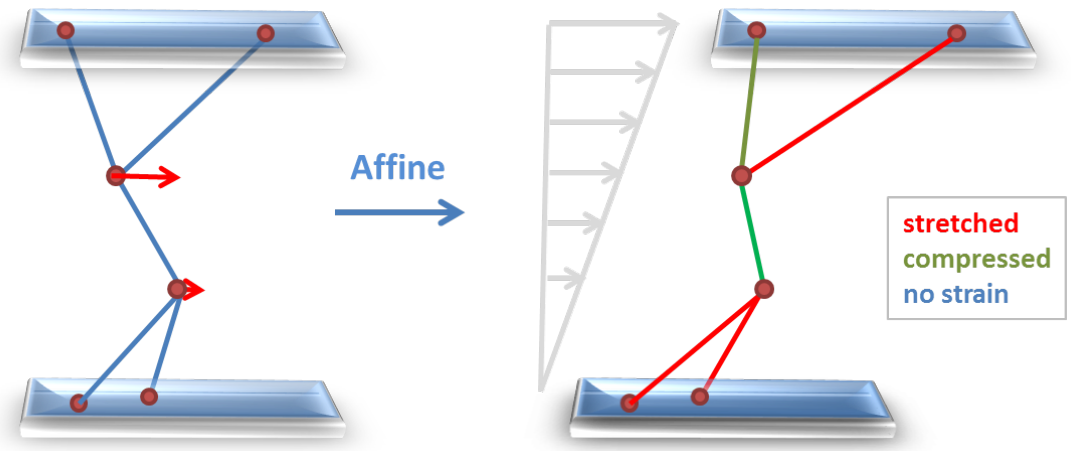

Figure 11.5: When a network moves affinely, every point translates in the direction of strain a fixed amount. The sheared network (right-hand side) will have strains over the fibers that depend solely on their original orientation in the network.

now that the individual fibers can move non-affinely, they find a network configuration that lowers the total number of stretched or compressed fibers. In the example in fig. 11.6, we see that an arrangement in which none of the fibers are compressed or stretched is possible. This gives us some intuition about why the nodes might move non-affinely and exhibit the types of behaviors we observe in the network.

11.8 Conclusion and future directions

We find that fibrin networks have soft-bending modes. As the network is deformed, it utilizes these soft-bending modes to deform without stretching the individual fibers. At high enough strain, these modes will be exhausted and the individual fibers will begin to become stretched. This type of microscopic behavior as well as the resulting mechanics are consistent with the behavior and mechanics of networks with low-

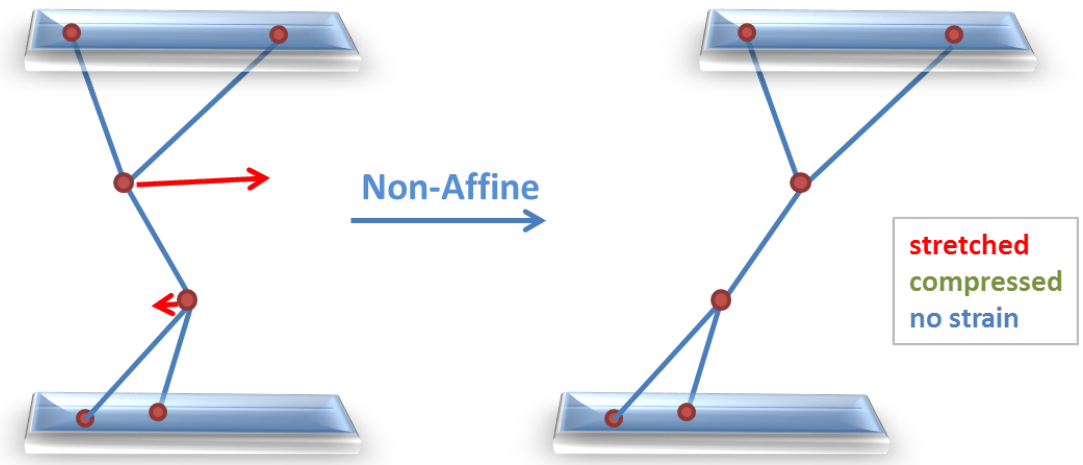

Figure 11.6: When a network moves non-affinely, the nodes in the network can move transversely or less/more than the affine expected motion. This enables the network to relieve the strain on the individual fibers. In the graphic above, the fibers have all moved to accommodate the strain without stretching or compressing any of their components.

connectivity number and small bending stiffness.

The current theoretical work done in understanding low-connectivity networks with bending stiffness have primarily focused on the behavior of these networks in the 0-strain limit. It will be interesting to quantitatively compare further work on the finite-strain limit to real networks such as the fibrin networks we have explored in this thesis.

In previous studies, whether the network deforms via stretching or bending depends in large part on the relative energies required to deform in these manners. Moreover, although never considered in simulations or models of low-connectivity networks, networks composed of fibers which can buckle with little or no force may

be an interesting limit. In particular, this limit may be interesting for fibrin systems where we observe significant fiber-buckling as well as a regime where most fibers are highly compressed at low system strains. [5]. Beyond accounting for the relative energies of bending, stretching, rotation etc., there is also a geometric upper limit where fibers must begin to become stretched. Future theoretical work will undoubtedly uncover the relative importance of each these different aspects.

Moreover, fibrin is similar to other stiff biopolymer networks such as highly bundled actin or collagen networks. These networks also have nodes with low connectivity number. Therefore, their mechanics may also be well understood from the context of networks with soft bending modes. However, this remains to be investigated.

[5]The stiffness from rotation at individual branch points is also likely to be important. However, we have not seen any obvious signatures of this in our measurements of fibrin behavior.

Part IV

Platelets!

Chapter 12

Effect of platelets on fibrin mechanics

We measure the mechanics of fibrin networks at different concentrations with increasing platelet concentration. The procedure to measure the mechanics is relatively straightforward: we initiate the polymerization of a fibrin gel with thrombin, which also activates the platelets. This causes the platelets to start to adhere to and contract the fibrin gel once it begins to form. The mixture is quickly pipetted in between two rheometer plates. This mixture is incubated for at least one hour to allow the fibrin network to form and the platelets to finish contracting. Afterwards, we impose a steadily increasing strain on the sample and measure the resulting stress.

12.1 Stress-strain response in the presence of platelets

Consistent with our previous measurements, in the absence of platelets, the stress-strain response of the network shows strain-stiffening (see fig. 12.1 blue line). As we increase the platelet concentration, the curve shifts to earlier strains (fig. 12.1 red and green curves) (Shah and Janmey, 1997).

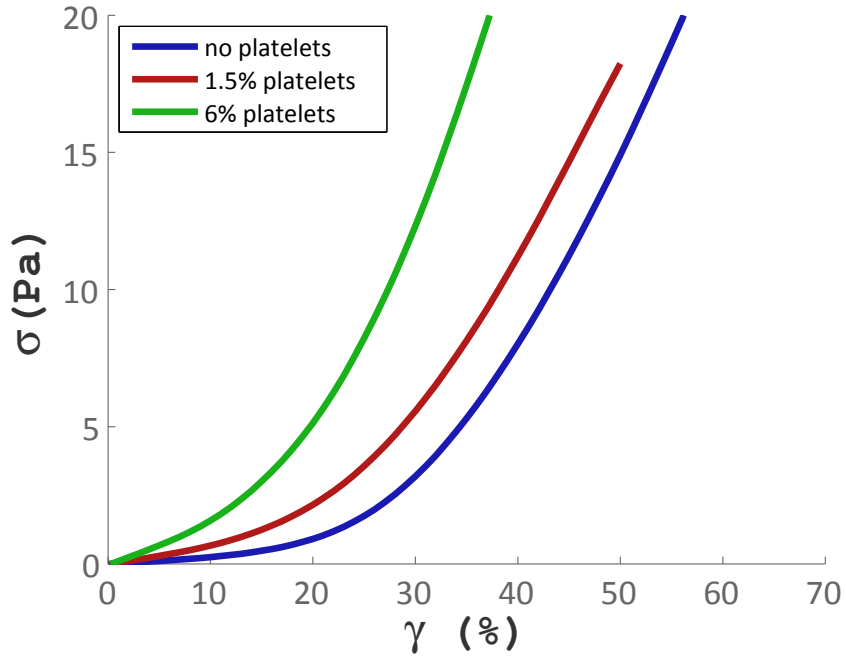

Figure 12.1: Stress-strain response of a 0.2mg/ml network with increasing platelet concentration

12.2 Differential stiffness

It is easier to interpret these data by examining the differential stiffness of these networks, K'. This is simply the derivative of the stress-strain curve at every point,

$K' = \frac{d\sigma}{d\gamma}$. It is a measure of the stiffness of the sample. At low strains, this value corresponds to the linear modulus of the sample. We can either plot this value versus stress, σ (see fig. 12.2), or versus strain, γ (see fig. 12.3). The former is useful in understanding the stiffness of a sample when a given force is applied. The latter is useful for understanding the stiffness of a sample at a certain degree of deformation.

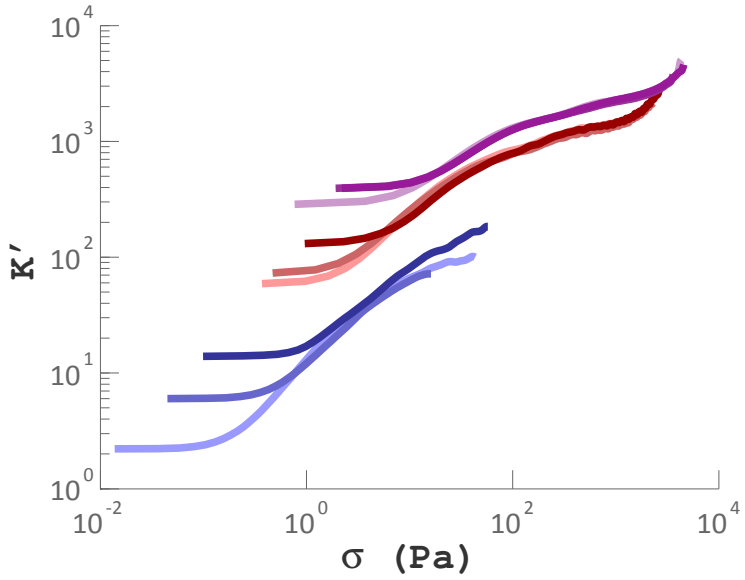

Figure 12.2: The differential stiffness for many samples versus stress. Each color is a different fibrin concentration. The darker the color the higher the amount of platelets in the sample.

If we examine how the platelets change the mechanical response of the network versus stress, we find that, with increasing platelet concentration, the linear modulus of the network increases but eventually intersects the curve without any platelets. We can understand this change by considering what is going on in the fibrin network in the absence of platelets. At small stresses, the stiffness of the gel is determined by the force required to bend or rotate the individual fibers. Adding platelets to the gel

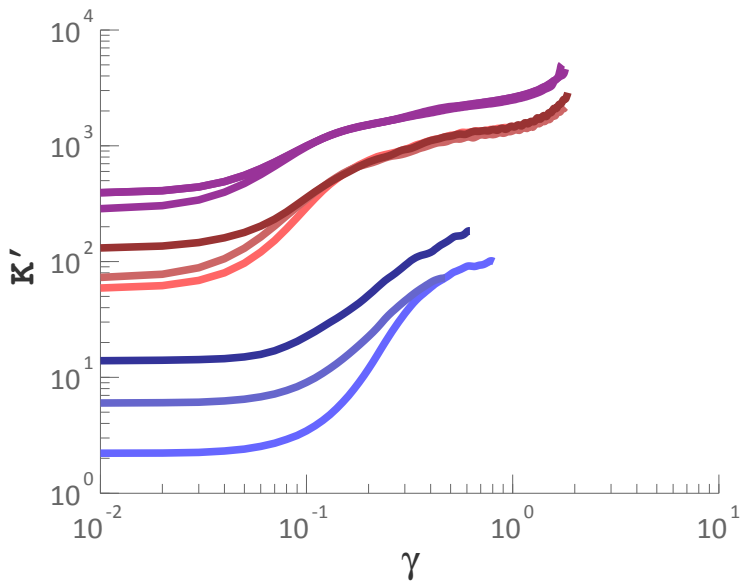

Figure 12.3: The differential stiffness for many samples versus strain. Each color is a different fibrin concentration. The darker the color the higher the amount of platelets in the sample.

causes the platelets to 'pull-out'some of the soft bending modes causing the network to be more constrained. This leads to a stiffening of the network in this regime. However, once it reaches the high-stress regime, where all of the fibers that will be engaged are being stretched, the network again just behaves like springs being pulled in parallel. This shows that the high-strain response of the gel remains unchanged. It also indicates that the platelets act solely as contractile elements. In particular, they do not behave as stiff inclusions in a soft background matrix as previously proposed (Lam et al., 2010).

We can characterize exactly how the linear modulus, G_0, critical stress, σ_c and critical strain, γ_c scale with fibrin concentration for different platelet concentrations. We find that with higher fibrin concentration, the effect of the platelets is less for

both σ_c and G_0 (fig. 12.4).

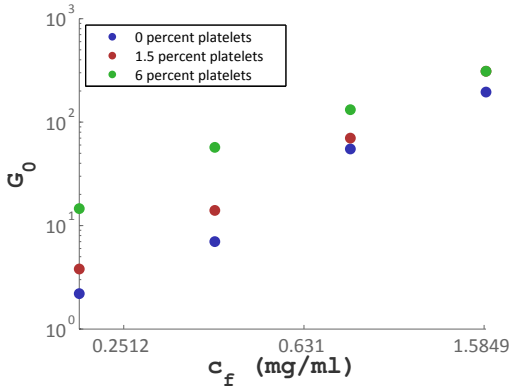

(a) G

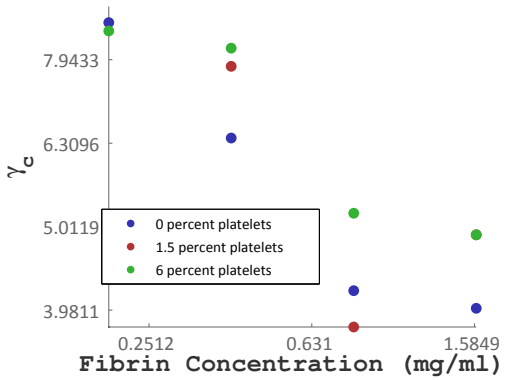

(b) 2% platelets

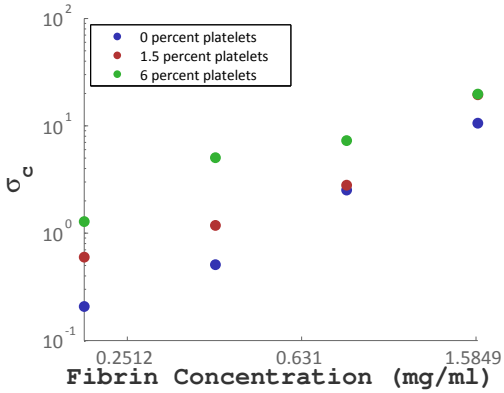

(c) 5% platelets

Figure 12.4: Network structure for 0.2mg/ml fibrin with increasing platelet concentration

12.3 Relation to previous results

A simulation of low-connectivity networks measured the differential stiffness of the networks with increasing 'motor concentration'. The 'motors'acted like small contractile elements similar to the platelets in the fibrin gels. The linear modulus in these networks increased with increasing motor force; this is consistent with the

results we measure here. Moreover, these simulations indicated that an affinely deforming network sets un upper limit to the K' (Broedersz and MacKintosh, 2011). The platelet/fibrin composite network response showed less of a mechanical change with increased fibrin concentration. We expect from the smaller non-affinity and earlier strain-stiffening, that high concentration fibrin networks are more constrained. Therefore, these data may indicate that the closer a network is to the upper affine limit, the more difficult it is for platelets to stiffen the gel further.

Chapter 13

Effect of platelets on clot structure

We can examine how the structure of fibrin networks is altered with the addition of platelets. We add platelets of three concentrations to fibrin networks of four different concentrations. We take confocal image stacks of randomly selected areas in each network. We examine maximum projections corresponding to equal volumes for each of the networks. The platelets appear as white spots in these images. Examining the images, we find that platelets cause a significant amount of aster-like formation around them in the network (see all figures in this chapter, 13.1, 13.2, 13.3, 13.4, 13.5). This is more significant for the low-concentration networks and becomes less significant for higher concentration fibrin networks.

This is consistent with our measurements of the mechanical effects of platelets. The lower fibrin concentrations show a more pronounced change in linear modulus when platelets are added. A similar alteration in the structure is consistent with our understanding that the primary effect of platelets on gel mechanics is through contraction of the network structure.

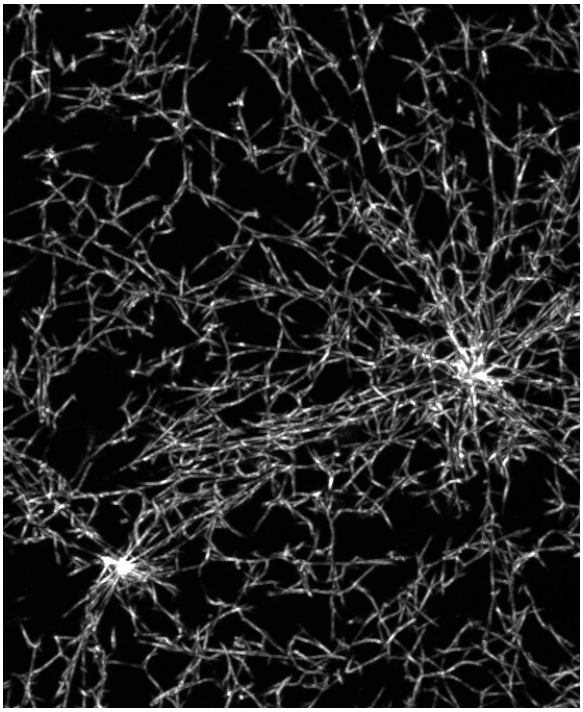

Figure 13.1: Zoomed in region of platelet contracted area

13.1 Relation to previous work

That platelets cause aster-like formation in fibrin gels is well-known (Carr, 2003). That this change has a dependence on fibrin concentration has not been reported (to my knowledge).

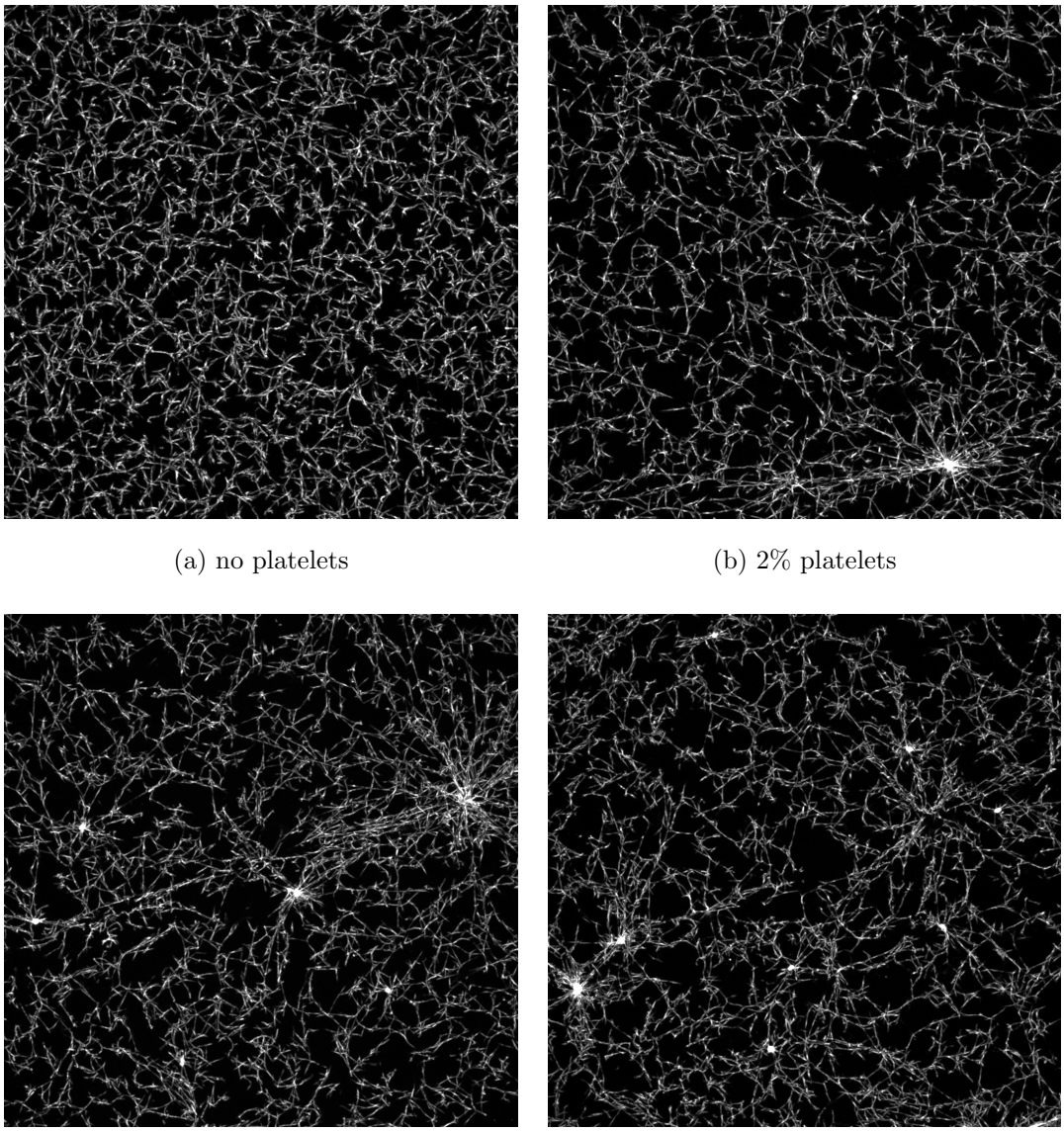

(a) no platelets

(b) 2% platelets

(c) 5% platelets

(d) 10% platelets

Figure 13.2: Network structure for 0.2mg/ml fibrin with increasing platelet concentration

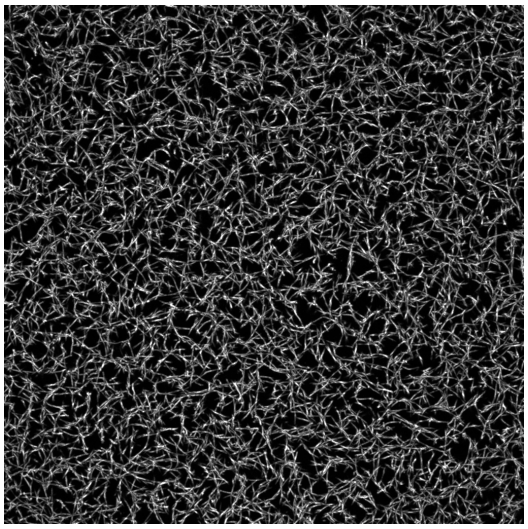

(a) no platelets

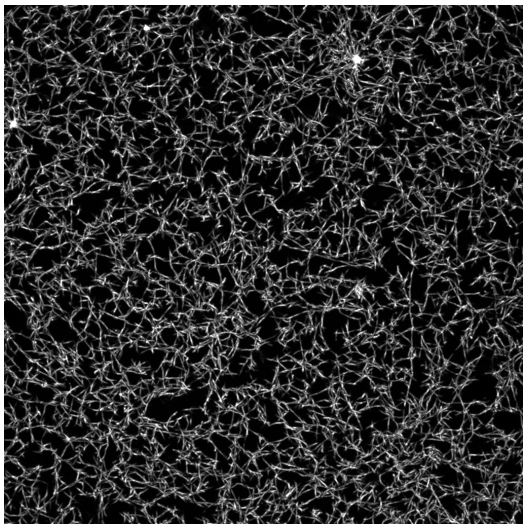

(b) 2% platelets

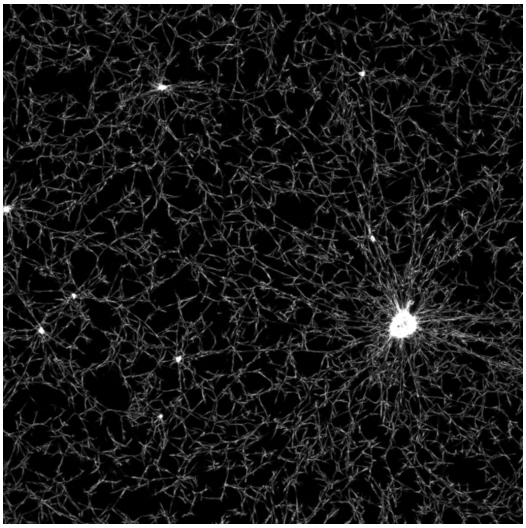

(c) 10% platelets

Figure 13.3: Network structure for 0.4mg/ml fibrin with increasing platelet concentration

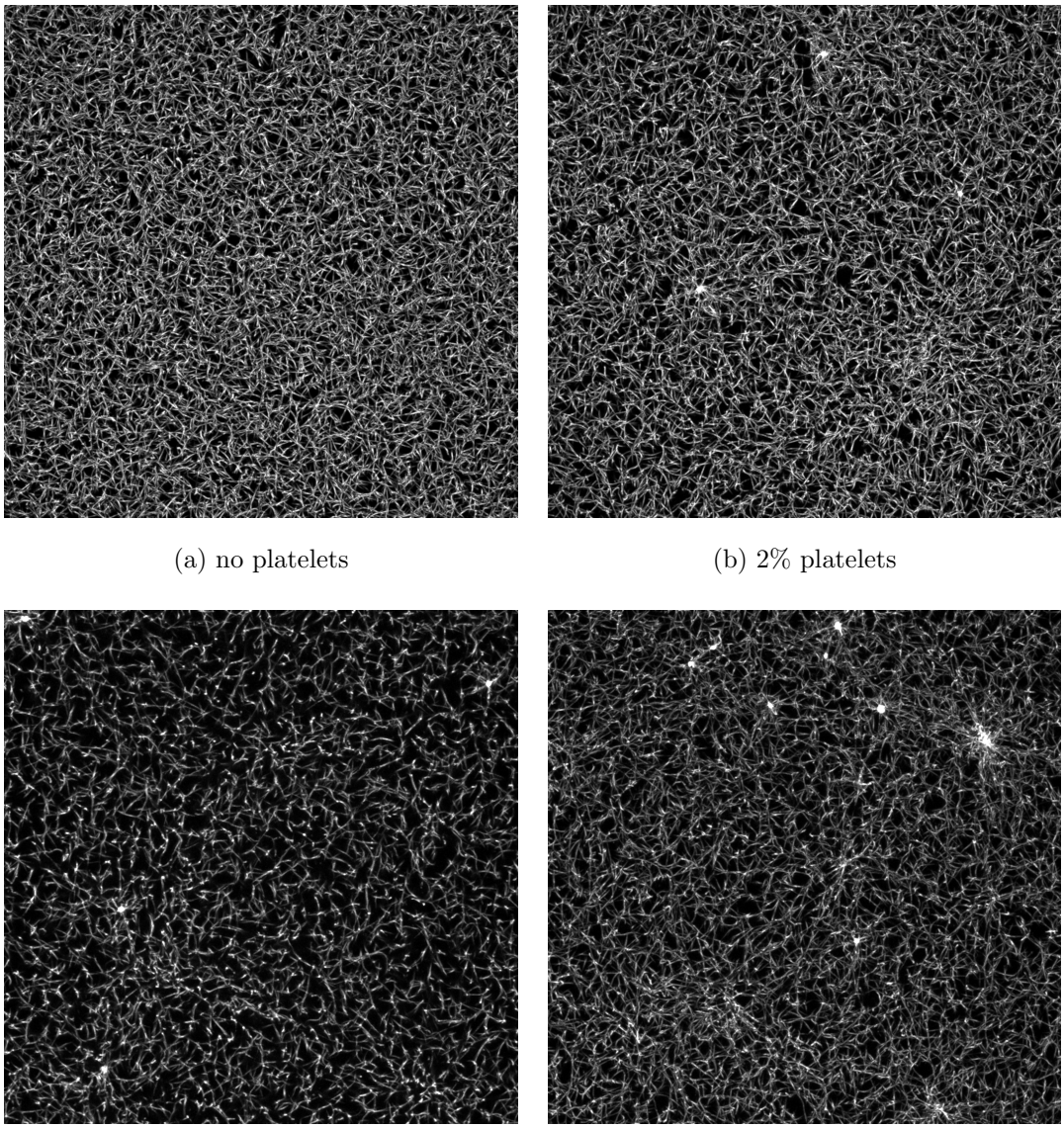

(a) no platelets

(b) 2% platelets

(c) 5% platelets

(d) 10% platelets

Figure 13.4: Network structure for 0.8mg/ml fibrin with increasing platelet concentration

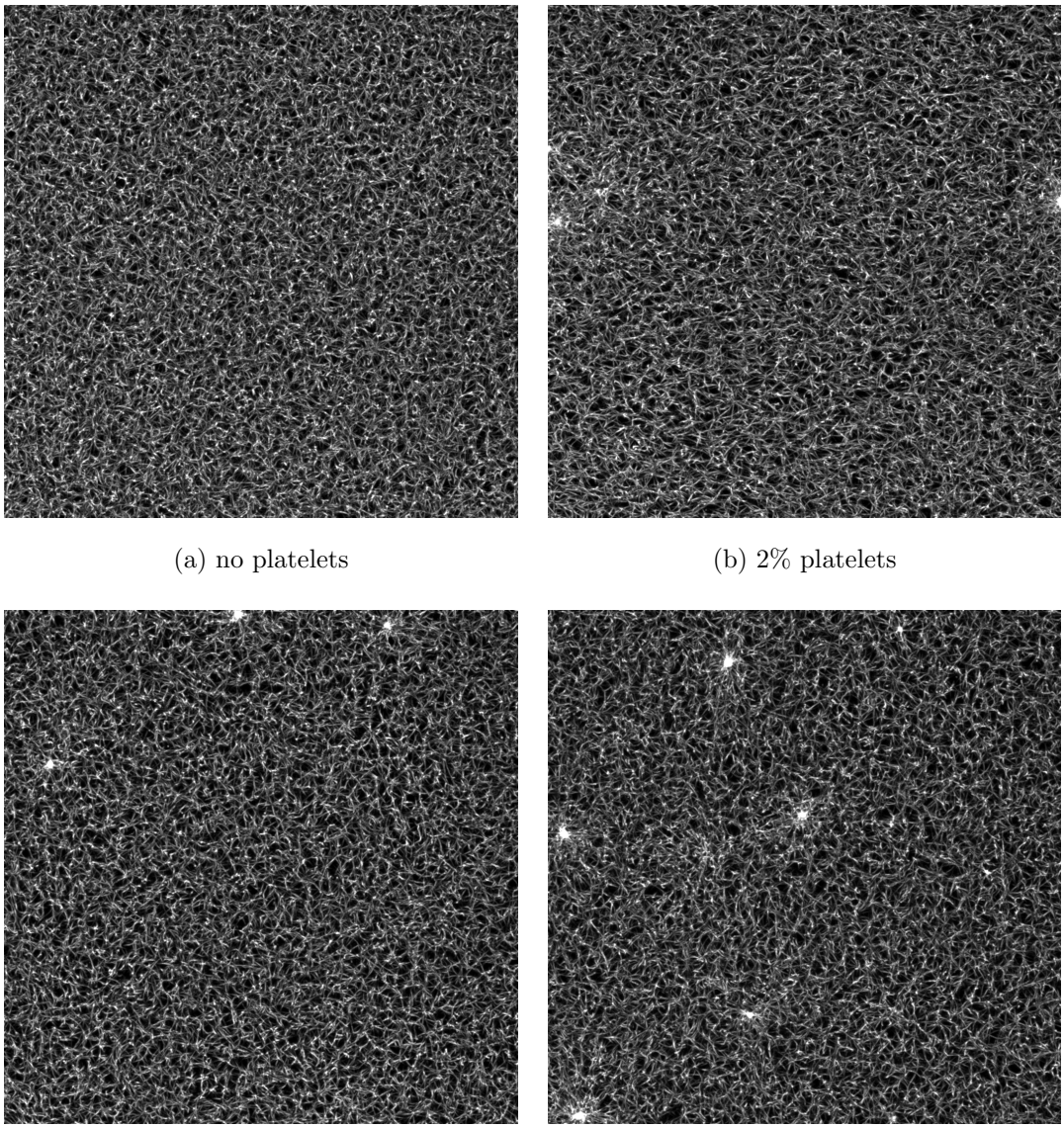

(a) no platelets

(b) 2% platelets

(c) 5% platelets

(d) 10% platelets

Figure 13.5: Network structure for 1.6 mg/ml fibrin with increasing platelet concentration

Part V

Materials and Methods

Chapter 14

Fibrin

14.1 Basic fibrin polymerization protocol

1. Human alpha-thrombin and fibrinogen (H-T 1002a and FIB3 respectively, Enzyme Research Labs, South Bend, Indiana) is stored at $-80°C$.

2. Thrombin is kept on ice and diluted to twice its final concentration in fibrin buffer. Thrombin is used quickly after dilution.

3. Fibrinogen is kept between $25°C$ and $30°C$ on a heat block. It is also diluted to twice its final concentration in fibrin buffer.

4. For fluorescently labeled samples, a portion of the diluted fibrinogen is fluorescently labeled. It is added for a final ratio of $6 : 1$ for unlabelled to labeled fibrinogen.

5. The $2X$ thrombin solution is added quickly to the $2X$ fibrinogen solution in equal proportions. The solution is pipetted a few times rapidly and added to the rheometer or shear cell in the appropriate amount.

6. For shear cell samples: the shear cell is 'pre-blocked'with a fibrinogen solution at $\sim 0.2mg/ml$ in fibrin buffer and allowed to incubate for at least 2 minutes. It is then removed with a Kimwipe before adding the final sample. (On shear cell samples with a force layer, this step is omitted.)

7. The samples are incubated for at least 6 hours to allow complete polymerization and cross-linking.

14.2 Fluorescently labelling fibrinogen

This protocol is adapted from the standard invitrogen protocol that comes with the invitrogen TAMRA-SE ($c-1171$ Invitrogen) dye.

1. First day: Dialyze fibrinogen at stock concentration(15mg/ml) from $-80°$C into reaction buffer. Typically $1ml$ fibrinogen solution is added to a Slide-A-Lyzer cassette

    - RXN Buffer: $0.25M$ Sodium Bicarbonate, pH8.5

2. *second day:*

    - 2mg TAMRA-SE (invitrogen c-1171) is dissolved into $100\mu l$ DMSO. Aliquot this into $10\mu l$ volumes and store all but one in the $-80°$C for future use
    - Dilute the $10\mu l$ aliquot with $90\mu l$ RXN buffer.

- Vortex to mix.
- Remove the fibrinogen from the Slide-A-Lyzer and put in eppendorf tube. Add $100\mu l$ of the dye mixture to the 1mL of fibrinogen
- Let react for 1 hour while rotating at room temperature while the sample vial is wrapped in aluminum foil
- Add this solution back into a Slide-A-Lyzer Cassette and dialyze against fibrin buffer (see above protocol) for > 24 hours.

14.3 Basic rheological protocol

1. Add thrombin to the fibrinogen solution and load quickly into the rheometer (typically I use the $AR-G2$ from TA instruments fitted with a $40mm$, $4\circ$ cone plate geometry).

2. As the network polymerizes, you monitor the polymerization by performing a time sweep with a 0.5% strain amplitude and a frequency of 1 rad/s. The G' and G" is recorded during this process. Usually polymerization takes several hours (typically for the low thrombin concentrations I use, the sample takes ~ 6 hours to polymerize).

3. Measure the stress-strain relation by imposing a steadily increasing strain on the network and recording the corresponding stress. I try to match the rate I use in the rheometer to the average rate I use during the shear experiment. This depends on the size of the field of view I use in the microscope and the step size I use. Typically, this results in rates around $5 \cdot 10^{-5}$ or so (a long time).

14.4 Construction of a shear cell without a force layer

(a) ROS

(b) ROS with the upper glass plate of the shear cell

Figure 14.1: A ring of stability with and without the piece of glass that will be the top plate

1. Create a ROS (ring of stability) (see fig. 14.1a)
   (a) Take a flat washer
   (b) Take a large coverslip $22mmx22mm$ no. 1
   (c) Using Norland Optical 81 adhere the coverslip to the washer.
2. Cut a regular microscope slide down to a $\sim 0.5\ cm^2$
3. Place the ROS on the microscope.
4. Place the cut piece of slide on top of the ROS (see fig. 14.1b)
5. Epoxy the top plate to the end of a rod coming out of the $3D$ stage that will eventually do the shearing (see fig. 14.2)

6. Wait until epoxy is cured.

7. Raise the top plate up $\sim 0.8mm$. (Use the $10x$ objective to find the distance of the top plate from the bottom)

8. Then pre-block the sample for 2 minutes. Thoroughly wipe and dry the cell.

9. Then load sample

10. Seal the sample using a mineral oil

11. Wait for polymerization

12. Have shear fun!

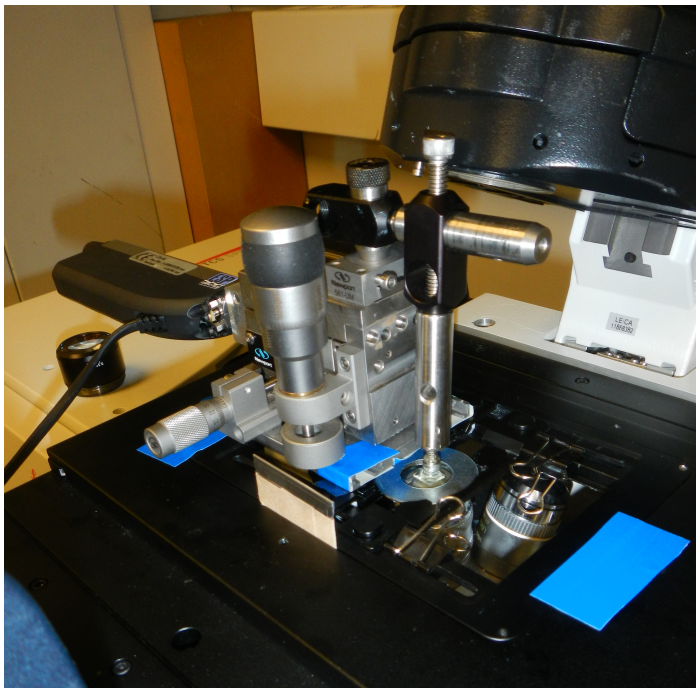

Figure 14.2: A depiction of the finished shear cell sitting on the confocal microscope

14.5 Basic shearing protocol on the microscope

1. The shear cell is constructed out a stage that can control motions in X, Y, and Z. We have replaced the micrometer screw (or whatever it is called) in the Y direction with a motor we can control with standard $RS232$ protocols.

2. Using a simple matlab code I wrote to control the motor, I set up a simple script that moves the stage a fixed amount (in roughly 1% strain steps) at timed intervals.

3. Then, I setup the confocal microscope to take an image stack at similarly timed intervals.

4. To perform the shear experiment, you start the imaging on the confocal and the script on the computer that controls the shear cell concurrently.

14.6 Force layer on a coverslip

(In collaboration with Stefan Muenster (SM) and Tom Kodger (TEK))

1. NuSil preparation a. Mix : i. Half NuSil A (with 1/5th NuSil A with beads from TEK) ii. Half NuSil B by weight

2. Spin coat at 1000 RPMs onto a coverslip for a final thickness of 30um (done by TEK)

3. Bake at 90°C for at least 1 day

4. (Simultaneously: measure the NuSil rheology on the rheometer)

14.7 Construction of shear cell with force layer

(In collaboration with SM and TK)

1. Create a ROS (ring of stability)
   (a) Take a flat washer
   (b) Take a large coverslip with a 30um NuSil layer
   (c) Using Norland Optical 81 adhere the coverslip (force layer side away from the washer) to the washer.
   (d) Scrap NuSil off the sides of the coverslip using a razor blade. (leaving a square in the center where your sample will go)
   (e) Clean up any NuSil residue using hexane
   (f) Cut two spacers with a height $200\mu m$. This serves as a spacer to place the top plate on while epoxying it. Place these strips on either side of the square of NuSil
2. Cut a regular microscope slide down to a $0.5cm^2$
3. Place the ROS on the microscope (force layer side up).
4. Place cut piece of slide on top of the spacers on the ROS
5. Epoxy the top plate to the end of a rod coming out of the 3D stage that will eventually do the shearing (see pic)
6. Wait till epoxy is cured.

7. Use the 10x objective to find the distance of the top plate from the bottom
8. Raise the top plate up ~ 0.8mm
9. Then load sample
10. Seal the sample using a vacuum grease in a syringe that is heated up. (The grease should be liquid when it cools it seals in the sample without running all over the place)
11. Wait for polymerization

14.8 Buffers

Fibrin Buffer 150mM NaCl, 20mM HEPES, 20mM $CaCl_2$ pH7.4

Chapter 15

Platelets

15.1 Polymerization of fibrin with platelets protocol

1. Human alpha-thrombin and fibrinogen (H-T 1002a and FIB3 respectively, Enzyme Research Labs, South Bend, Indiana) is stored at $-80°C$.

2. Thrombin is kept on ice and diluted to twice its final concentration in fibrin buffer. Thrombin is used quickly after dilution.

3. Fibrinogen is kept between $25°C$ and $30°C$ on a heat block. It is also diluted to twice its final concentration in fibrin buffer.

4. Immediately before initiating the polymerization of the fibrin and activation of platelets, the following are mixed with equal volumes resulting in a solution of fibrinogen and platelets in platelet buffer which have twice the final concentration for the sample.

(a) Fibrinogen is diluted to 4 times its final concentration in platelet buffer. For microscopy samples, a small amount of fluorescently labeled fibrinogen (at a ratio of 1:6) is added to this solution (see the fibrin materials and methods for more details on fluorscently labelling fibrinogen).

(b) Platelets are diluted to 4 times their final concentration.

5. To initiate the polymerization reaction, equal portions of the thrombin solution from step 2 and the platelet-fibrinogen solution from step 4 are mixed together and quickly pipetted either between two plates on the rheometer or into a flow cell on the confocal microscope.

   (a) Final concentration of thrombin: 0.25 U/ml

   (b) Final concentration of platelets is systematically varied between 1% and 10%.

   (c) Final concentration of fibrinogen is systematically varied between 0.2 and 1.6 mg/ml.

15.2 Platelet purification

Platelets were purified from human blood obtained from volunteers and subsequently gel-filtered as described in (Shah and Janmey, 1997) with the exception that all experiments were performed within 12 hours of purification and the platelets were stored at 25°C. Platelet concentrations in this thesis are all relative to their concentration after purification and reported as their diluted volume. For instance, 1%

platelets indicates that the platelets have been diluted to $1/100th$ of their their concentration after purification in platelet buffer.

15.3 Basic rheological protocol for platelet-fibrin samples

1. Add thrombin to the fibrinogen-platelet solution and load quickly into the rheometer

2. As the network polymerizes and the platelets contract the gel, you monitor the polymerization by performing a time sweep with a 0.5% strain amplitude and a frequency of 1 rad/s. The G' and G" is recorded during this process. The samples are let polymerize for 2 hours.

3. A constant strain rate of $0.01/s$ is applied while measuring the resultant stress to determine the full response (both the low- and high-strain response) of the networks.

Note: the activity of the platelets change over time. Therefore, to compare the effect of platelets under different conditions, samples are run on four rheometers concurrently. Each rheometer is fitted with a different tool:

- Anton Paar: fitted with a 50 mm, 1° cone plate
- Two AR-G2s: each fitted with a 40 mm, 4° cone plate
- Ares G2: fitted with a 40 mm, $0.04rad$ cone plate

15.4 Platelet-fibrin samples for confocal microscopy

1. 1. A flow cell with several lanes is constructed on a number 1.5 or number 1 coverslip:
   (a) Several strips of mounting tape are placed parallel to each other on the coverslip to create lanes.
   (b) A glass microscope slide is cut to fit over these lanes, and then pressed in place over these lanes.
   (c) Each lane represents a different platelet and fibrinogen concentration sample.
   (d) All the conditions are loaded in succession. (As quickly as possible, to avoid any differences in platelet activity over time).
2. The samples are allowed to incubate for several hours.
3. An image stack of each lane is taken at random locations $50\mu m$s off the surface.

15.5 Buffers

Fibrin Buffer 150mM NaCl, 20mM HEPES, 20mM $CaCl_2$, pH7.4

Platelet Buffer 140mM NaCl, 10mM HEPES, 3mM KCl, 0.5mM $MgCl_2$, 5mM $NahCO_3$, 10mM Glucose, pH7.4

Bibliography

Broedersz, C. P. and MacKintosh, F. C. (2011). Molecular motors stiffen non-affine semiflexible polymer networks. *Soft Matter*, 7(7):3186, doi:10.1039/c0sm01004a.

Broedersz, C. P., Mao, X., Lubensky, T. C., and MacKintosh, F. C. (2011). Criticality and isostaticity in fibre networks. *Nat Phys*, 7(12):983–988, doi:10.1038/nphys2127.

Brown, A. E. X., Litvinov, R. I., Discher, D. E., Purohit, P. K., and Weisel, J. W. (2009). Multiscale mechanics of fibrin polymer: Gel stretching with protein unfolding and loss of water. *Science*, 325(5941):741–744, doi:10.1126/science.1172484.

Carr, M. E. (2003). Development of platelet contractile force as a research and clinical measure of platelet function. *Cell biochemistry and biophysics*, 38(1):55–78.

Chao, F. C., Shepro, D., and Yao, F. (1970). Clot retraction: II. theoretical model of platelet filamentogenesis. *Microvascular Research*, 2(1):61 – 66, doi:10.1016/0026-2862(70)90051-8.

Cohen, I. (1979). The contractile system of blood platelets and its function. *Methods and achievements in experimental pathology*, 9:40–86. PMID: 368520.

Collet, J.-P., Shuman, H., Ledger, R. E., Lee, S., and Weisel, J. W. (2005). The elasticity of an individual fibrin fiber in a clot. *Proceedings of the National Academy of Sciences of the United States of America*, 102(26):9133–9137, doi:10.1073/pnas.0504120102.

Doi, M. and Edwards, S. (1988). *The Theory of Polymer Dynamics*. The International Series of Monographs on Physics Series. Clarendon Press.

Gonzalez, R. C., Woods, R. E., and Eddins, S. L. (2004). *Digital Image processing using MATLAB*. Pearson Prentice Hall, Upper Saddle River, N.J.

Hantgan, R., Taylor, R., and Lewis, J. (1985). Platelets interact with fibrin only after activation. *Blood*, 65(6):1299–1311.

Hudson, N. E., Houser, J. R., III, E. T. O., II, R. M. T., Superfine, R., Lord, S., and Falvo, M. R. (2010). Stiffening of individual fibrin fibers equitably distributes strain and strengthens networks. *Biophysical Journal*, 98(8):1632 – 1640, doi:10.1016/j.bpj.2009.12.4312.

Huisman, E. M., Heussinger, C., Storm, C., and Barkema, G. T. (2010). Semiflexible filamentous composites. *Phys. Rev. Lett.*, 105:118101, doi:10.1103/PhysRevLett.105.118101.

Kang, H., Wen, Q., Janmey, P. A., Tang, J. X., Conti, E., and MacKintosh, F. C. (2009). Nonlinear elasticity of stiff filament networks: Strain stiffening, negative normal stress, and filament alignment in fibrin gels. *The Journal of Physical Chemistry B*, 113(12):3799–3805, doi:10.1021/jp807749f.

Kim, E., Kim, O. V., Machlus, K. R., Liu, X., Kupaev, T., Lioi, J., Wolberg, A. S., Chen, D. Z., Rosen, E. D., Xu, Z., and Alber, M. (2011). Correlation between fibrin network structure and mechanical properties: an experimental and computational analysis. *Soft Matter*, 7(10):4983, doi:10.1039/c0sm01528h.

Lam, W. A., Chaudhuri, O., Crow, A., Webster, K. D., Li, T.-D., Kita, A., Huang, J., and Fletcher, D. A. (2010). Mechanics and contraction dynamics of single platelets and implications for clot stiffening. *Nature Materials*, 10(1):61–66, doi:10.1038/nmat2903.

Lewis, J. (1995). Fast normalized cross-correlation. In *Vision interface*, volume 10, pages 120–123.

Liu, W., Carlisle, C. R., Sparks, E. A., and Guthold, M. (2010). The mechanical properties of single fibrin fibers. *Journal of Thrombosis and Haemostasis*, 8(5):1030–1036, doi:10.1111/j.1538-7836.2010.03745.x.

MacKintosh, F. C., Käs, J., and Janmey, P. A. (1995). Elasticity of semiflexible biopolymer networks. *Phys. Rev. Lett.*, 75:4425–4428, doi:10.1103/PhysRevLett.75.4425.

Onck, P. R., Koeman, T., van Dillen, T., and van der Giessen, E. (2005). Alternative explanation of stiffening in cross-linked semiflexible networks. *Phys. Rev. Lett.*, 95:178102, doi:10.1103/PhysRevLett.95.178102.

Piechocka, I. K., Bacabac, R. G., Potters, M., MacKintosh, F. C., and Koenderink, G. H. (2010). Structural hierarchy governs fibrin gel mechanics. *Biophysical Journal*, 98(10):2281–2289, doi:10.1016/j.bpj.2010.01.040.

Ryan, E. A., Mockros, L. F., Weisel, J. W., and Lorand, L. (1999). Structural origins of fibrin clot rheology. *Biophysical Journal*, 77(5):2813–2826.

Schwarz Henriques, S., Sandmann, R., Strate, A., and Koster, S. (2012). Force field evolution during human blood platelet activation. *Journal of Cell Science*, 125(16):3914–3920, doi:10.1242/jcs.108126.

Shah, J. V. and Janmey, P. A. (1997). Strain hardening of fibrin gels and plasma clots. *Rheologica acta*, 36(3):262–268.

Storm, C., Pastore, J. J., MacKintosh, F. C., Lubensky, T. C., and Janmey, P. A. (2005). Nonlinear elasticity in biological gels. *Nature*, 435(7039):191–194, doi:10.1038/nature03521.

Tang, W. and Thorpe, M. F. (1988). Percolation of elastic networks under tension. *Phys. Rev. B*, 37:5539–5551, doi:10.1103/PhysRevB.37.5539.

Timoshenko, S. and Gere, J. M. (2009). *Theory of elastic stability*. Dover Publications, Mineola, N.Y, 2nd ed., dover ed edition.

Weisel, J. W. (2004). The mechanical properties of fibrin for basic scientists and clinicians. *Biophysical Chemistry*, 112(2-3):267–276, doi:10.1016/j.bpc.2004.07.029.

Weisel, J. W. (2008). BIOPHYSICS: enigmas of blood clot elasticity. *Science*, 320(5875):456–457, doi:10.1126/science.1154210.

Wen, Q., Basu, A., Winer, J. P., Yodh, A., and A Janmey, P. (2007). Local and global deformations in a strain-stiffening fibrin gel. *New Journal of Physics*, 9(11):428–428, doi:10.1088/1367-2630/9/11/428.

White, J. G. (2007). Chapter 3 - platelet structure. In MD, A. D. M., editor, *Platelets (Second Edition)*, pages 45 – 73. Academic Press, Burlington, second edition edition.

Wyart, M., Liang, H., Kabla, A., and Mahadevan, L. (2008). Elasticity of floppy and stiff random networks. *Physical Review Letters*, 101(21), doi:10.1103/PhysRevLett.101.215501.